Atomic-scale study of structural and optical properties of nanoscale systems

Eric Weikum

Normandie Université

UNIVERSITÉ DE ROUEN NORMANDIE

THÈSE

Pour obtenir le diplôme de doctorat

Spécialité **PHYSIQUE**

Préparée au sein de l'**Université de Rouen Normandie**

Atomic-scale study of structural and optical properties of nanoscale systems

Présentée et soutenue par

ERIC WEIKUM

Thèse soutenue le 24/11/2023

devant le jury composé de :

M. AURELIEN CRUT	Maître de Conférences - UNIVERSITE LYON 1 CLAUDE BERNARD	Rapporteur du jury
M. LUIZ TIZEI	Chercheur HDR - UNIVERSITE PARIS-SACLAY	Rapporteur du jury
M. DIDIER BLAVETTE	Professeur des Universités - Université de Rouen Normandie	Membre du jury
MME EVA MONROY	Directeur de Recherche - UNIVERSITE GRENOBLE ALPES	Président du jury
M. LORENZO RIGUTTI	Maître de Conférences - Université de Rouen Normandie	Directeur de thèse
MME ANGELA VELLA	Professeur des Universités - Université de Rouen Normandie	Co-directeur de thèse

Thèse dirigée par **LORENZO RIGUTTI** (GROUPE DE PHYSIQUE DES MATERIAUX) et **ANGELA VELLA** (GROUPE DE PHYSIQUE DES MATERIAUX)

ED 591 PSIME

GPM Groupe de Physique des Matériaux

Acknowledgments

The contributions presented in this manuscript would not be possible without the relentless dedication of my thesis directors Lorenzo Rigutti and Angela Vella. I am indebted to Lorenzo Rigutti for being the guiding hand of this thesis. His advice and the direction which he offered me will always be kept treasured by me. I'm also incredibly thankful for having Angela Vella as the co-director of my thesis. Her abillity to understand (usually quicker than me) my developing thoughts has been very helpful during my work at the GPM.

Asides from allowing me to profit from their great expertise on the research subjects discussed in this thesis I'm especially appreciative for the insights on the academic environment and on the professional approach regarding organized projects which they have shared with me. I am very grateful for their encouragement, guidance and especially patience which has allowed me to develop our ideas into this project. I will never forget the fruitful discussions we had.

I'd also like to thank the entirety of the ERIS team. Especially I'd like to thank Ivan Blum, Pradip Dalapati and Abraham Neftali Diaz for their experimental support and Jonathan Houard and Gerald da Costa for making the PAP experiments possible on the technical level by realizing and maintaining the PAP set-up and its software interface. The ease with which this team is able to modify the instrumental set ups and the data acquisition and treatment is truly remarkable. The combined expertise on Atom Probe Tomography of this team has made my time here a great professional pleasure. I wish the entire team great success for their future endeavors.

[13] Wohl dem Menschen, der Weisheit erlangt,
und dem Menschen, der Einsicht gewinnt!
[14] Denn es ist besser, sie zu erwerben, als Silber,
und ihr Ertrag ist besser als Gold.

Sprüche 3 LUT

[13] Happy is the man that findeth wisdom,
And the man that getteth understanding.
[14] For the merchandise of it is better than the merchandise of silver,
And the gain thereof than fine gold.

Proverbs 3 KJV

[13] Heureux l'homme qui a trouvé la sagesse,
Et l'homme qui possède l'intelligence!
[14] Car le gain qu'elle procure est préférable à celui de l'argent,
Et le profit qu'on en tire vaut mieux que l'or.

Proverbes 3 LSG

Contents

List of Figures

List of Tables

General Introduction

The technological proliferation of nanostructured devices has left an undeniable impact on the modern world. With the omnipresence of computers and light-emitting devices in daily life the role of applied semiconductor physics and nano-optics has become apparent. For the quality control and the development of these devices delicate characterization techniques like Transmission Electron Microscopy, Atom Force Microscopy and Secondary Ion Emission Spectroscopy are required.

The Laser-assisted Atom Probe (La-APT) allows for the chemical characterisation of nanostructured semiconductor specimen with near atomic resolution. While this technique allows for a unique way to obtain three dimensional chemical information, it does not have the instrumental abillity to extract optical information from the specimen. This represents an obvious drawback when compared with competing characterization technologies like Transmission Electron Microscopy, which can utilize the well established Cathodoluminescence technique to obtain information on the optical transition of the studied system.

This thesis focuses on the nanometric investigation of light emitting heterostructures, based on non-Silicon material systems using the Photonic Atom Probe (PAP) technique, which couples the microscopic information obtained from La-APT Tomography with Photoluminescence (PL) spectroscopy. This coupling allows to extract the specimen's Photoluminescence response by utilizing the laser pulse which is inherent to the La-APT to excite photocarriers. While the PAP has already been shown to give access to the correlated APT reconstruction data and PL response of a variety of different specimen systems, this technology itself is still not fully characterized. The present work serves to further our understanding of the PL signal detected within the PAP set up and to present its ability for the characterization of semiconductor device structures.

This thesis is divided in four chapters. Chapter 1 establishes the fundamental basis of the concepts discussed in this thesis. It introduces the physical basis of the heterostructures which are to be investigated in this manuscript and presents the usual techniques

of their current investigation. A special focus is laid on the APT technique here. In order to better understand its capabilities and limitation its physical background and its historical development are outlined. Finally the state of the art of the correlation between APT and Photoluminescence experiments is presented including some examples of the studies already performed using the PAP.

Chapter 2 presents the material systems which are studied in this thesis, namely a system consisting of ZnO quantum wells (QWs) embedded in (Mg,Zn)O barrier material and an (In,Ga)N Laser Diode which is grown on a GaN-based heterostructure which also contains a Tunnel Junction. Also the PAP is presented on an instrumental level here. The main focus of this chapter is however the description of the Finite-Difference-Time-Domain (FDTD) method and how FDTD calculations can be used to understand the development of the PL signal detected by the PAP set-up.

In Chapter 3 the ZnO/(Mg,Zn)O QW system is investigated. By comparing the experimentally observed PL behavior of the specimen to the FDTD calculation results information on both the specimen and the PAP instrument are gained. By performing a polarization resolved investigation of a specimen in the PAP instrument and comparing the experimental results to FDTD calculations the orientation of the dipole emitters whose emit the detected PL is determined. An In-operando experiment is performed on a specimen during the performance of a PAP experiment. Comparing this experiment's results to FDTD calculation shows that the optical properties of an APT specimen are modified by the high electric field conditions which the specimen is under. These conditions are also present during the performance of an APT experiment outside of the PAP.

Chapter 4 presents a PAP investigation of an entire (In,Ga)N LD diode device embedded within a complex (Al,In,Ga)N heterostructure which contains a variety of different doping elements (Ge, Mg, Si) and a tunnel junction. This specimen represents a complex heterostructure consisting of a variety of differently composed layers. In this analysis a PAP experiment which was able to resolve the entire heterostructure was performed. With a total depth of analysis of 1.9 μm a grand total of 107 million atoms were detected during the corresponding APT analysis. From the APT data obtained from the experiment the chemical composition of the different layers is investigated granting access to the doping levels of Ge and Mg and the Ga-site fraction of Al and In. From these compositional analyses the layer structure of the specimen is obtained via APT reconstruction. By correlating the obtained APT information with the PL spectra which were recorded during the entire performance of the experiment, regions of origins and mechanisms leading to the different PL signals were determined.

1. State of the Art

In this chapter the basic background of the thesis is presented. The semiconductor heterostructures which are investigated in the context of this work, namely Quantum Wells (Section 1.1.1) and Tunnel Junctions (Section 1.1.2), as well as some experimental methods for their chemical, optical and microscopic characterization (Section 1.1.3) are introduced to the reader in Section 1.1.

A special focus is laid on the Atom Probe Tomography technique whose physical basis (Section 1.2.1) and historical development (Section 1.2.2) is presented in Section 1.2.

Finally the current state of the art of the experimental possibilities for a correlative combination of Atom Probe Tomography and Photoluminescence spectroscopy is presented in Section 1.3. Here the recently obtained insights gained from ex-situ methods (Section 1.3.1), as well as the Photonic Atom Probe (Section 1.3.2) which allows an in-situ combination of APT and PL are presented.

1.1 Heterostructure Systems

1.1.1 Quantum Wells

Functionally a Quantum Well (QW) represents a small-scale two-dimensional potential well for charge carriers. This is achieved by embedding a thin layer of a semiconductor material between two thick layers, which consist of a barrier material with a larger band-gap. Like this, a potential sink for the charge carriers ($V(x \in [-\frac{l}{2}, +\frac{l}{2}]) = 0$), which is surrounded by an energy barrier ($V(x \notin [-\frac{l}{2}, +\frac{l}{2}]) = V_{\mathrm{QW}}$) is generated.

Since the potential which is present in our problem is time-independent, every electronic state ψ needs to satisfy the stationary Schrödinger-Equation:

$$\hat{H}\psi(x) = E\psi = \left[-\frac{\hbar^2}{2m}\frac{\mathrm{d}^2\psi(x)}{\mathrm{d}x^2} + V(x)\right]\psi \Leftrightarrow \frac{\mathrm{d}^2\psi(x)}{\mathrm{d}x^2} + \frac{2m}{\hbar^2}\left[E - V(x)\right]\psi = 0 \quad (1.1)$$

The electron potential is lowered at the position of the QW layer. Let's consider the

bound electronic states for which the electron energy is smaller than the potential barrier's energy ($E < V_{\mathrm{QW}}$). By also considering a localized state boundary condition ($|\psi|^2 \to 0$ for $x \to \pm\infty$) it can be easily shown that the wave functions:

$$\psi_{\mathrm{o}}(x) = \begin{cases} \psi_{\mathrm{o},1}(x) = -A \cdot e^{+xk_1} & \text{for } x < -\frac{l}{2} \\ \psi_{\mathrm{o},2}(x) = B \cdot \sin(x|k_2|) & \text{for } x \in \left[-\frac{l}{2}, +\frac{l}{2}\right] \\ \psi_{\mathrm{o},3}(x) = +A \cdot e^{-xk_1} & \text{for } x > +\frac{l}{2} \end{cases} \tag{1.2}$$

and

$$\psi_{\mathrm{e}}(x) = \begin{cases} \psi_{\mathrm{e},1}(x) = +A \cdot e^{+xk_1} & \text{for } x < -\frac{l}{2} \\ \psi_{\mathrm{e},2}(x) = C \cdot \cos(x|k_2|) & \text{for } x \in \left[-\frac{l}{2}, +\frac{l}{2}\right] \\ \psi_{\mathrm{e},3}(x) = +A \cdot e^{-xk_1} & \text{for } x > +\frac{l}{2} \end{cases} \tag{1.3}$$

are the solutions of Eq. (1.1) for odd and even parity states respectively. The resulting Eigen-energies of these states can be calculated by inserting the wave functions Eq. (1.2) and Eq. (1.3) into the Schrödinger equation for $x \in [-\frac{l}{2}, +\frac{l}{2}]$ and $x \notin [-\frac{l}{2}, +\frac{l}{2}]$:

$$E = \frac{\hbar^2 |k_2|^2}{2m} = V_{\mathrm{QW}} - \frac{\hbar^2 k_1^2}{2m} \tag{1.4}$$

Since the wave functions have to be continuous and continuously derivable at every x (including $x = \pm\frac{l}{2}$), k_1 and $|k_2|$ have to fulfill the conditions:

$$\begin{aligned} k_1 &= +|k_2| \cdot \tan\left(\frac{l|k_2|}{2}\right) && \text{for even parity states} \\ k_1 &= -|k_2| \cdot \cot\left(\frac{l|k_2|}{2}\right) && \text{for odd parity states} \end{aligned} \tag{1.5}$$

By defining $q = \frac{lk_1}{2}$ and $p = \frac{l|k_2|}{2}$ Eq. (1.5) can be reduced to be dependent on only one variable:

$$p^2 + q^2 = \frac{k_1^2 l^2}{4} + \frac{|k_2|^2 l^2}{4} = \frac{2m}{\hbar^2} \frac{V_{\mathrm{QW}} \cdot l^2}{4} = R^2 \tag{1.6}$$

Since R^2 is independent of k_1 and $|k_2|$, the q-dependence can be eliminated from Eq. (1.5):

$$\begin{aligned} +p \cdot \tan(p) &= \sqrt{R^2 - p^2} && \text{for even parity states} \\ -p \cdot \cot(p) &= \sqrt{R^2 - p^2} && \text{for odd parity states} \end{aligned} \tag{1.7}$$

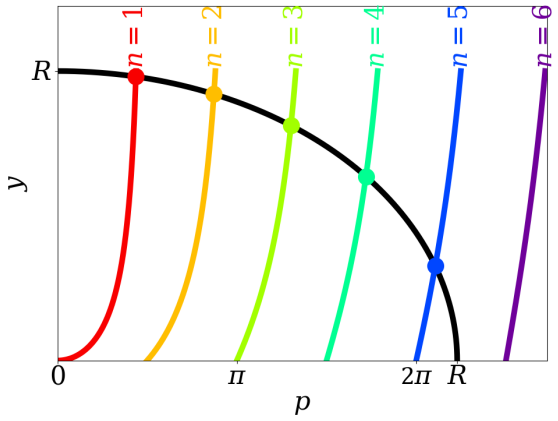

Figure 1.1: Graphical plot which allows to find the $p = \frac{l \cdot |k_2|}{2}$-values of the different states, which are bound to the QW. From these the allowed wave vectors $|k_2|$ can be calculated.

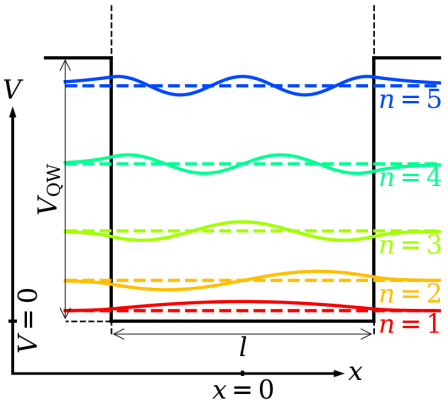

Figure 1.2: Wave functions of the all the electon states, which are bound to a QW with finite energy V_{QW}. These wave functions are characterized by their wave vectors, which are determined in Fig. 1.1

.

The solutions of the transcendental Eq. (1.7) give all allowed wave vectors $|k_2|$, which describe the bound states of the QW and can obtained graphically by plotting $+p \cdot \tan(p)$ and $-p \cdot \cot(p)$ against $\sqrt{R^2 - p^2}$ as a function of p (Fig. 1.1). The intersections of these graphs give the allowed wave values for p and thus the wave vectors k_1 and $|k_2|$ for every state. With the possible values of k_1 and $|k_2|$ known, the wave function $\psi(x)$ can be visualized for all possible wave vectors (Fig. 1.2).

Quantum well behavior is characterized by electronic states, which are well separated in energy levels, due to being in a potential well. Such a discretisation of energy states represents a qualitative difference from the energy continuum, which is present for bulk material. A possible measure of this discretisation is the average difference between the QW's energy levels. Since there is only one state for every p-intervall of a length of $\pi/2$, and there are no p-values higher than R, which result in electronic states bound to the QW the total number of states bound to the QW (N) can be estimated as:

$$N \approx \frac{2R}{\pi} = \frac{l}{\pi}\sqrt{\frac{2m}{\hbar^2} V_{\mathrm{QW}}} \tag{1.8}$$

By dividing QW's the barrier potential V_{QW} by the number of states N, a measure of

the average energy spacing between the QW states can be obtained.

$$\langle \Delta E \rangle \approx \frac{V_{\mathrm{QW}}}{N} \approx \frac{\pi \sqrt{V_{\mathrm{QW}}}}{l} \sqrt{\frac{\hbar^2}{2m}} \tag{1.9}$$

In order to achieve a high energetic spacing between the electron states bound to the QW and thus to obtain QW-behavior of the electrons inside of the potential sink, the barrier potential V_{QW} needs to be high or the length of the potential sink l has to be small. While the barrier potential is given by the material which is chosen for the barrier and QW, the length of the potential sink can be tuned by modifying the growth parameters of the specimen.

The potential landscape which is characteristic for QWs (Fig. 1.2) can be produced within semiconductor materials by the growth of heterostructures. By creating a thin low band gap layer which is sandwiched between two thick layers of high band gap material this potential landscape can be achieved. While the low band gap layer serves as a potential sink for both electrons and holes, the high band gap layers represent the potential barrier confining the charge carriers. The electronic transitions between these confined electron and hole states give rise to the QW's characteristic optical response.

Considering the barrier potential (which is of the same order of magnitude as the difference between the band-gap of the QW-material and the barrier material) to be V_{QW}=100 meV and the average spacing between the states bound to the QW to be $\langle \Delta E \rangle$ =20 meV (resulting in roughly five QW states), the length of the QW would have to be of the order of l =10 nm. In order to create such a thin structure, sophisticated growth techniques are necessary. Only after the development of modern deposition techniques like molecular beam epitaxy (MBE, Davey and Pankey (1968)) and metal-organic chemical vapor deposition (MOCVD, Manasevit (1968)) the production of solid state specimen which show the optical transition properties predicted in this section has become possible (Dingle et al. (1974)). Quantum wells have found applications in LED (Ozden et al. (2001)) as well as for general photoemitters, optical modulators and detectors (Chaisakul et al. (2019)).

1.1.2 Tunnel Junction

When applying a voltage to a body usually the current which passes through a given body rises with a rising applied voltage ($\frac{\mathrm{d}V}{\mathrm{d}I} > 0$). This situation can be described as "positive differential resistance" and is a very common phenomenon. The increase of a an electrical current due to an increase in applied voltage, which is to be expected for a

biased conductor (Ohm (1828)), is described by this notion.

It is however possible to design devices for which an increase in voltage hinders the transport of charge carriers in a specific voltage interval. One example of such a "negative differential resistance" device is the gas discharge tube (Frith and Rodgers (1896)). In a solid state device such a voltage-current characteristic can be achieved by a Tunnel Junction (also knows as Esaki (1958) Diode).

This device can be realized by producing a p-n junction where both sides have doping levels that are high enough to be able to consider them to be degenerate. This means that the Fermi energy lies within the valence band for the p-type portion and inside of the conduction band for the n-type part of the p-n junction (Fig. 1.3a). The extremely high doping levels ($\approx 10^{20}$ cm^{-3}) of both zones lead to very small depletion lengths (≈ 15 nm), meaning that the region where the Fermi energy differs significantly from the bulk material is small enough to allow quantum tunneling between the n-type and p-type region to take place. The width of the depletion zone is the length over which the charge carriers have to tunnel through. This fact leads to the unusal behavior that a reversely

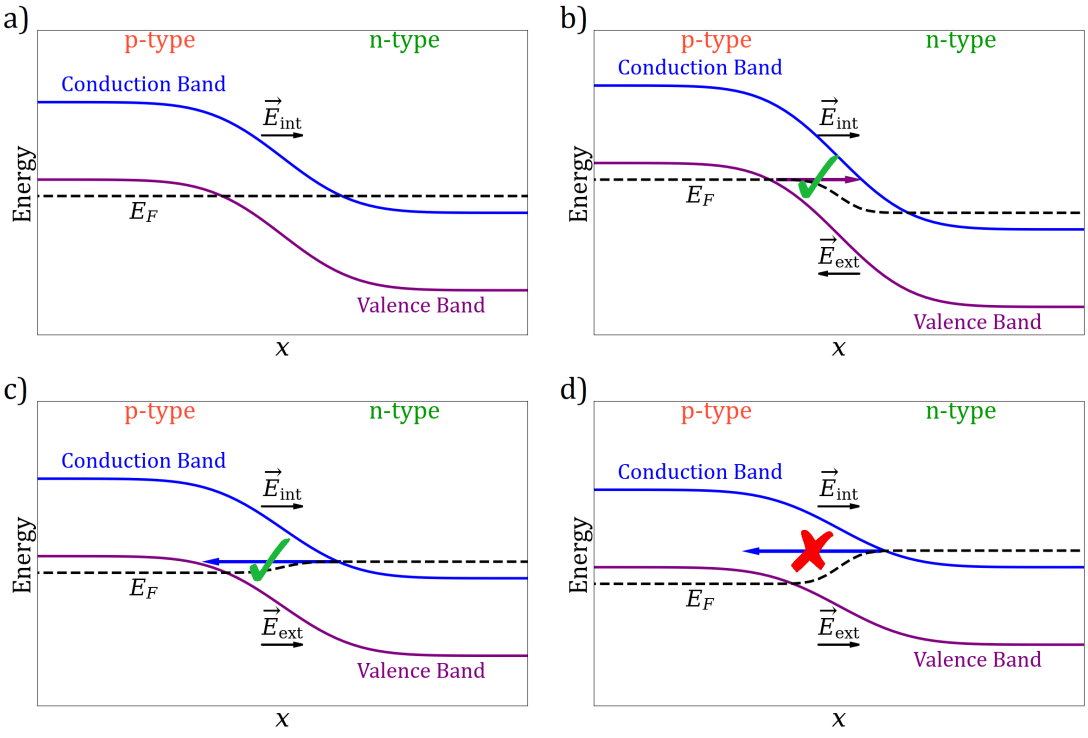

Figure 1.3: Band diagram of a Tunnel Junction under different bias conditions.
a) unbiased TD, b) reverse bias, c) small forward bias, d) high forward bias.

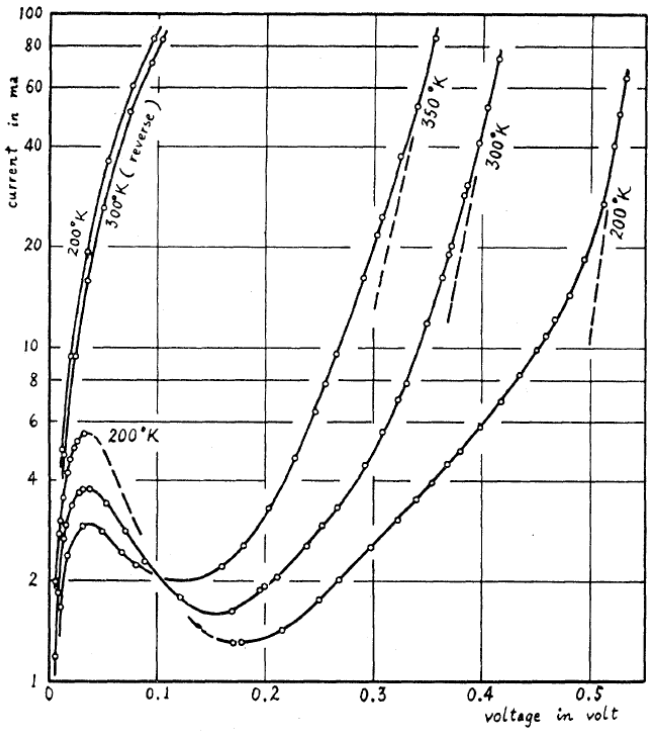

Figure 1.4: Current-voltage characteristics of the TJ studied in Esaki (1958).

biased (Fig. 1.3b) Tunnel Junction (TJ) allows for a significant flow of electrical currents (Fig. 1.4).

At a small forward bias (Fig. 1.3c), the TD allows for charge carrier transport much like a regular p-n junction. If however the applied voltage exceeds a critical value, the tunneling of charge carriers becomes hindered (Fig. 1.3d). At a sufficiently high forward bias, the conduction band lies above the valence band for every x-coordinate. Since an electron can only tunnel into a state which has the same energy as its original state and no such state exists inside of the valence band, tunneling is hindered under such conditions. This situation disables the possibility of any interband tunneling of electrons and holes likewise. Fig. 1.4 shows the voltage current characteristic of the TJ investigated in Esaki (1958). It can be seen that an increase in the applied voltage results in a reduced electrical current around $V = 0.1$ V (Fig. 1.4). This represents an instance of "negative differential resistance". At even higher applied voltages ($V > 0.2$ V) diffusive charge carrier transport becomes dominant again resulting "positive differential resistance" at high applied voltages.

A biased TJ's direct effect on the charge carriers is that it induces valence band elec-

trons from the p-type doped region into the conduction band of the n-type region and holes of the n-type material's conduction band into the p-type material's valence band. This induction of charge carriers can be used as a way to introduce free charge carriers into the optically active regions of light-emitting devices (LED) in order to increase the intensity of the emitted Luminescence. This is especially useful if either there are issues with the production of high quality p-type or the n-type layers of a specific material system. Production of high quality p-type doped GaN poses such a challenge (Akasaki (2007)). By using a TJ to introduce additional free electrons or holes into poorly conductive layers their charge transport properties can be augmented for the utilization in devices (Takeuchi et al. (2001),Krishnamoorthy et al. (2014)).

1.1.3 Semiconductors Heterostructure Characterization

Both Quantum Wells (Section 1.1.1) and Tunnel Junctions (Section 1.1.2) represent semiconductor heterostructures with nanometric dimensions. Regular photon microscopy does not allow to resolve such small sub-wavelength structures. Instead other probes have to be used in order to study the properties of nanometric structures.

High resolution transmission electron microscopy (HR-TEM) provides a method to resolve quantum wells (Smeeton et al. (2003)). This method utilizes the difference in the effective cross section between an electron beam and different atoms in order to create a chemical contrast between the different phases of the specimen (Fig. 1.5). Quantum wells usually have a large deviation from the composition (≈ 10 %) of the surrounding barrier material. The dopant concentrations of the degenerate layers of the TJ, while very high for semiconductor standards (10^{20} cm^{-3}, Turski et al. (2019)), still only correspond

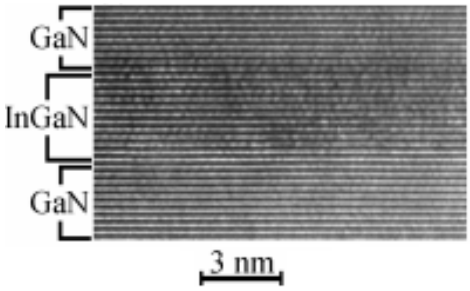

Figure 1.5: HR-TEM Image of an InGaN QW embedded in GaN (Turski et al. (2019)).

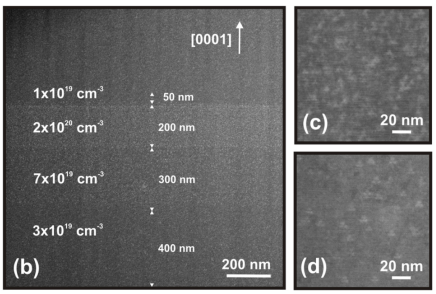

Figure 1.6: (b) HR-TEM image of Mg-doped GaN with varying doping levels. (c) $2 \cdot 10^{20}$ cm^{-3} (d) $7 \cdot 10^{19}$ cm^{-3}. The contrast in (c) and (d) comes from structural defects. (Amichi et al. (2020))

to $\approx$ 0.1 % of the atoms which constitute the TJ. This low density of dopant atoms means, that TEM-measured contrast in differently doped regions (Fig. 1.6b) is likely to be caused by the presence of defects and not by the solute dopants themselves (Amichi et al. (2020)).

Thus a difference in doping may result in a TEM contrast coming from different defect densities (Fig. 1.6c and d). The electron beam excitation of the specimen also results in the emission of Cathodoluminescence (Edwards and Martin (2011)). Due to the electron beam energy being orders of magnitude higher than the band gap of a studied semiconductor the amount of generated photocarriers is much larger than the dosage of the electron beam. This high energy excitation of the specimen also does not allow for the study of a specific electronic transition, but instead provides the optical response of every possible electronic transition of the specimen. Performing Cathodoluminescence spectroscopy during a TEM experiment provides the optical response of a point defect embedded within the specimen with a spatial resolution of around 80 nm (Tizei and Kociak (2012)). The study of localized Luminescence emitters (Quantum Disks) embedded within a nanowire specimen has shown to increase the spatial CL resolution up to 5 nm (Zagonel et al. (2011)). In cubic GaN this correlative technique can be used to study the effect of stacking fault defects on the specimen's optical response (Kemper et al. (2015)).

The usual way to perform chemical analysis in the context of a TEM experiment is energy-dispersive X-ray spectroscopy (EDX). However this method has a spatial resolution which is not sufficient to measure the thickness of very thin ($\approx$ 5 nm) QWs and has difficulties obtaining quantitative information on chemical compositions (Li et al. (2018)).

In order to measure the doping concentration of layered systems secondary ion mass spectroscopy (SIMS) is a prefered method (Takeuchi et al. (2001)). While this method provides a depth resolution on the nanometer scale (Russo et al. (2020)), its much poorer lateral resolution does not allow for the investigation of clustering phenomena, which serve as a major source for the deactivation of dopants.

Since QWs are a usual component for the optically active region of LEDs, their Luminescence properties are of particular interest. For bulk samples the optical emission properties of QWs embedded inside of LEDs are frequently studied using electroluminescence measurements (Turski et al. (2019)). This macroscopic analysis method allows for the investigation of the general light-emission behavior of LEDs under the application of an external voltage, which mimics the operating conditions of the device.

While this method allows for the study of the light-emission of a QW embedded inside of a device, a method which gives spatially resolved Luminescence information on

nanometric heterostructures allows for the optical characterization of the light-emitting structures and defects present in such nanostructures. A method which provides Photoluminescence (PL) information with a spatial resolution below the wavelength of the utilized exciting laser is Near-Field Scanning Optical Microscopy (NSOM).

A common defect which appears during the growth of (In,Ga)N/GaN QWs is the V-shaped structural defect (Hangleiter et al. (2005)). These defects have the shape of pyramids with a hexagonal basis. NSOM has shown that these defects modify the bandgap of QWs embedded inside of them (Hitzel et al. (2004)). The NSOM method also offers opportunities to correlate its results with those obtaineded from Atomic Force Microscopy (AFM), which allows the study of a specimen's surface morphology on the nanometer scale (Li et al. (2019)).

Atom Probe Tomography (Section 1.2) represents a unique method for obtaining chemical information with a nanometric resolution. The previously described methods use externally introduced probes to gain insight into the specimens properties. HR-TEM, CL and EDXS utilize electrons as a probe, NSOM uses photons and AFM uses a sharp nano-tip which interacts with the specimen surface in an elastic regime. While Atom Probe Tomography (APT) uses the atoms which constitute the specimen as a probe (like SIMS), the APT specimen's geometry allows for not only for the sub-nanometric depth resolution of the SIMS method, but also for a lateral resolution on the atomic scale.

The Atom Probe Tomography technique allows to obtain the three-dimensional positional coordinates of all detected atoms (usually around half the total specimen atoms, due to a detection efficiency around 50%) which constitute a specimen. While being a destructive method and requiring a very specific technique for the preparation of specimens (Gault et al. (2012)), it allows to perform three-dimensional chemical microscopy on the nanometric scale.

However APT itself does not provide optical information like NSOM or CL does. The lack of this dimension of investigation represents a drawback of the isolated APT-method when compared to coupled AFM/NSOM (Li et al. (2019)) and TEM/CL techniques (Edwards and Martin (2011)). An upgrade of the general APT set-up which allows to harvest PL information during the performance of an APT experiment is presented in Section 1.3.

The practical challenge for such a method is to correlate the APT specimen's PL response with the development of the geometry which the specimen undergoes during its APT investigation. The PL signal emitted from a laser-excited APT specimen depends mostly on compositional and structural factors, as well as on the environmental parameters which are characteristic for the APT experiment itself (electric field, specimen

geometry, mechanical stress, temperature).

1.2 Atom Probe Tomography

APT is a destructive analysis method, which gives access to the 3D positions of the atoms which used to constitute the specimen. By successively removing atoms from the specimen's surface using a high electric field, the original position of every field evaporated atom can be reconstructed and the chemical nature of every atom can be characterized. A very sharp tip-shaped specimen is positively biased with a voltage which is sufficiently high to remove cations from the tip surface. These cations are then detected using a position sensitive ion detector, which gives information on the location on the surface from where the ion is emitted. By applying a pulsed excitation, the time-of-flight of every ion is calculated, from which the chemical nature of the detected ion is obtained.

In Section 1.2.1 the physical basis of the technique as well as instrumental basis of the method are discussed. Section 1.2.2 shows a summary of historical development of the APT technique.

1.2.1 Physical and Instrumental Basis

1.2.1.1 Field Evaporation

The operational principle of the APT method is the field enhancement which takes place when applying a high voltage onto a very sharp tip-shaped specimen (APT-tip). This "sharpness" expresses itself as a low radius of curvature at the tip apex (r_0). The electric field which is present at the surface of a tip apex when a bias voltage V is applied to the specimen can be calculated from this radius of curvature:

$$E = \frac{V}{k_f \cdot r_0} \tag{1.10}$$

The field reduction factor k_f takes into account the tip geometry. While $k_f = 1$ applies to a spherical capacitor biased with the voltage V, actual APT-tip shapes represent a deviation from this situation which can be described with $k_f > 1$. For actual APT-tips k_f usually takes values around 5 (Sakurai and Müller (1973)).

For an APT-tip with a radius of curvature around 100 nm, the application of a high voltage (1 kV) leads to high electric fields ($2 \cdot 10^9$ V/m) close to the apex. Depending on the bias different physical phenomena can occur. At negative bias, such high electric fields lead to the emission of electrons from the specimen (Fowler and Nordheim (1928)).

At sufficiently high positive bias ($E \approx 10^{10}$ V/m) cations are emitted from the proximity of the apex (Müller et al. (1968)).

This process of field evaporation is usually explained by the image-force model (Müller (1956)), which assumes that the field evaporation of a surface ion with the charge ie is thermally driven and has the activation energy:

$$Q_i(E) = \Lambda - iW + f(E) + \sum_{j=1}^{i} I_j \tag{1.11}$$

where Λ is the heat of sublimation, W is the electron work function for metallic specimens and the electron affinity for semiconductor materials and I_j is the evaporated ion's $j-$th ionization energy. $f(E)$ is a function, which describes the reduction of the activation energy of the specimen's surface atoms with a rising electric field and can be considered to decrease linearly with a rising electric field (Tsong (1978)). While the work function is independent of the field evaporated species, the ionization energy and the heat of sublimation depend on the physical properties of the field evaporated ion.

With the activation energy known, the evaporation rate can be calculated:

$$\phi_i(T, E) = \phi_0 \cdot \exp\left(\frac{-Q_i(E)}{k_B T}\right) \tag{1.12}$$

where ϕ_0 is the product of the vibrational frequency of the surface atoms and the number of atomic sites which qualify for thermal field evaporation. The ions which are field evaporated according to Eq. (1.12) can be detected by a position sensitive detector whose impact-position data gives information on the original position of the evaporated ion on the tip surface.

While other evaporation mechanisms are suggested for the field evaporation of APT specimens, the thermal process described here still is considered to be dominant (Kelly et al. (2014a)). In the special case of semiconductor materials evaporating during their APT analysis this simple picture is complicated by a variety of physical effects such as the inhomogenous absorption of laser energy, electric field induced charge carrier accumulation and modifications of the band structure.

1.2.1.2 Mass Spectroscopy

While a specimen which is field evaporated under a static DC-voltage is able to provide data about the positions of the evaporated atoms, their chemical nature remains ambiguous. In order to characterize the detected ions chemically a pulsed excitation,

which triggers the field evaporation of the surface atoms is used. During the application of a base voltage, which is insufficient for its field evaporation, additional laser (Kellogg and Tsong (1980)) or voltage (Müller et al. (1968)) pulses can be applied to the tip in order to cause a surface atom's evaporation to be temporally correlated to this excitation. The pulsed excitation of the specimen gives a reference for the point in time of the occurence of an evaporation event. This allows access to the time of flight of the respective evaporation event.

These field-emitted cations are used as the probe during the Atom Probe Tomography study of a specimen. Since the electric field falls off in close proximity to the tip surface (≈ 1 μm) a cation with the charge $+q$ can be considered to reach its maximum kinetic energy (qV) right at the tip surface, when compared to the usual distance between the specimen and the position sensitive ion detector ($l \approx 10$ cm). Using this estimation the velocity of the cation can be considered to be constant during the entire time-of-flight (t):

$$qV = \frac{m \cdot v^2}{2} = \frac{m \cdot l^2}{2 \cdot t^2} \Rightarrow M = \frac{e \cdot m}{q} = eV \cdot \frac{2 \cdot t^2}{l^2} \tag{1.13}$$

Where e is the elementary charge. With the voltage V, the time-of-flight t and the flight-length l known, the mass-to-charge ratio M [amu] can be calculated. The mass-to-charge ratio allows for the chemical identification of the evaporated atom.

However, the frequency of the pulses which are used to excite the specimen cannot be chosen to be arbitrarily high. In the practice of time of flight spectroscopy every detection event is assigned to the excitation pulse which has direcly preceeded it in order to calculate its time of flight. Thus the time between two exciting pulses has to be longer than the time of flight of the slowest emitted ion in order to properly assign its evaporation to the properly corresponding excitation pulse. At a fixed pulse frequency f the maximum possible time of flight which still ensures the proper attribution of the evaporation event to the pulse is $\frac{1}{f}$. The biggest mass to charge ratio which can be detected from an APT experiment (M_{crit}) can be expressed as:

$$M_{\mathrm{crit}} = \left(\frac{em}{q}\right)_{\mathrm{crit}} = \frac{2 \cdot eV}{f^2 \cdot l^2} \tag{1.14}$$

Eq. (1.14) shows that an APT experiment performed at a high voltage is able to properly identify ions with a higher mass to charge ratio. The voltage at which the experiment is performed is however given by the radius of curvature r_0 (Eq. (1.10)) of the specimen and is set to a value that gives the desired evaporation rate of the specimen (Eq. (1.12)).

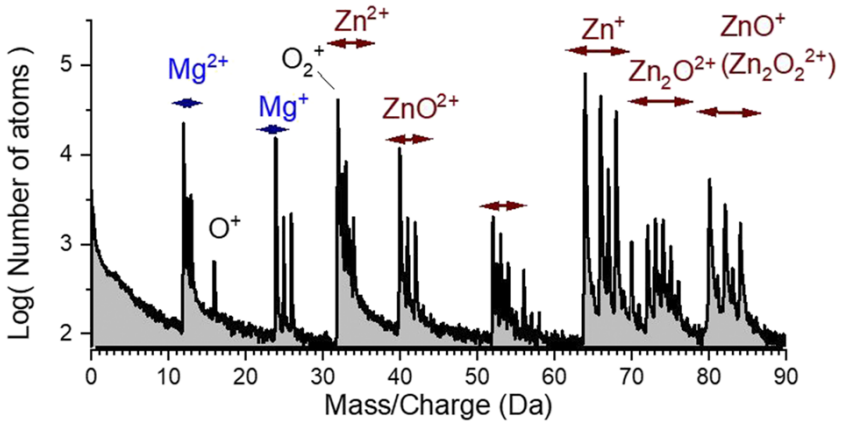

Figure 1.7: Example of a mass spectrum recorded from a ZnO/(Mg,Zn)O specimen (Houard et al. (2020)).

An instrumental parameter which defines the maximum mass to charge ratio of a properly identified ion is the flight length l. Since the flight length is proportional to the time of flight, short flight lengths allow for the identification of higher mass to charge ratio ions. In order to avoid overlap between different evaporated species' mass to charge ratio peaks (Fig. 1.7), l cannot be chosen to be arbitrarily small. Another instrumental parameter (which is much more easily modifiable) is the pulse frequency f. This parameter cannot be chosen to be arbitrarily small since f is proportional to the speed with which an APT analysis is performed. A smaller pulse frequency means that it takes more time to perform an APT analysis with a given amount of detected ions.

An example of a mass spectrum is shown in Fig. 1.7. Since the detected ions are either of atomic (e.g. Mg^{+}, Zn^{2+}) or molecular (e.g. ZnO^{+2}, Zn_2O^{2+}) nature and show different charge states, different species can be measured at the same mass to charge ratio during the same experiment (e.g. O_2^{+} and Zn^{2+}). In such a case, while the contribution of both species to the joint mass peak can be estimated by taking the natural abundance of both species into account, the chemical nature of the detection event remains ambiguous.

1.2.1.3 3D Reconstruction

With the position sensitive detector providing two-dimensional information on the specimen surface's properties, obtaining the correct depth positions of the detected ions requires a treatment of the detected data with a tomographic algorithm (Deconihout et al. (1994)) the outline of which is described in Vurpillot (2016) and briefly condensed here in order to familiarize the reader with it.

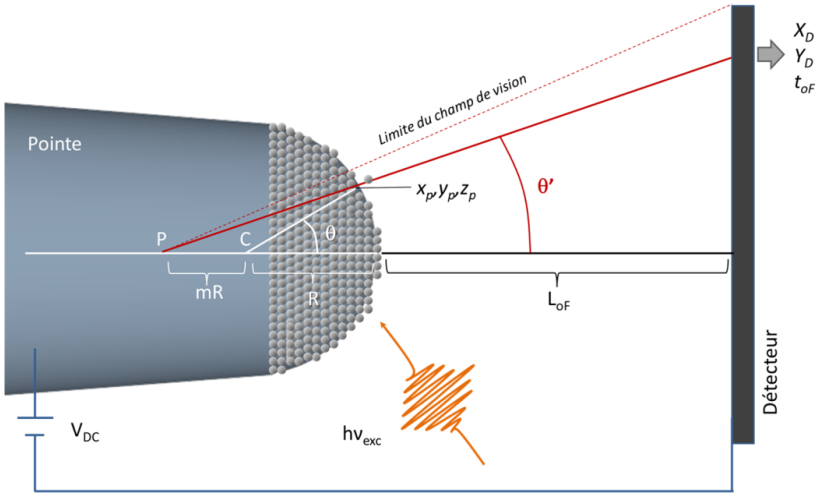

Figure 1.8: Schematic of an APT specimen and the parameters which are important for the three-dimensional reconstruction of the atomic positions (Rigutti (2020)).

The atoms detected by the atom-probe set up are characterized by their impact positions (X_D, Y_D) on the two dimensional detector (Fig. 1.8). By taking the rotational symetry of the specimen and a constant radius of curvature r_0 into account, these coordinates can be transformed into cylindrical coordinates, which give the atom's position on the tip apex (x_p, y_p, z_p):

$$\begin{aligned} \theta &= (m+1) \cdot \arctan\left(\frac{\sqrt{X_D^2 + Y_D^2}}{l}\right) \\ \phi &= \arctan\left(\frac{Y_D}{X_D}\right) \end{aligned} \tag{1.15}$$

where m represents a deviation of the ion's trajectory from that which is expected from a spherical capacitor which originates from the specimen geometry. From these cylindrical angles and the apex's radius of curvature the ion's original position the apex can be calculated:

$$\begin{aligned} x_p &= r_0 \cdot \sin\theta \cdot \sin\phi \\ y_p &= r_0 \cdot \sin\theta \cdot \cos\phi \\ z_p &= r_0 \cdot \cos\theta \end{aligned} \tag{1.16}$$

While Eq. (1.16) gives the original position of an ion which is evaporated from a

static tip apex, the tomographic aspect of the evaluation is introduced by considering that every evaporated atom can be considered to contribute to an increase in depth ($\mathrm{d}z$). This means, that the next evaporated atom has to be considered to have a lowered depth value $z - \mathrm{d}z$, where the gain in depth ($\mathrm{d}z$) depends on the volume of the atom which has caused it (Deconihout et al. (1994)). By successively evaluating the gain in depth for every evaporated atom the correct depth can also be calculated for atoms which are evaporated once the initial tip surface has already been fully evaporated. The dataset provided from the APT experiment consists of the original atomic position of every field evaporated atom as well as of every evaporated atom's mass to charge ratio.

1.2.2 Historical Development

1.2.2.1 Field Electron Emission Microscope

The discovery of the electron by Wiechert (1897) and Thomson (1897) has shown the quantization of the electric charge. It has also opened questions about the possibility to remove these negatively charged particles from a body. Using the theory developed by Fowler and Nordheim (1928) it has been shown, that electron emission can be expected to occur at dc-electric field strengths around 10^9 V/m under negative bias.

The prospect to create electron emission from a specimen's excitation by a high electric field was especially interesting for those scientists interested in electron sources. Such high electric fields can be generated by applying a high voltage to a specimen with a small radius of curvature. While the electron emission resulting from high electric fields present at low radius of curvature specimen has been well established as a way to generate electron beams (Crewe et al. (1968)), the electron emission from such tip-shaped specimen can also be used to obtain information on the physical properties of the material which constitutes the specimen.

The Field Electron Emission Microscope (FEEM) (Fig. 1.9) allows the analysis of the field-emitter. By applying a high negative bias ($\approx$4 kV) to a specimen with a small radius of curvature ($\approx$1 μm), electrons are emitted from the specimen (Müller (1937)). The high voltage accelerates electrons from the negatively biased tip towards a phosphorescent screen, which serves as their detector. Since any gas atoms present in the chamber can be ionized by the emitted electrons and then accelerated towards the specimen, the presence of many gas molecules inside of the measurement chamber causes a roughening of the specimen surface. A pump is used in order to reduce the pressure inside of the FEEM chamber down to 10^{-5} Pa.

Fig. 1.10 shows a result of these early FEEM experiments. Since the work function

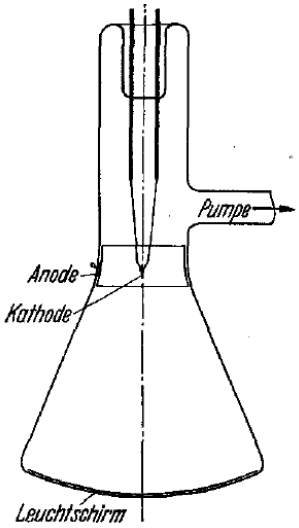

Figure 1.9: The Field Electron Emission Microscope developed by Müller (1937). The electrons emitted from the anode are detected by the phosphorescent screen ("Leuchtschirm").

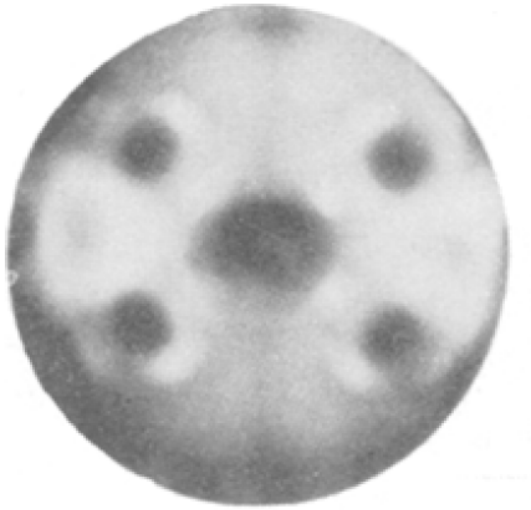

Figure 1.10: FEEM image of a [110]-oriented Tungsten specimen (Müller (1937)).

depends on the crystal orientation of the tip surface, the varying brightness in this photograph represents a stereographic projection, of the crystal's zone axes. Like this crystallographic information of the specimen is obtained using the FEEM technique.

1.2.2.2 Field Ion Microscope

With the FEEM technique becoming more established, the inversion of the applied bias became a topic of research. First experiments utilizing a positive bias applied to the specimen resulted in specimen fracture at an electric field around $7 \cdot 10^9$ V/m (Müller (1943)).

At a higher positive bias ($\approx 10^{10}$ V/m) however the emission of positively charged ions from the specimen is expected. These high electric fields are usually achieved by reducing the specimen's radius of curvature from ≈ 1 μm (FEEM) to ≈ 0.1 μm. The idea of a Field Ion Microscope (FIM) was first realized by Müller (1951). In order to achieve an ion current which is sufficiently high to create an image on the phosphorescent screen, Hydrogen gas ($p = 0.1$ Pa) is introduced into the chamber for Müller's original design. Due to their lower activation energy these Hydrogen molecules are first adsorbed to the specimen and then field desorbed instead of the atoms which constitute the specimen

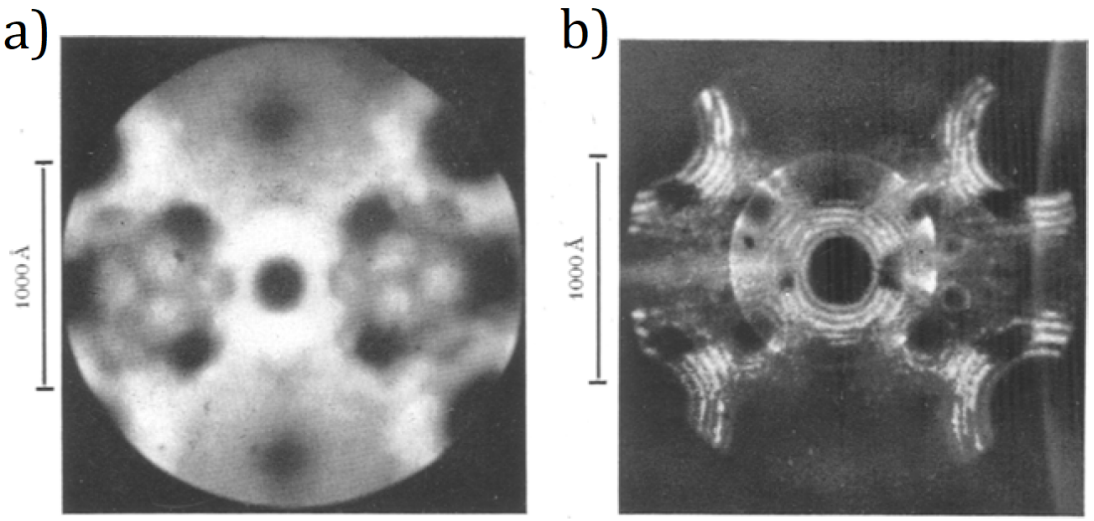

Figure 1.11: Comparison between a FEEM a) and a FIM b) image recorded from the same Tungsten specimen Müller (1951).

(Tungsten).

Compared to the FEEM, the FIM allows an improved resolution of surface features. Since an ion's mass is much larger than the electron mass, the thermal tangential velocity of a field emitted ion is much lower than for an emitted electron. Due to the tangential velocity being the main source of error in lateral resolution, the FIM technique allows for an improved resolution of spatial features of the specimen surface. Fig. 1.11 shows a direct comparison of a FEEM and a FIM image of the same Tungsten specimen. The improvement of the surface's features' resolution is obvious. While the FEEM detector (Fig. 1.11 a)) only shows the general location of the specimen's zone axes, the FIM experiment gives access (Fig. 1.11 b)) to the terrace-like nature of the specimen surface. The bright rings around the zone axes represent the surface terrraces, which are easily field evaporated due to the low binding energy, which they experience on their exposed positions. The clear point-like imaging on the Phosphorescent detector comes from the ionization of imaging gas atoms close the tip surface and is widely considered to be the first verified detection of isolated atoms.

1.2.2.3 Early Atom Probes

While the FIM method gives crystallographic information on the specimen by providing the zone axies of its surface, it does not give any information on the chemical constitution

of the sample. By applying a sufficiently high DC voltage onto a specimen which is located inside of the high vacuum that does not contain any imaging gas atoms, instead of these imaging atoms the specimen's constituent atoms can be ionized and be accelerated towards the detector. While this method does not allow for a the clear imaging of the specimen's zone axes of the FIM method, the analysis of the field evaporated surface atoms can be used to obtain chemical information of the specimen.

Time-of-flight spectroscopy of the field evaporated ions allows to identify the chemical nature of the evaporated atoms. By applying voltage pulses, the time-of-flight of the ions which constitute the FIM signal is measured Müller et al. (1968). In the context of this work a Tungsten specimen is analysed utilizing $7 \cdot 10^{-3}$ Pa Helium partial pressure in order to obtain FIM images of the specimen. Afterwards, the He-gas supply is cut off reducing the total chamber pressure to 10^{-4} Pa. Under these low pressure conditions the Tungsten atoms which constitute the specimen's surface are field evaporated. From their time-of-flight, the mass-to-charge ratios of the field evaporated species are calculated and the chemical nature of the field evaporated species (e.g. W^{3+} and WO^{3+}) is determined.

These early atom probes usually had very long flight length (82 cm for Müller et al. (1968)). While this is beneficial for the achievement of a good time-of-flight resolution (and a good thus mass-to-charge ratio resolution), the part of the specimen surface from where the atom's trajectories are leading towards the detector is only a small fraction of the total surface. This means, that most of the field evaporated surface ions are inaccessible to the detection system.

The next evolutionary step in the development of the imaging Atom Probe was the introduction of instruments with much smaller flight lengths (Panitz (1973)). By the reduction of the flight-length down to 10 cm, it became similar to the diameter of the photomultiplier detector (7.5 cm) in value. This modification allows the study of a much larger fraction of the tip's surface atoms, resulting in a higher field of view of the short-flight-length atom probe.

Another modification of the previously used atom probe set-up introduced in Panitz (1973) is that the voltage pulse is not applied to the specimen, but to an electrode that lies between the specimen and the detector. This modification allows for the application of the voltage pulse to the tip apex without the need for it to propagate through the specimen. This set-up also allows operation with introduced imaging gas as well as under ultra-high vacuum (UHV) conditions. Utilizing high gain on the phosphorescent screens allows for the detection of field desorption images under UHV conditions. By time-gating, this instrument allows to record the field desorption images of only a specific species.

While this time gating allows to separately record field desorption images of the

different species that constitute the specimen, this approach only allows to identify the chemical nature of a select mass-to-charge ratio window at any given time, while the entire rest of the field evaporation signal is lost.

1.2.2.4 Position Sensitive Atom Probes

In order to allow the atom-probe technique to assign chemical information to every single detection event the position sensitive atom probe was developed (Cerezo et al. (1988)). By using a time-resolved position sensitive position sensitive detector the time of flight of every single evaporated atom as well as its impact position is recorded. The electrons generated from the MCP are then collected using an elaborate multi-anode set-up, which grants access to the impact positions of the ion.

The technique was further improved by the construction of an alternative multi-anode set-up, where a 10×10 anode grid is placed behind a multi-channel plate (MCP) (Bostel et al. (1989), Blavette et al. (1993), Deconihout et al. (1993)). Over a total detector area of 10×10 cm, a total of one hundred anodes with a size of 1×1 cm each are deposited on a glass support. These anodes are separated by gaps (0.1 mm), in order to ensure that no charge can be transfered between them. The basic working principle is that the amount of collected charge is measured at every anode. By evaluating the charge distribution on the detector, the impact position is calculated. The distance between these anodes and the MCP, as well as the bias voltage between these objects can be varied in order to properly calibrate the instrument.

In both previously presented detectors the collection of the generated charges represents a challenge for the accurate measurement of the timing information. The development of the delay-line detector (Da Costa et al. (2004)) has improved the performance for multi-hit detection detection of the APT's position sensitive detector set-up. This detector operates by placing two metallic wires behind the MCP plate. Two insulating rods are mounted on the edges of the detection area. One wire is mounted to the both insulating rods in a way that it spans the entire detection area. After winding the wire around one of the rods it is guided back to the other rod. Repeating this step results in the coverage of the entire detection area much like for a weft in weaving. The other wire in mounted in the same way, but with its insulating rods perpendicular to those of the first one. The MCP generated electrons are caught by these biased wires and propagate along them. By measuring the difference between the arrival times of both electron clouds the impact position is calculated. This technique allows for a great improvement of the spatial resolution of the APT-system.

1.2.2.5 Laser-assisted Atom Probe Tomography

While voltage pulses allow for a great control of the field evaporation of metals, systems with much lower electric conductivity pose a different challenge. By utilizing laser pulses insted of ns-voltage pulses in order to trigger the field evaporation of the specimen atoms, the problems coming with an electrical pulse propagating through a high-resistance specimen can be avoided.

The interaction between positively biased nanotip specimens and a light source was first studied in the context of optically excited FIM experiments (Niu et al. (1977)). In the scope of this work a Mercury lamp ($P = 200$ W) is used to excite a Tungsten specimen. In order to study the influence of the Mercury lamp illumination on the evaporation rate during a FIM experiment (imaging gas: Anthracene 10^{-4} Pa), a 13 Hz beam chopper is used. By averaging over many chopper cycles, the effect of the Mercury lamp illumination could be estimated, showing that the illumination of the specimen is especially impactful for the ion count rate at low applied voltages. This behavior was explained by taking into consideration the effect of the light excitation on the tunneling probability and its interplay with the field strength close to the apex. This idea of a photoexcitation directly in aiding the tunneling process was first introduced in Tsong et al. (1976) and would later become known as the concept of "Photo-ionization".

With a proof of optical excitations being able to increase the ion emission probability, optical excitations were shown to be viable for the pulse triggering for atom probes experiments. Using laser pulse triggering mass spectra of specimen that contain gas molecules adsorbed to surface were recorded. By evaluating the chemical nature of the emitted ions from the time-of-flight information surface reactions of ethylene on a silver tip under laser pulse excitation were studied as a function of various parameters (applied voltage, specimen temperature, gas pressure, laser power, repetition rate and wavelength) in Nishigaki et al. (1979).

Laser pulsing has shown to give a good resolution for the mass spectrum of adsorbed gas molecules. Drachsel et al. (1980) have shown, that the width of the recorded time-of-flight peaks (adsorbed Xe) is similar to the time-length of the ns-laser pulse. A similarly good quality of the results for the time-of-flight resolution have been obtained for the field evaporation of bulk materials (Kellogg and Tsong (1980)).

The development of the laser-triggered field evaporation technique has opened the material domain of non-coductive materials to atom probe analysis (Cerezo et al. (1986)). The utilization of short fs-laser pulses has shown to be beneficial for the mass-resolving power of the APT experiment (Gault et al. (2006)).

Laser-assisted APT (La-APT) is based on the thermal excitation caused by the intraband relaxation of laser-generated photo-carriers . This thermal relaxation leads to a heating up the specimen during the application of the laser pulse. Afterwards the heat takes some time to dissipate within the specimen, leading to an elevated temperature of the specimen for some time after the laser pulse has already ceased to excite the APT tip. This leads the tip's apex region emitting ions for some time after the laser pulse has already passed. This delayed field evaporation of surface atoms leads to the appearance of thermal tails within the mass spectrum when performing La-APT experiments (Vella (2013)).

1.3 Correlative APT & PL Analysis

With the establishment of the (laser-assisted APT) La-APT technique semiconductor materials have been enabled for a facilitated investigation. A characteristic of semiconductor material is that they have interesting optical emission properties. With this material class being laser-excited during the an La-APT experiment, the semiconductor specimen's optical response has become a subject of study as well.

The specimen's APT-information can be correlated with its optical response in different ways:

- Investigation of an APT specimen by another measurement technique before its field evaporation (ex-situ)
- Measuring the specimen's optical response inside of the APT instrument without its field evaporation (in-situ)
- Collection of the specimen's optical information during the field evaporation of an APT specimen in the context of an APT experiment (in-operando)

For a joint measurement of the optical and structural properties of the specimen the in-operando approach is used. Compared to the previously discussed methods (Section 1.1.3) which allow for a correlative analysis of a specimen (AFM/NSOM and TEM/CL) this method offers a new dimension to localize the original region of PL. The APT component of the analysis allows for the removal of whole regions of the investigated specimen. While AFM and TEM based techniques study a static specimen, La-APT coupled with PL allows to better localize the region from where the specific PL signals are emitted.

In this section an overview about recently performed experiments investigating the correlative analysis of semiconductor specimen by APT and Photoluminescence (PL)

spectroscopy is presented.

1.3.1 Preliminary Work

The idea to perform a measurement that correlates APT and PL measurement results was first brought forward in Rigutti et al. (2013). In this work the behavior of a ZnO microwire mounted on a Tungsten tip is studied using a μ-PL set up.

Since the investigated ZnO microwire length of about 100 μm is very large compared to the estimated spot size of 2 μm, distinct portions of the long chunk are able to be illuminated separately. By moving the laser spot along the chunk's main axis, PL spectra were recorded as a function of the position of the excited region. After the performance of this first $\mu-$PL experiment, the chunk was reintroduced into the FIB chamber and underwent annular milling, turning it into an APT tip. This annularly milled tip's PL was also investigated for different laser spot positions along its main axis. Comparing the PL response of the chunk and the milled tip shows that the process of annular milling deteriorates the intensity of the specimen's PL response. After the milled tip's PL-investigation it was succesfully field evaporated and analysed using an APT-set up.

Another correlative study was performed on GaN quantum dots embedded inside of AlGaN (Mancini et al. (2017)). In this study, the quantum dot's (QD) nanometric geometry was obtained from La-APT and Electron Tomography information. These results were then used to perform simulations of the QD's emission emission energies. By showing that the simulated PL energy, which best describes the experimentally observed result is obtained by taking interface fluctuations at the bottom of the QD into account for the simulation, additional indications for the existance of such interface fluctuations in the specimen were given.

Since for these two works, the PL measurement set-up and the APT chamber are separated, the PL investigation and the APT investigation had to be performed separately. Thus any PL spectrum can only be recorded for a single specimen geometry. Both these experiments thus allow for a ex-situ information of the specimen's optical and APT-obtained information.

1.3.2 The Photonic Atom Probe

By enabling the simultaneous measurement of the specimen's PL and APT signal, the Photonic Atom Probe (Houard et al. (2020)) allows for the performance of in-situ and in-operando experiments. Being able to perform an La-APT measurment simultaneously with a PL-spectroscopy experiment, while having the specimen at a fixed position, the

Photonic Atom Probe (PAP) allows the recording of the specimen's PL response during the entire duration of an La-APT measurement. A description of the PAP set-up and its working principles is presented in Section 2.2.

The PAP has already shown a multitude of possible applications for the study of correlative APT-PL analyses, as well as studies exploiting the extreme electric field and mechanical stress conditions, which are caused by the presence of the high electric field close to the tip's apex.

The influence of the extreme mechanical stress on the optical properties of a material was first studied by Rigutti et al. (2017). This method of investigation can be considered to be a form of contactless piezo-spectroscopy, where the high voltage induced by the application of the dc-voltage, which is required to perform APT experiments, leads to an application of a mechanical stress, while the PAP allows the study of the stressed material by spectroscopy. In this work, the PAP was used in order to study the PL signal emitted from localized nitrogen-vacancy (NV^0) complexes in diamond. The NV^0-complexes introduces two degenerate localized states into the system's energy band gap, to which any photo-electrons can relax. The application of uniaxial stress to the localized NV^0-complex causes its states' degeneration to be lifted, resulting in a splitting of the transition energies, which manifests itself as a splitting of the PL signal. By controlling the voltage, which is applied to the specimen, the splitting can also be influenced. Utilizing this piezo-spectroscopic method, mechanical stresses of up to 7 GPa were verified to be present inside of an APT specimen, which is under high voltage.

Another example of localized photoemitters embedded inside of an APT specimen being used as a probe of the stress states present in the specimen is shown in Dalapati et al. (2021). For this work a ZnO/(Mg, Zn)O quantum well (QW) is used as a localized PL source. This QW is aligned roughly perpendicular to the tip main axis. This results in the tip apex approaching the QW, while the APT field evaporation successively removes atoms close to the tip's apex. The dependence of the PL-energy emitted from the QW was studied while varying the voltage applied to the tip's apex. The resulting red-shift of the localized emitter's PL signal is explained by the modified stress states. This explanation was made by utilizing strain-dependent band theory (Langer et al. (1970)), which was used to estimate the stresses present close to the QW from the energy shifts of the PL signal. Additionally to the previously mentioned voltage induced strain effects, lattice mismatch (between the ZnO QW and the (Mg,Zn)O barrier material) induced strain effects were also taken into account. From these considerations, the stress, which is present close to the tip's apex is estimated to be 1.25 GPa.

Dimkou et al. (2020) is a PAP study of an InGaN/GaN multi QD system. In this

work, the QDs present in the APT specimen were successively field evaporated, while the PL signal was being recorded continuously. In the initial states in which the system is found (with all QDs present), the optical signal of all QDs forms broad peak, in which the contributions of the different QDs cannot be distinguished. In the later states, when most of the QDs have already been field evaporated, the spectral components of the different QDs become more and more pronounced, until finally single QD's PL signals can be distinguished by their energies. In the scope of this study, the laser-power dependence of the PL-intensity of the GaN barrier material and the InGaN QD was studied. It is shown, that the barrier material shows a linear dependence of the PL-intensity on the laser-power, while the InGaN QD's PL-intensity saturates at higher laser-power.

In Di Russo et al. (2020) the optical response of a specimen consisting of a series of (Mg,Zn)O QWs with varying thicknesses is studied. By calculating the difference of the subsequently recorded PL spectra it is shown that the PL response of the QWs, which have a varying thickness, can be distinguished. By considering the change of the specimen's total PL response, shortly before a specific QW starts to evaporate, this method of differential spectroscopy is shown to allow the measurement of the PL energy of said QW. Applying this method to every single QW of the system yields the PL energy of the four thinnest of the five QWs embedded inside of the specimen (0.5 nm, 0.9 nm, 1.8 nm, 3.2 nm). The thickest QW (4.0 nm) has a significant overlap with the PL signal originating from the ZnO substrate, resulting in its energy not being available for measurement.

While the PAP-technique has been shown its abillity to provide valuable data on the studied materials as well as on the physical conditions under which APT experiments are generally performed, there still remain some conceptual advances that can be made using this method. Firstly while Dalapati et al. (2021) gave insights into the behavior of the PL-energies that are obtained during the performance of a PAP experiment, the physical meaning of the detected PL intensity was not an object of investigation in that work and remains to be properly interpreted. Secondly the PAP investigation still offers open venues for the investigation of more complex semiconductor-heterostructure devices and the correlation of alloy-composition and doping related optical signals from such a specimen with the APT information which is obtained in-operando.

2. Materials and Methods

In this chapter the practical fundamentals of the thesis are outlined. In the first section, we introduce the two studied material systems which are investigated in the context of this thesis. First we introduce the non-polar ZnO quantum wells (QWs) separated by (Mg,Zn)O barrier material (Section 2.1.1) and then (In,Ga)N Tunnel Diodes (TD) embedded in a GaN-based heterostructure (Section 2.1.2).

Then the physical (Section 2.2.1) and instrumental (Section 2.2.2) fundamentals of the Photonic Atom Probe (PAP) are elaborated on.

In the third section we introduce Finite-Difference-Time-Domain (FDTD) calculations (Section 2.3.1), in order to explain the behavior of the detected Photoluminescence (PL) intensity emitted from a ZnO/(Mg,Zn)O specimen. We present the evaluation methods for the numerical simulations' results which are used to study the effect of an evolving idealized tip geometry (Section 2.3.2) on the propagation of the exciting laser pulse and the emitted PL. By simulating the influence of the specimen's field evaporation on the laser absorption (Section 2.3.4) and its PL-emission distribution (Section 2.3.5) properties, a measure of the detected PL intensity is obtained. Finally modulations of the specimen's optical properties which are inherent to the APT experiment are introduced into these FDTD simulations (Section 2.3.3).

Taking into account the limited field-of-view of the PAP's PL detection set-up (Section 2.3.7) allows to relate these results to the instrumental conditions of the PAP. Finally a method to gain insight on the polarization information which is contained in the detected PL signal from the FDTD simulation is presented (Section 2.3.8).

2.1 Material Systems

In the context of the present work, two distinct material systems are studied. Firstly (Section 2.1.1) ZnO QWs embedded in (Mg,Zn)O barrier material were studied in order to characterize the general behavior of PL intenstiy which is detected by the PAP set

up. The studied system consists of two ZnO QW, of which only one shows a PL signal that is detectable by the PL detection set up of the PAP (Dalapati et al. (2021)). This lack of PL emission from the other QW is attributed to damaging due to focussed-ion-beam (FIB) preparation. By utilizing this specimen as a model system of a localized PL emitter in the context of the PAP, the influence of the specimen's field evaporation on the development of the emitted PL intensity is studied in order to characterize the general behavior of a localized PL emitter embedded in the PAP specimen.

The second studied system is a complex semiconductor heterostructure, which is used in order to show, how the PAP allows for a distinction of PL signals, coming from a multitude of emitting regions, each of which are characterized by their characteristic PL energies (Section 2.1.2).

2.1.1 ZnO Quantum Wells embedded in (Mg,Zn)O

ZnO is a wide band-gap (3.4 eV) II-VI semiconductor with a large exciton binding energy (60 meV, Ozgur et al. (2005)). It is possible to produce ZnO thin films by sputter deposition, which represents an inexpensive and relatively simple way for deposition on glass and Si (with a thermally grown SiO_2 surface 1 μm)-substrates (Sundaram and Khan (1997)). These properties make ZnO a promising material system for the production of optoelectronic devices.

A common material system which is used for the production of ZnO-based heterostructures is (Mg,Zn)O. MgO is a large band-gap material (Roessler and Walker (1967)). By adding Mg to ZnO (Mg,Zn)O is created, where Mg and Zn atoms share the same crystallographic sites. The resulting compound has a band-gap energy which lies (depending on the Mg content of the alloy) between the characteristic values of ZnO (3.4 eV) and MgO (7.7 eV). By tuning the Mg content of (Mg,Zn)O, the band-gap of the resulting alloy can be tuned over the possible concentration range Wang et al. (2015).

In the context of this present thesis Finite-Difference-Time-Domain (FDTD) simulations of an ZnO/(Mg,Zn)O-specimen are performed. The dielectric function of ZnO has been measured by spectrometric ellipsometry in Yoshikawa and Adachi (1997). In the context of the FDTD simulations, the dielectric function as described in that publication is used to describe the optical properties of the ZnO phases of the ZnO/(Mg,Zn)O-specimen. The values of the dielectric function of ZnO as a function of the photo-energy (for an electric polarization of the used photons along the ZnO's polar c-axis ([0 0 0 1])) is shown in Fig. 2.1. The (Mg,Zn)O phases are simulated by performing an energy shift on the ellipsometry results. Since the PL energy of the (Mg,Zn)O phase is obtained

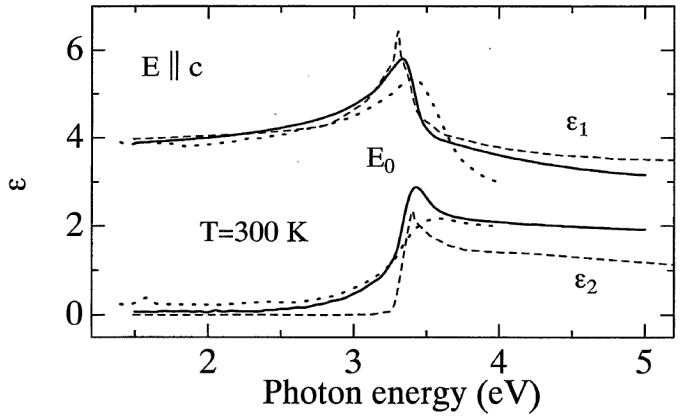

Figure 2.1: Real (ϵ_1) and imaginary (ϵ_2) part of the dielectric function obtained from ellipsometry experiment by Yoshikawa and Adachi (1997) (solid lines).

from the PAP experiment, the dielectric functions obtained from Yoshikawa and Adachi (1997) are energy shifted by the PAP obtained energy difference between the PL energy emitted from the specimen's ZnO phase and its (Mg,Zn)O phase.

While ZnO is a polymorphous material, which is shown to crystalize in the cubic Zinc-blende and Rocksalt structure types, as well in the hexagonal Wurzite structure (Fig. 2.2), the thermodynamically stable configuration under ambient conditions is Wurzite. The Wurzite hexagonal crystal structure ($P6_3mc$) is not centro-symetric. This symetry property of the material manifests itself in the piezoelectric (Lu et al. (2006)) and optically birefringent (Park and Schneider (1968)) properties of the ZnO material system, which are caused by the presence of a polar axis ([0 0 0 1]) of the crystal lattice.

This polar axis also represents the prefered growth direction for the production of ZnO

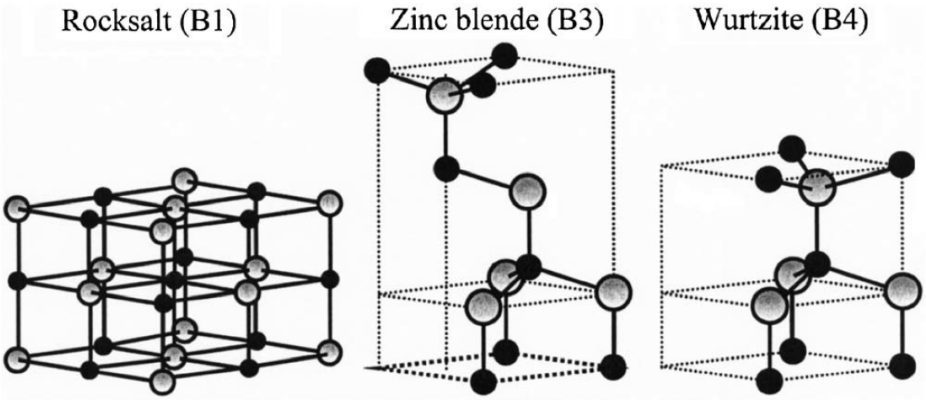

Figure 2.2: The crystallographic morphologies of ZnO (Ozgur et al. (2005)).

thin film systems. However, the polarity of the [0 0 0 1] growth direction has shown to cause the presence of high electric fields ($9 \cdot 10^7$ V/m) at the interfaces between bordering phases (e.g. ZnO/(Mg,ZnO)) grown by heteroepitaxy (Morhain et al. (2005)). Such high internal fields cause the separation of free electrons and holes in grown nanostructures like quantum wells (QWs). Since QWs are frequently used as a basis for light emitting devices, this separation of charge carriers represents an obstacle for their efficient photoemission.

By the growth of ZnO-based heterostructures along the non-polar $[1\,1\,\overline{2}\,0]$-direction, this problem can be overcome. With the $[1\,1\,\overline{2}\,0]$-direction being non-polar there are no internal fields separating exciton within the QW. In Chauveau et al. (2008) it is shown that ZnO-heterostructure growth along the $[1\,1\,\overline{2}\,0]$ a-axis is possible by plasma-assisted Molecular epitaxy (PAMBE). Using an $r-$oriented sapphire substrate and a (Zn,Co)O buffer layer, a double quantum well heterostructure system was grown along the a-axis (Fig. 2.3a).

Utilizing the Photonic Atom Probe (PAP) technique a PAMBE grown ZnO/(Mg,Zn)O heterostructure akin to the structure presented in Chauveau et al. (2008) has been studied (Dalapati et al. (2021)). This structure was grown along the $[1\,\overline{1}\,0\,0]$ (m)-direction which is (like $[1\,1\,\overline{2}\,0]$) a non-polar axis. This results in an absence of high electric field at the interfaces between the heterostructure's different layers. This specimen (Fig. 2.3b) consists of two ZnO QWs with differing thickness ($t_{\mathrm{QW1}} = 2$ nm, $t_{\mathrm{QW2}} = 4$ nm), which are separated by (Mg,Zn)O ($Mg_{0.27}Zn_{0.73}O$) barrier material of 60 nm thickness.

The tip used for the PAP analysis was produced by the standard procedure of focussed ion-beam (FIB) lift-out (Blum et al. (2016)) using a ZEISS Nvision40. This process is exemplified in Fig. 2.4. First the section where the APT tip is to be extracted from is covered with platinum in order to protect the region from unwanted ion-beam irradiation (Fig. 2.4a). This platinum deposition can be performed within the FIB instrument by the insertion of Pt-containing gas into the chamber. By irradiating this gas with the ion beam a Pt layer is deposited. After this two long trenches are cut into the specimen (Fig. 2.4b). A micromanipulator is welded to the region between the two trenches (Fig. 2.4c). Then the lamella is cut off from the sample from which the APT specimen is produced. With the lamella disconnected from the specimen, it can be lifted out (Fig. 2.4d). Then the lamella is guided towards a Tungsten tip, which is used as a structural basis of the APT specimen, using the micromanipulator (Fig. 2.4e). After contact between the Tungsten tip and the lamella has been made, these two objects are welded together using the platinum gas insertion system. The micromanipulator is then separated from the lamella by cutting with the FIB (Fig. 2.4f). By illuminating the specimen with the FIB from

above, the specimen is brought into the desired shape (Fig. 2.4g). Afterwards the milled tip is cleaned using a FIB with a lower acceleration voltage in order to reduce the part of the specimen which is damaged by Ga-implantation (Fig. 2.4h). Finally the tip has to be confirmed to have the geometrical properties which are desired for the APT experiment (Fig. 2.4i).

30 kV Ga ions were used for the cutting processes, followed by a cleaning step using an acceleration voltage of 2 kV. This preparation method was developed in order to allow for PL-emission from QW#1 as well as from the (Mg,Zn)O barrier material. Due to Ga-induced damages no PL emission from the top QW#2 is detectable for any FIB-prepared APT specimens.

Since FIB-irradiation causes a modification of an atom-probe tip's material properties (Rigutti et al. (2013), Vella et al. (2018), Bogdanowicz et al. (2018)), the lowered cleaning voltage (and resulting lowered penetration depth) serves to preserve the optical properties of the specimen.

In Dalapati et al. (2021) it is shown that the PAP recorded PL signal of the QW#1 contains valuable information about the voltage-induced mechanical stresses present in the PAP specimen. Since the electric field has been shown to decline in the very close

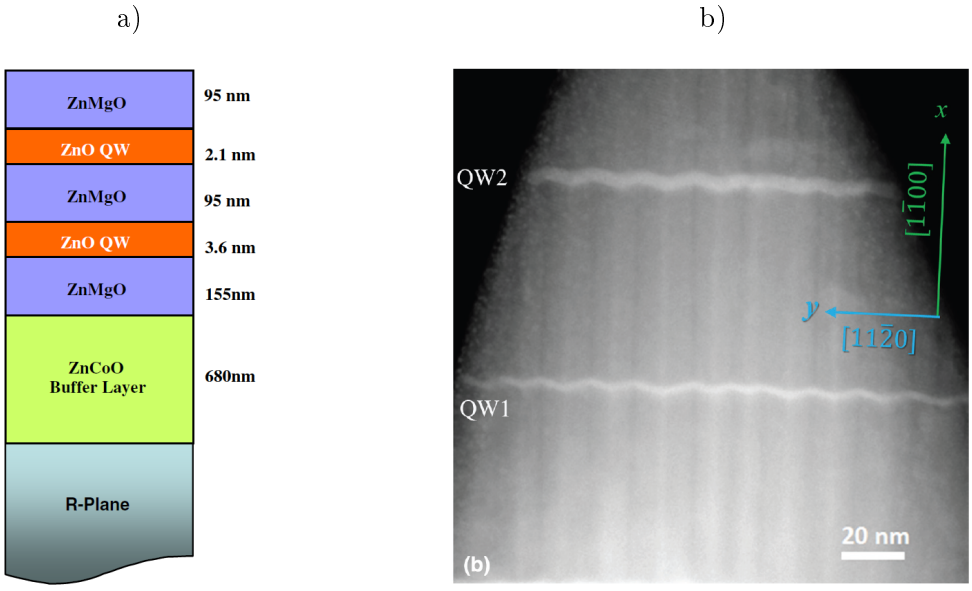

Figure 2.3: a) The layer-order of the ZnO/(Mg,Zn)O double QW heterostructure studied in Chauveau et al. (2008). b) A transmission electron micrograph generated from a specimen lifted out from the same substrate as the specimen described in Dalapati et al. (2021).

proximity of the tip apex (Silaeva et al. (2014)), electric field effects on the PL emission energy are not taken into consideration. QW#2 has not shown any PL emission in this experiment. Varying the voltage applied to the tip is shown to modify the emission energy of both the QW#1 and the (Mg,Zn)O barrier material (Fig. 2.5). Both PL energies experience a red shift with a rising applied voltage. This voltage dependent experiment was performed for applied voltages, that are sufficiently low not to cause any field evaporation of the specimen.

Also the energy of the QW#1's PL signal was recorded during the performance of an actual PAP experiment, in the context of which the specimen itself is being field evaporated (Fig. 2.6). During the specimen's field evaporation (Apex position→0) the energy of the photons emitted from QW#1 also experiences a red shift.

The reason for both of these red shifts (with rising voltage and with progressing

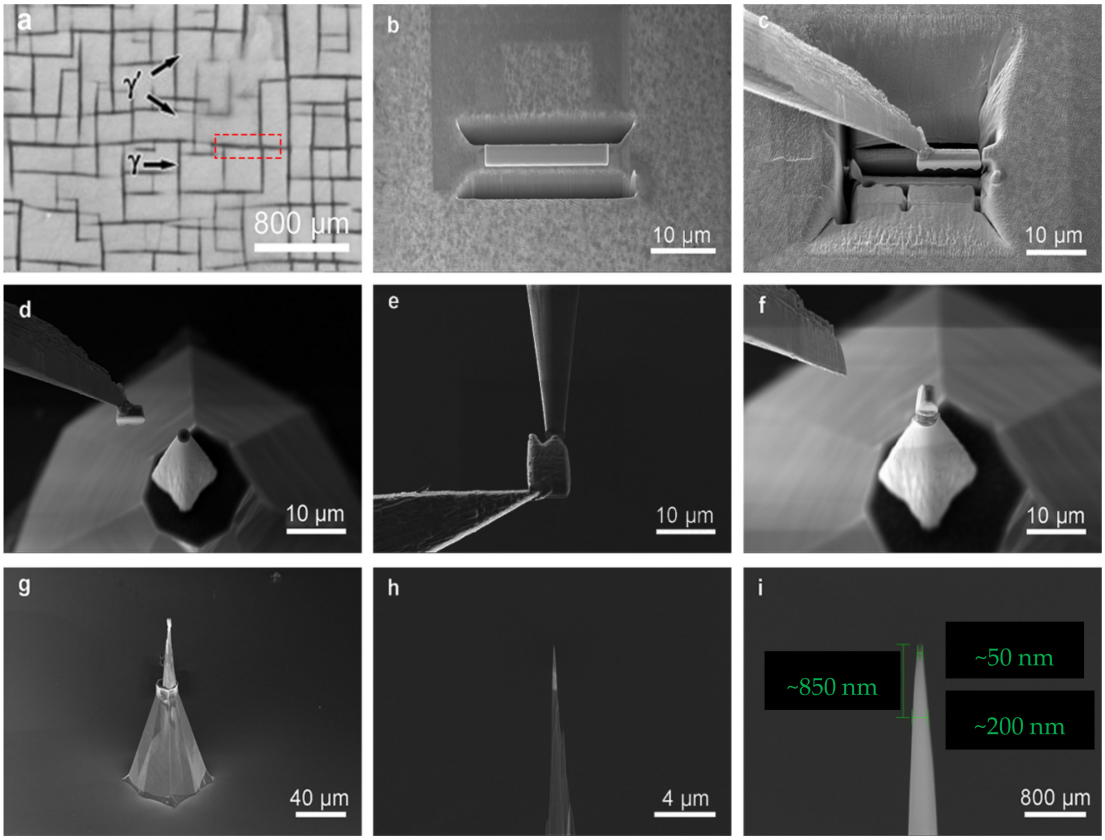

Figure 2.4: Example of the standard lift-out APT specimen preparation (Al/Ni-system). (a) Platinum deposition, (b) cutting, (c) fine cutting, (d) lift-out, (e) welding, (f) separation, (g) annular milling, (h) cleaning, (i) confirmation (Qiao et al. (2022)).

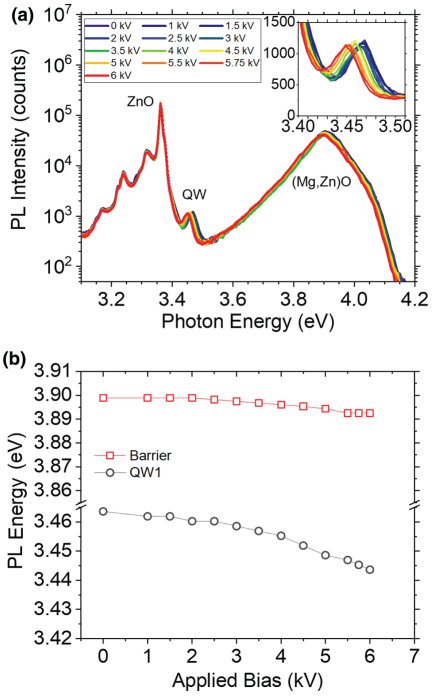

Figure 2.5: PL emission of the (Mg,Zn)O specimen studied in Dalapati et al. (2021). a) the PL spectra and b) the development of the emission energy with rising bias voltage of the PAP-tip.

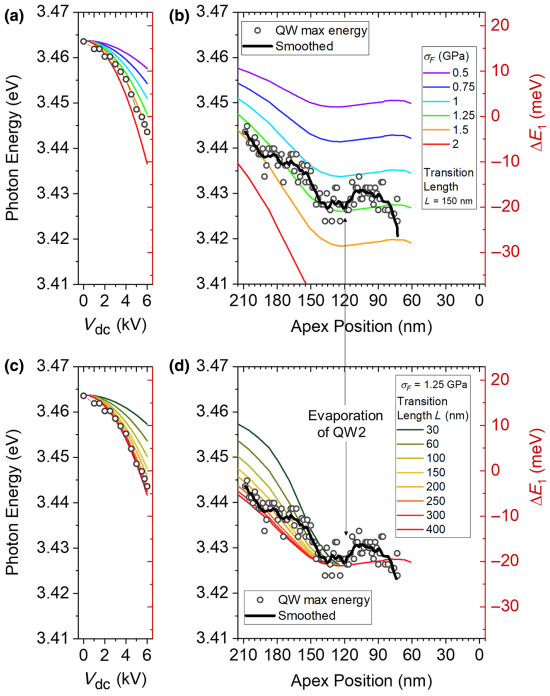

Figure 2.6: QW#1's PL and its description by a $k \cdot p$ calculation under the consideration of a fixed Maxwell stress (a,b) and a fixed transition length (c,d). (Dalapati et al. (2021))

specimen evaporation) of the PL energy is found in the modification of the mechanical stress inside of the specimen. The mechanical stress at the position of the QW#1 rises with an increasing applied voltage, as well as, with the QW#1 coming closer to the specimen apex during the specimen's field evaporation.

Utilizing a quasicubic $k \cdot p$ effective mass Hamiltonian theory (Langer et al. (1970)) the modification of a material's band structure by mechanical strains was calculated. The application of this method takes into account both the mechanical strains induced by the applied voltage and the lattice-mismatch induced strains. The Maxwell stress at the specimen's apex surface (σ_F), which is induced by the accumulation of holes in the proximity of the tip apex and the transition length (L), which describes the length over which the stress decays at an increasing distance from the apex are essential parameters for the calculation of the strain dependent band-gap energy. Both these parameters cannot be easily obtained from APT data. Instead the PL data obtained from the PAP experiment is utilized to estimate their values.

Fig. 2.6 shows the transition energies obtained from this calculation compared to the measured PL energies. Since the values of both σ_F and L are unknown and both parameters influence the calculated photon energies, there is a set of different values for both of these which is able to explain the experimental data. In order to solve this, the value of either L (Fig. 2.6 a,b) or σ_F (Fig. 2.6 c,d) is considered to be fixed. Like this the development of the photon energy can be plotted as a function of the dc-voltage and the apex position for different values of the variable parameter and compared to the experimentally obtained PL energies. $\sigma_F = 1.25$ GPa and $L = 150$ nm represents a set of parameters, which gives a good description of the experimental data.

In Dalapati et al. (2021) the dependence of the QW#1's and the (Mg,Zn)O barrier material's PL energy on the specimen's surface electric field induced mechanical strains is presented. Like this the evolution of the PL energy during the specimen's field evaporation is explained as well. In the context of this present thesis the dependence of the emitted PL intensity on the progressing field evaporation is studied. This analysis is performed by comparing the experimental dataset, which was obtained in the context of Dalapati et al. (2021), to a series of Finite-Difference-Time-Domain (FDTD) simulations of the tip which were performed in the context of this thesis. By investigating the PL emission originating from the QW#1 insights on the behavior of the detected PL intensity which is emitted from a localized emitter during the performance of a PAP experiment are gained.

2.1.2 (In)GaN Tunnel Junction Laser Diode

III-Nitrides (AlN, GaN and InN) have been shown to be a material class of very interesting electro-optical properties. Especially the possibility of creating intermediary alloys between these pure compounds ((Al,Ga)N, (In,Ga)N and (Al,In)N) has been shown to open a rich space for band-gap and lattice engineering. With the hexagonal Wurzite crystal structure (Fig. 2.7) being the stable configuration of AlN, GaN and InN at room temperature (Trampert et al. (1997)), these intermediary alloys originating from this material class allow for a large band-gap and lattice parameter space being available for this system (Fig. 2.8). The available wavelengths for interband emission from III-Nitrides range from short-wavelength-infrared (1770 nm) for pure InN to UV-C (200 nm) for pure AlN.

The production of high quality InN specimen has been an issue for a long time. Poor quality InN specimen show an absorption edge at 1.89 eV, while not showing a PL response at this energy. This unusual behavior of the optical properties of InGaN is

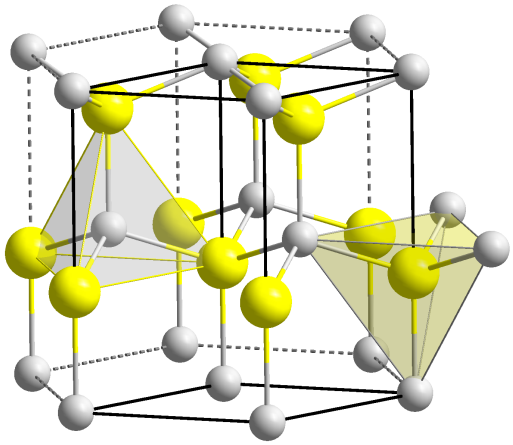

Figure 2.7: The Wurzite crystal structure. Each group III element (yellow) is surrounded by a tetrahedron consisting of N atoms (grey) and vice versa. (Wikimedia (2008))

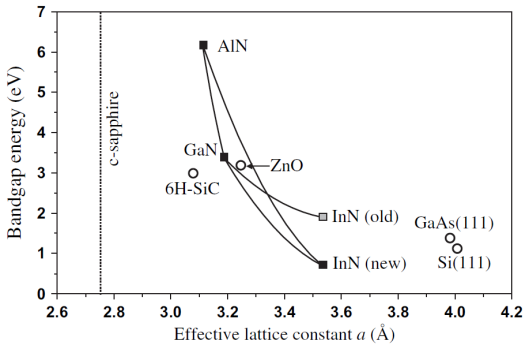

Figure 2.8: The energy band gaps and the lattice parameter of the (Al,Ga,In)N system. The band gap of InGaN is dependent on the quality of the deposited films. Low quality InN shows an absorption edge at roughly 2 eV (old), while an improved quality of the deposited material reduces the absorption edge to the value of the band gap down to 0.7 eV (new). Wang and Yoshikawa (2004)

explained by the Burstein-Moss shift (Wu and Walukiewicz (2003)), which is caused by the degeneration of semiconductor material by degeneration by a high free charge carrier concentration (Burstein (1954), Moss (1954)). In order to produce high quality InN specimens, have their absorption edge at the actual optical transition energy (0.7 eV), it is either possible to perform post-growth annealing (5h 490°C) in vacuum (Davydov et al. (2002)) or to grow the specimen using the plasma-assisted MBE (PAMBE) technique (Wu et al. (2002)).

Usually metal-organic chemical vapor epitaxy (MOVPE) is used for the growth epitaxial of GaN-structures (Wang and Yoshikawa (2004)). After growing a thin AlN buffer layer on a sapphire (α-Al_2O_3), which serves to reduce the stresses between substrate and layer, GaN epitaxially grown on top of it (Yoshida et al. (1983)). This buffer layer reduces the inherent stresses of the interface by introducing regularly arranged mismatch dislocations into its interface with the sapphire substrate (Sun et al. (1994)).

On the basis of such heteroepitaxially grown structures, additional layers which contain other group III elements can be deposited. Such double heterostructures have already been well established for use as light emitting devices (LED) and are able to cover a large range of wavelengths (Nakamura et al. (1993), Chen et al. (2021)).

Most crystal growth methods result in the incorporation of light element impurities (C, O), whose defects give way to n-type conductivity of epitaxially grown III-nitrides (Watson (2013)). For obtaining the free charge carrier concentrations required for the creation of devices such as LEDs, intentional doping is used. For n-type doping Si serves as a substitutional dopant on the Ga site, resulting in a shallow donor state with an energy of 12 to 17 meV below the conduction band (Ambacher (1998)). This low binding energy allows to consider that the doping induced free electron concentration in the conduction band is given by the doping concentration of Si. GaN based LED structures typically contain Si concentrations of $5 \cdot 10^{18}$ cm^{-3} (Watson (2013)).

Alternatively Ge can be utilized as an n-type dopant. This choice has been shown to provide good doping properties up to a charge carrier concentration of $2.4 \cdot 10^{20}$ cm^{-3} for MOVPE grown specimens (Kirste et al. (2013)) and $6.7 \cdot 10^{20}$ cm^{-3} for samples produced by PAMBE (Ajay et al. (2016)). In Kirste et al. (2013) it has been shown, that MOVPE grown GaN shows a proportionallity between the flux of the Ge-precursor (GaH_4) during the layer growth and the resulting free charge carrier concentration for charge carrier concentrations of up to $2.4 \cdot 10^{20}$ cm^{-3}. Ge-doped GaN specimen produced utilizing the PAMBE technique allows for even higher free charge carrier concentrations ($6.7 \cdot 10^{20}$ cm^{-3}, Ajay et al. (2016)). A direct comparison of the state of the art GaN growth techniques also shows that Ge-doping allows to reach high doping levels (above 10^{20} cm^{-3}), which are inaccessible by Si doping (Konczewicz et al. (2022)). Substitutional Ge doping of GaN also introduces less strain into the lattice when compared to Si doping (Bogusławski and Bernholc (1997)).

As shown in the comprehensive historical review on the development of blue nitride-based LEDs presented in Akasaki (2007), p-type doping of GaN (Amano et al. (1990)) was only achieved after the AlN buffer layer, which is required for the growth of high quality expitaxial GaN, has already been well established. The usual p-type dopant of GaN is Mg. By treatment of MOVPE grown Mg-doped GaN via low-energy electron beam irradiation (LEEBI), lowered resistivity and increased blue luminescence was achived (Amano et al. (1989)).

Since a LEEBI treatment of p-type GaN embedded in MOVPE grown structures is limited by the low penetration depth of its low-energy electron beam, the possibilities for the growth of heterostructures is limited. An alternative route for the growth of high-quality p-type GaN layers, which are sandwiched between other layers is MBE. It has been shown, that high growth temperature (≈ 1000°C) MBE using a high ammonia partial pressure for providing nitrogen into the films is viable for the production of GaN layers (Grandjean et al. (2001)).

By utilizing plasma-assisted MBE (PAMBE) high quality GaN/AlGaN heterostuctures can be grown at lower temperatures ($\approx 700°C$). The high charge carrier mobilities and good optical quality of structures grown utlizing this method made it a viable choice for the production of electronic devices' (Skierbiszewski et al. (2014)) based on GaN heterostructures. Also InGaN can be produced without introducing a large amount of free charge carriers utilizing PAMBE allowing to achieve a non-degenerate semiconductor, that also shows an absorption edge close to the actual band gap (Davydov et al. (2002)).

Recently the hydrogen-free PAMBE technique has been shown to allow for the production of p-type GaN layers embedded inside of GaN based heterostructures, which do not require any further treatment in order to activate the specimen's Mg-doping (Turski et al. (2019)). In this previously mentioned study three different tunnel junction (TJ) based heterostructures were investigated. While all these structures are grown along the polar axis of the hexagonal axis of wurzite GaN-heterostructures, the polarity of the growth direction is relevant for the microscopic electric field conditions present in the specimen. At the heterostructure interfaces large charge carrier concentrations accumulate. The accumulated charge carriers form a two-dimensional electron gas on the interface. The electric polarity of the field induced by these carriers is dependent on the system's growth direction (Fichtenbaum et al. (2007)). All semiconductor specimen discussed in the context of this thesis are grown along the [0 0 0 1]-direction (Ga-polar).

In Turski et al. (2019) two GaN-based light-emitting diodes (LED) produced by PAMBE are investigated (Fig. 2.9a and b). In both heterostructures the TJ serves to inject charge carriers into the (In,Ga)N quantum well, which is the optically active region, where the charge carriers are supposed to be generated in order to obtain a well defined luminescence signal, which is given by the optical properties of the QW. The primary difference between these two heterostructures is that the doping order is inverted for these two structures. This inversion of the structure's doping order allows a structure grown along the [0 0 0 1] to mimic the electronic structure of a diode grown along the $[0\,0\,0\,\bar{1}]$-direction. Due to this inversion of the system's electronic structure they show qualitatively different electroluminescence spectra despite the similar doping levels of these two structures' equivalent layers.

While the top-TJ LED (Fig. 2.9a) shows a strong contribution of the low In-content (7% In) cladding region which surrounds the QW (high energy emission in Fig. 2.10a), the bottom-TJ LED (Fig. 2.9b) only shows the electroluminescence signal originating from the QW itself (QW related emssion in Fig. 2.10a and b). This behavior is explained by the polarity of the bottom-TJ LED, which leads to a joint accumulation of electrons and holes which is limited to the QW itself, while the top-TJ LED configuration allows free

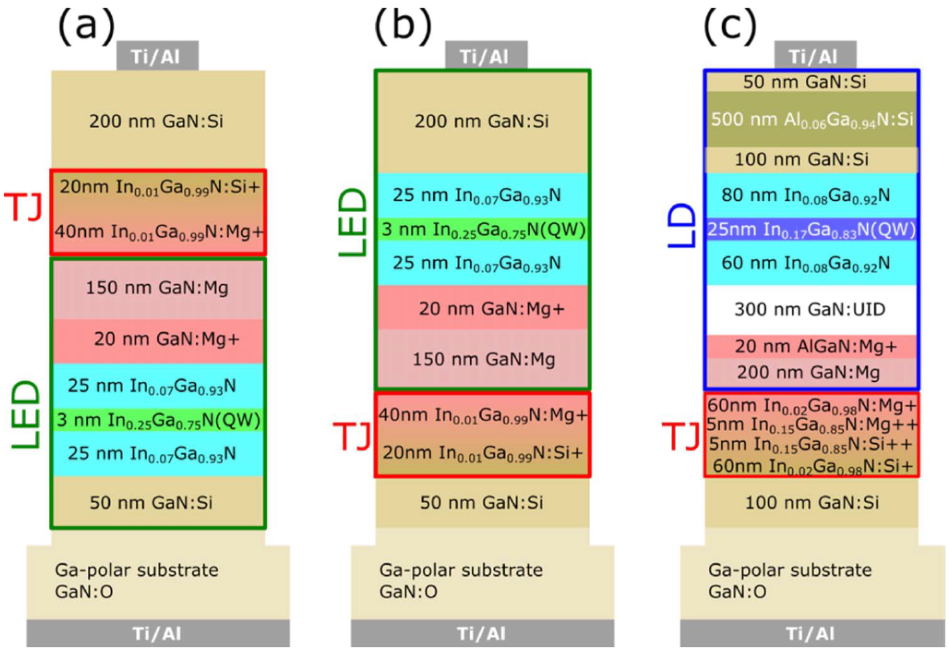

Figure 2.9: The GaN-based diode heterostructures studied in Turski et al. (2019). a) top-TJ LED (Ga-polar), b) bottom-TJ LED (N-polar), c) bottom-TJ LD (N-polar).

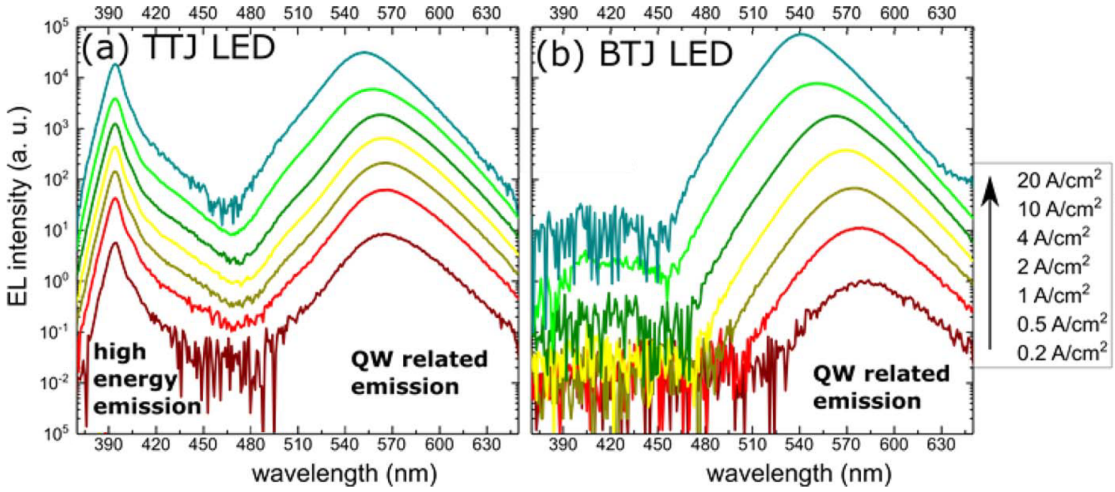

Figure 2.10: Electroluminescence spectra of the GaN-based LED shown in Fig. 2.9a and b presented as a function of the current density present in the LED device (Turski et al. (2019)). While the top-TJ LED shows an electroluminescence signal coming from the QW and its cladding layer (a), the bottom-TJ LED only shows the QW related emission (b).

carrier recombination in the low In-content cladding region. This statement is verified by numerical simulations of both structure's band gap diagrams, which confirm that electrons and holes coexist in the cladding region as well as in the QW for the top-TJ LED sturucture, while the bottom-TJ LED structure only shows the QW itself to contain a significant concentration of both electrons and holes. Since the spatial overlap of free electrons and holes is required for the emission of electroluminescence from a given region of the specimen, it is evident, that electroluminescence emission can be expected from both the cladding layers and the QW for the top-TJ LED structure, while the bottom-TJ LED only shows a signal originating from the QW exclusively.

Fig. 2.9c) shows the structural scheme of a bottom-TJ laser diode (LD), which was grown by PAMBE. In order to decrease the high operating voltage (≈ 8 V) of the bottom-TJ LED structure, the doping levels of the grown TJ is increased from a dopant density of $5 \cdot 10^{19}$ cm^{-3} ((In,Ga)N:X+) to 10^{20} cm^{-3} ((In,Ga)N:X++) (X=Mg,Si) for the LD structure.

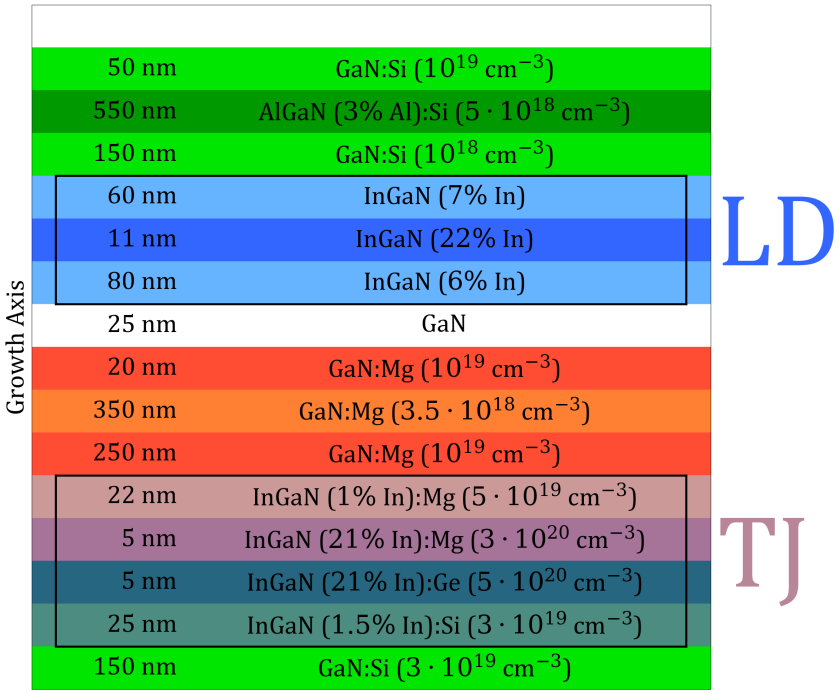

Figure 2.11: The bottom-TJ LD's layer structure, which is being studied using the photonic atom probe. The Ga site fraction of the alloying elements (Al, In) is shown in % and the doping (Mg, Si, Ge) levels are shown in cm^{-3}.

Using the PAP, a specimen akin to the bottom-TJ laser diode was studied in the scope of this thesis. As shown in Fig. 2.11, the general structure of the bottom-TJ LD (Fig. 2.9c)) is also present in this specimen. The entire structure is grown on a commercially available Ga-polar GaN substrate (with [0 0 0 1] as growth direction), on which the bottom layer GaN:Si ($3 \cdot 10^{19}$ cm^{-3}) is deposited. This n-type conductive layer serves as a basis on which the Tunnel Junction is deposited. The TJ itself consists of the highly doped and highly In alloyed central region and the cladding layers. The chemical information about the layers shown in Fig. 2.11 are obtained via XRD measurements for the alloying content (In, Al) and are estimated from the growth conditions of the dopant elements (Mg, Si, Ge). The bottom-most layer of the TJ is the low concentration and moderately doped InGaN (1.5 % In):Si ($3 \cdot 10^{19}$ cm^{-3})-cladding layer. Together with the p-doped top cladding layer (InGaN (1 % In):Mg ($5 \cdot 10^{19}$ cm^{-3}), this layer embeds the TJ. Due to the smaller band gap of InN (compared to GaN), the In content of both layers results in a lowered band gap in the TJ's surroundings. This causes a confinement of charge carriers in this region.

The TJ itself consists of two highly doped, high In-content InGaN layers. The n-type doped region (InGaN (21 % In):Ge ($5 \cdot 10^{20}$ cm^{-3})) of the TJ uses (opposed to all other n-doped regions of the specimen) Ge as dopant instead of Si. This choice of Ge as a dopant was made in order to ensure the presence of a high concentration of free electrons, which is necessary to create the electronic structure characteristic for the TJ (Konczewicz et al. (2022)). The highly p-doped layer of the TJ has the composition InGaN (21 % In):Mg ($3 \cdot 10^{20}$ cm^{-3}).

On top of the TJ GaN:Mg of varying Mg-doping levels is grown. This doping was introduced in order to ensure a good flow of electrical current into the optically active LD layer. Since the Mg-dopants also represent an unwanted channel for charge carrier recombination, a compromise between the conductivity of the p-doped layers and the Mg-induced optical losses has to be made. Three differently doped Mg-doped layers are involved in the region between TJ and LD. Two thick doping layers contain GaN:Mg (10^{19} cm^{-3}) and GaN:Mg ($3 \cdot 10^{18}$ cm^{-3}) are covered with a thin Mg-doped layer (GaN:Mg (10^{19} cm^{-3})). The LD region is separated from this p-type region by a thin unintentionally doped GaN layer.

The laser diode itself is surrounded by two cladding layers (InGaN (6% In) and InGaN (7% In)), which serve to concentrate the voltage induced free electrons and holes in the central layer of the LD (InGaN (22% In)). This central layer serves as the optical medium of the LD into which the charge carriers are pumped electrically. The reversed arrangement when compared with the classical top-TJ diode set-up (Fig. 2.9a), allows for

a more concentrated combined presence at the central layer, that reduces the intensity of the photo-emission generated from the TJ's cladding layers (Turski et al. (2019)).

Above the active LD layers, the doping is again n-type. The doping agent used here is Si. This region of the specimen also contains an Al alloyed layer (AlGaN (3% Al):Si ($5 \cdot 10^{18}$ cm^{-3})). This low refractive index material serves to push the optical modes into the lower layers of the specimen.

The PAP technique opens a new avenue for the study of GaN LD heterostructures. Firstly the chemical composition of the specimen shown in Fig. 2.11 can be analysed by the evaluation of the PAP obtained APT data. Since the specimen contains a multitude of different alloying (Ga, Al, In) and doping (Mg, Si, Ge) elements, an APT experiment offers a possibility for the quantification of the content of each component in every layer of the heterostructure.

Secondly the PL data obtained during the PAP experiment promises to provide insight into the specimen's optical properties in ways which are inaccessible for electroluminescence experiments. While electroluminescence only provides an optical signal from the optically active regions of the LD device, the PL signal collected in the context of the PAP experiment allows the collection of the optical response of a much larger region of the specimen.

Finally the combined analysis of compositional and optical properties obtained by the PAP experiment allows to identify the optical response of the different layers present in the heterostructure. By the subsequent field evaporation of the layers constituting the LD the evaporated layers can be excluded to contribute to the measured PL signal. By considering that a layer cannot contribute to a measured PL spectrum after it has been field evaporated, its characteristic PL response can be identified by exclusion.

2.2 The Photonic Atom Probe

2.2.1 Physical Background

The Laser-assisted Atom Probe Tomography (La-APT) technique uses an ultrashort (usually fs) laser pulse to trigger the field evaporation of surface atoms and to trigger the clock which is used to measure the time-of-flight of the field evaporated ion (thus giving information on the ion's mass-to-charge ratio). In semiconductor materials, this laser pulse can interact with the specimen in two different ways.

If the fs-pulse has a photon energy smaller than the band-gap, the specimen is not expected to have a strongly absorbing response to the excitation. This comes from

the quantum mechanically forbidden zone of the band-gap, which does not allow the existance of any states, which electrons are able to transition into with the supplied photo-energy. In such a scenario, no photocarriers can be considered to be generated due to single photo absorption in bulk material. However during the field evaporation of a specimen excitation is still possible when using sub band-gap energy laser pulses (Kelly et al. (2014b)). The specimen's excitation by below band-gap energy photons can be explained by multiple different approaches, which take into account the modification of the system's properties due to the high electric field present at the specimen's apex, or due to the high laser intensity which is present in the context of the La-APT experiment:

- Charge carrier accumulation and band gap shrinkage modify the opto-electronic properties close to the tip apex, resulting in an accumulation of large amounts of charge carriers close to the apex and a shrinkage of the material's band-gap (Silaeva et al. (2014))
- Higher harmonics generation due to local optical field enhancement leads to the generation of higher energy photons within the specimen (Bouhelier et al. (2003))
- The broken translational symetry at the tip surface leads to a rectification of the laser induced optical field, resulting in an electric field, which has an oscillation period that is much longer than the period of the exciting laser pulse. While the laser pulse oscillates too quickly to cause surface ions to be excited by it, the rectified electric field oscillates at a much lower frequency. It can be understood to serve as a DC electric electrical field which asists the evaporation of the specimen's surface ions during the excitation of the specimen via the laser pulse (Vella et al. (2006).

On the other hand a specimen with a band-gap which is lower than the laser-pulse's photon energy is generally able to directly generate photocarriers. The process of the excitation of bulk-like charge carriers via the laser pulse is shown in Fig. 2.12. First the absorption of a laser-photon creates a free hole and a free electron (1), then both free charge carriers thermalize (2), on the conduction and valence band respectively until they are fully thermalized. On the top of the valence band (for holes) and on the bottom of the conduction band (for electrons) they finally recombine (3) leading to the emission of PL photons.

During the thermalization of the specimen's charge carriers (2), electronic energy is transformed into vibrational energy carried by the specimen's lattice. This can be understood as the formation of phonons from the photocarriers' excess energy. This

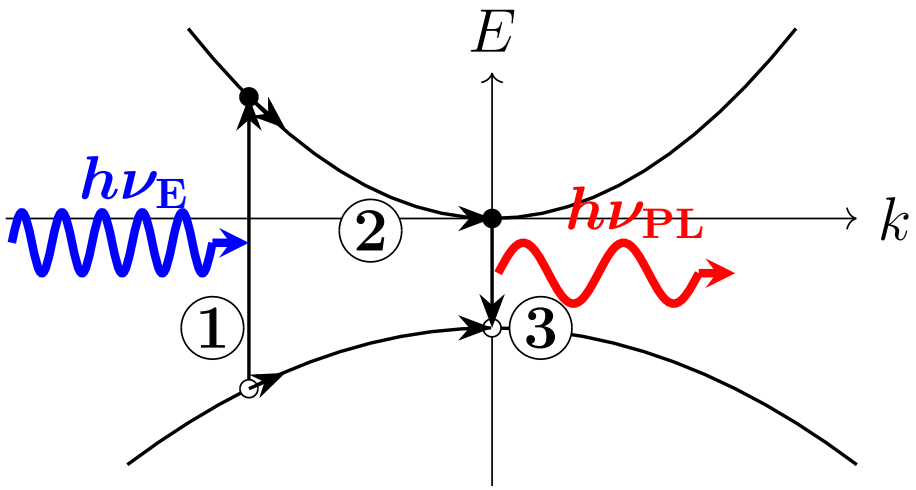

Figure 2.12: The generation of a Photoluminescence signal. (1) an exciting photon is absorbed by the specimen, generating an electron-hole pair. (2) intraband relaxation of both the free electron (conduction band) and the free hole (valence band). (3) recombination of the electron and hole at the extrema of their respective bands. The difference between the exciting energy $h\nu_{\mathrm{E}}$ and the PL energy $h\nu_{\mathrm{PL}}$ is the thermal photo-energy supplied to the specimen.

thermal excitation of the specimen's lattice increases the probabillity of the surface atoms' field evaporation (Vurpillot et al. (2006)).

While this thermal excitation of the lattice (2) is necessary for the La-APT method, the Photoluminescence (PL) emission which originates from the recombination of the photocarriers (3) can be considered as a necessary by-product of any La-APT measurement performed on a semiconductor material (if a laser with higher photon energy than the band gap is used). The PL signal contains optical information about the specimen (e.g. an approximation of the band-gap energy). This optical information can be harvested from an APT specimen by using the PAP technique.

2.2.2 Technical Realisation

The instrumental basis of the PAP as presented in Houard et al. (2020) is introduced in this section. Fig. 2.13a shows a schematic of the PAP set up. The laser pulse, which excites both the PL and the specimen's field evaporation is generated by a Ti:Sa oscillator (Coherent Chameleon Ultra II marked as 1.in the figure). This oscillator has an adjustable wavelength in the range from 600 to 1100 nm at a base repetition rate of 80 MHz and a pulse length of 150 fs. Set to a wavelength of 780 nm, it shows a peak

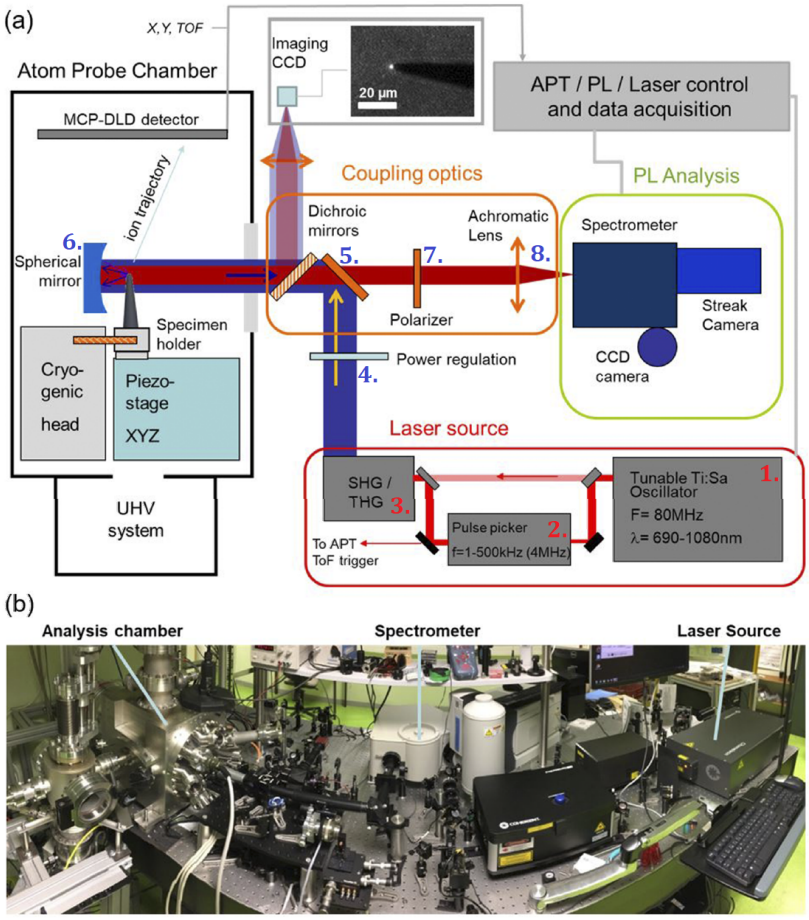

Figure 2.13: The Photonic Atom Probe. a) Schematic of the Elements constituting it. b) Photograph of the actual set-up. (Houard et al. (2020))

power of 4 W (50 nJ/pulse or 310 GeV/pulse).

Since the laser repetition rate is too high for an APT analysis, a pulse picker (2.) is used in order to reduce the pulse repetition rate. For atom probe experiments, the flight length of 18.5 cm limits the repetition rate. In order to be able to observe heavy ions, laser repetition rates below 500 kHz are recommended. At an acceleration voltage of 4 kV, $f = 500$ kHz corresponds to a critical mass to charge ratio (Eq. (1.14)) of $\left(\frac{em}{q}\right)_{\text{crit}} = 90$ amu, which represents the field evaporated ions with the highest mass-to-charge ratio which can still be properly assigned to the laser pulse which triggered its field evaporation. In order to perform a pure PL experiment and during the laser alignment process repetition rates up to 4 MHz are beneficial in order to ensure an increased PL intensity emitted from the specimen.

The laser pulses generated from the Ti:Sa oscillator serves as an inital beam from which higher harmonics are generated in order to excite the specimen using photon energies which are higher than what the oscillator can provide. An APE HarmoniXX third harmonics generator (THG) (**3.**) is used in order to generate the initial beam's second and third harmonics, allowing access to the wavelength ranges from 300 to 550 nm (second haromonic) and 200 to 367 nm (third harmonic) as well. Opposed to the set-up shown in Fig. 2.13a, in the layout of the set-up of the PAP during the performance of the PAP experiments, the clock which is used for the APT time-of-flight measurement is triggered by the THG pulse (270 nm) and not by the oscillator-generated fundamental beam (780 nm).

By using a $\lambda/2$ plate and a polarizer (**4.**), a fine-tuned power regulation as well as a laser polarization selection are performed. The laser intensity of the undesired lower harmonics (fundamental excitation and second harmonics) are filtered out utilizing a band pass filter. Usually the third harmonics (THG) pulse is used in order to excite the specimen ($\lambda = 270$ nm). The polarizer itself is arranged in such a way, that the passing pulse has an electric field, which is π-polarized. This means, that the electric field of the exciting laser pulse oscillates along the main axis of the APT tip.

The THG pulse is then guided into the PAP's optical axis. The optical axis serves a two-fold purpose for the PAP. Firstly it guides the π-polarized THG beam onto the studied specimen. Secondly it is also used to guide the specimen's optical response towards the PL spectrometer.

The dichroic mirrors (**5.**) guide the laser pulse towards the spherical mirror (**6.**), which serves to focus it onto the specimen. The spherical mirror also serves to collect the PL emitted from the specimen and guides it through the dichroic mirrors (**5.**) and towards the polarizer (**7.**). The dichroic mirrors reflect the laser pulse, while allowing the specimen's PL response to pass. This can be achieved by utilizing a high-pass energy filter, whose cut-off lies between the expected PL response's and the pulsed laser's energies.

The dichroic mirrors have to be selected in a way, that they mostly reflect the laser pulse, while being transparent to the specimen's PL response. The polarizer (**7.**) can easily be removed or inserted into the set-up in order to be have the choice between either the performance of polarization resolved PL analysis or to harvest the entire PL signal for low exposure time experiments.

By focussing the specimen's PL signal using an achromatic lens (**8.**), the PL is guided into the PL spectrometer. The used spectrometer is a Horiba iHR 320, which has three different gratings with line densities of 150 1/mm, 600 1/mm and 1200 1/mm, allowing

for energy resolutions of up to 0.5 meV. Alternatively the streak camera set up can be used in order to perform time-resolved PL measurements with a time resolution of 25 ps.

The APT detection set up utilizes a 77 mm diameter Multi-Channel Plate Delay Line Detector (Da Costa et al. (2004)), which is mounted at a 18.5 cm distance from the specimen apex position.

Since the Photonic Atom Probe is an analysis method, which combines Atom Probe Tomography and Photoluminescence Spectroscopy, it is important to call into mind, that some instrumental parameters play a conceptual role in both methods. This is important in order to clarify, what is meant when adressing said parameter. One of these instrumental parameters, which has a different meaning to the APT and μPL portions of the PAP is the field of view (Fig. 2.14). For the APT method the field of view describes the portion of the specimen, from where atoms can be detected by the MCP detector. For the $\mu-$PL set-up on the other hand, the field of view describes the solid angle around the specimen, from where PL signal is guided into the PL spectrometer. An estimation

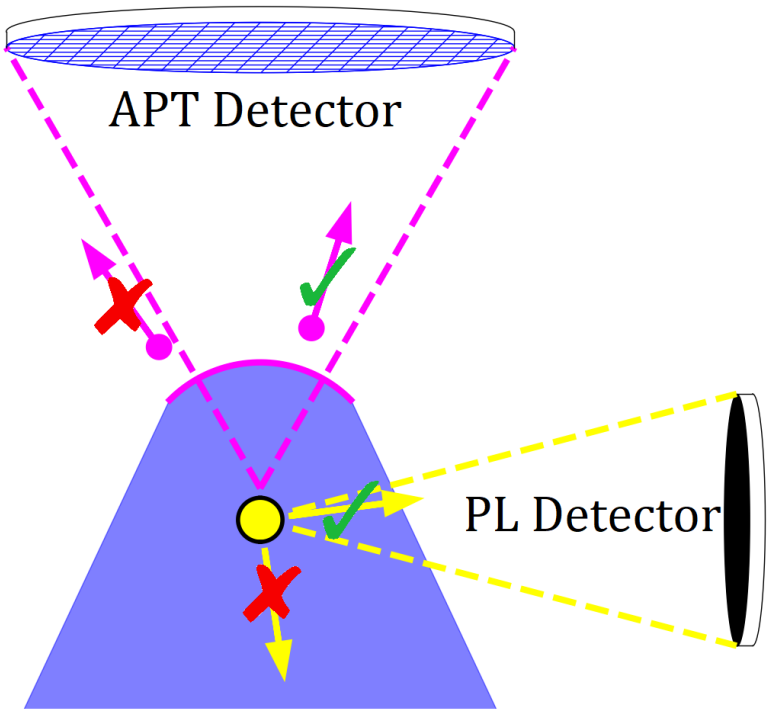

Figure 2.14: The field of views of the PAP. Since the instrument collects photonic (yellow) and atom probe (magenta) data, it is important to distinguish between both methods' distinct fields of view. Only those particles (ions and photons respectively) that are emitted into the respective field of view are detected by the set up.

of the PL spectrometer's field of view is delivered in Section 2.3.6.

2.3 Finite Difference Time Domain Calculations

The PAP measurement not only delivers information about the energy of the PL signals emitted from the different emission sources of the specimen, it also allows the user to extract physical information from the total amount of PL intensity, which is being emitted from the sample. However the PAP's PL set-up is only able to detect the strength of the PL response which is being emitted into its field of view. Since the vast majority of the emitted light is not directed into the system's field of view, the total strength of the emitted PL signals remains unknown. In order to properly interpret the physical meaning of the PL-intensity which is being detected by the PAP set-up, a series of simulations was performed. The purpose of these simulations is to measure the dependence of the detected PL signal on the development of the APT-tip's geometry during its field evaporation. FDTD simulations were used to theoretically describe the PL emission from a ZnO QW embedded inside of (Mg,Zn)O material (Section 2.1.1).

By simulating the propagation of the laser excitation as well as of the QW's emitted PL response, the strength of the detected PL signal is being estimated. The light propagation was simulated using the FDTD (Section 2.3.1) solver of the Lumerical software package. Two sets of simulations were performed in order to study the tips laser-absorption and PL-emission behavior.

The tip geometry can be expected to have a relevant impact on the strength of both the excitation caused by the laser and the distribution of the emitted PL intensity. Both the absorption and emission simulations were performed for a set of specimen geometries, which represent the different geometries the tip takes during its laser-assisted field evaporation (Section 2.3.2, Fig. 2.15a). The optical properties of the material which fills this geometry are described in Section 2.3.3. Since the specimen preparation and the extreme field conditions of the APT specimen can also be expected to modulate the optical properties of the specimen, they are the focus of the considerations of the aforementioned section.

The simulations of the laser-absorption behavior (Section 2.3.4, Fig. 2.15b) serve as a way to estimate the total amount of photo-carriers which are being generated inside of the QW. Without taking into account any carrier-transport-effects, these simulations provide us with a measure of the total PL-emission strength emitted by the QW.

The evolution of the tip geometry during its field evaporation not only changes the amount of light absorbed by the QW, but also how much of the emitted PL intensity

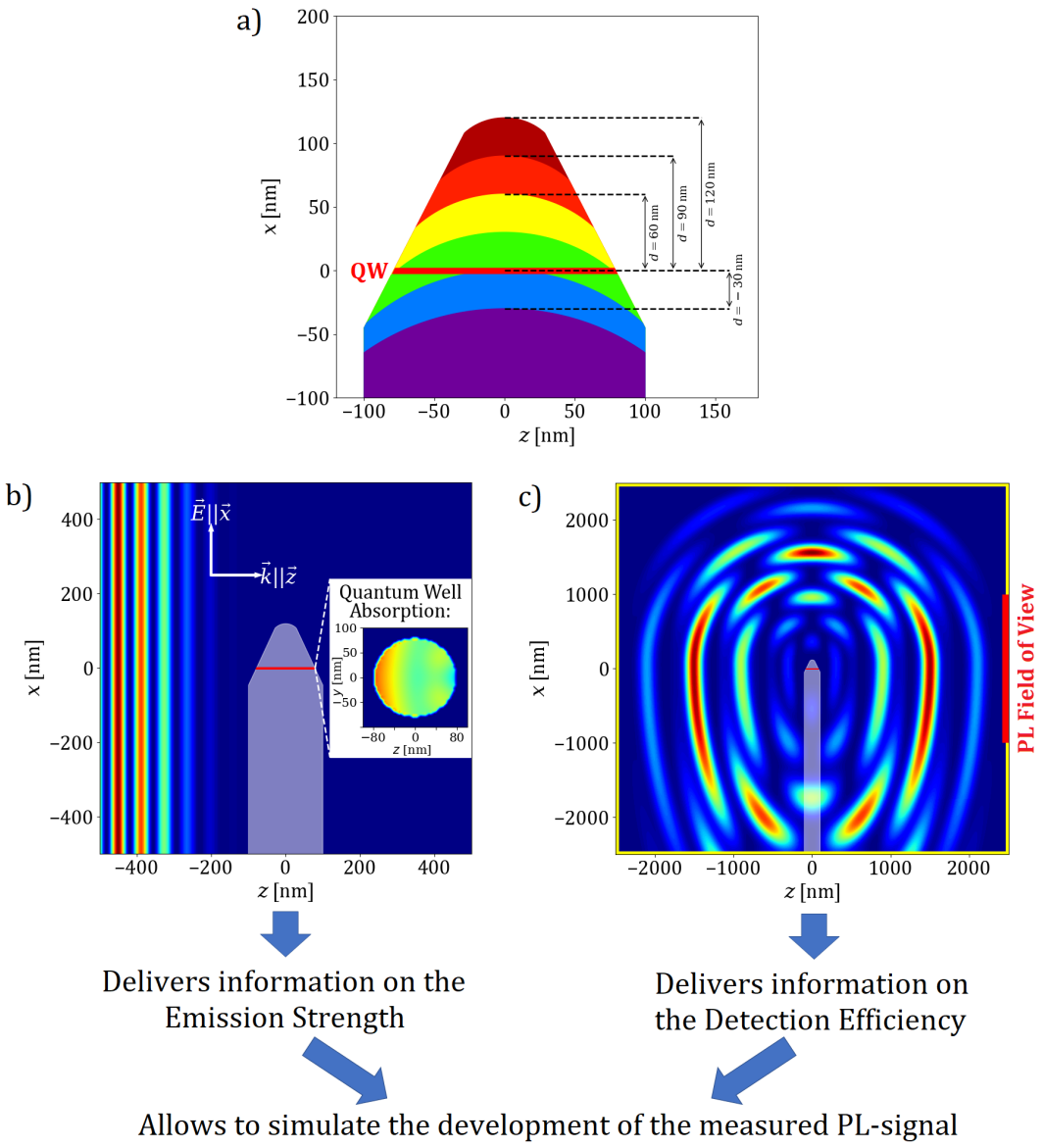

Figure 2.15: Schematic of the FDTD simulation's work flow. a) The FDTD simulations are performed on different evaporation stages of the specimen as a function of the depth of analysis d relative to the QW (red line). b) For each idealized tip geometry the amount of laser-light absorbed at the QW is simulated. The intensity of the emitted PL from the QW is considered to be proportional to laser-absorption in the QW-plane (see inlet). c) Also the far field emission of the QW generated PL is simulated. From this information, the fraction of light, which is being caught inside of the PL-spectrometer's field of view (yield) is obtained. By combining b) and c), the development of the measured PL signal is being simulated.

propagates into the PL-spectrometer's field of view. Since only a small fraction of the space surrounding the specimen is covered by the field of view of the PL detection set up, most of the emitted PL is unavailable for the detection system. Since the geometry of the specimen undergoes modifications during the PAP experiment, the fraction of the PL which is caught by the detection set-up changes during the tip evaporation. PL-emission simulations (Section 2.3.5, Fig. 2.15c) are performed in order to calculate the fraction of emitted PL intenstiy which is directed into the PL-detection system's field of view (Section 2.3.6). By combining the information on the fraction of light, which is being caught inside of the PL-detection system's field of view, with the total amount of light emitted from the QW, the PL detection efficiency (or yield) is calculated as a function of the progress of the specimen's field evaporation.

By combining the results of both sets of simulations, the development of the measured PL-signal can be simulated and can be compared to the experimentally measured PL signal (Section 2.3.7).

Finally a methodology for FDTD simulations of polarization resolved PAP experiments is presented in Section 2.3.8. The evaluation of the FDTD simulation data presented here allows to simulate PAP experiments in the context of which the Polarizer (described in Section 2.2.2) is inserted into the set-up.

2.3.1 The Finite-Difference Time-Domain (FDTD) Method

The Finite-Difference-Time Domaine (FDTD) method developed by Yee (1966), is a Computational Electro-Magnetics (CEM) method. As such it simulates the interaction of electromagnetic fields with matter, by solving Maxwell's equations numerically.

The FDTD method uses Maxwell's curl ($\vec{\nabla}\times$) equations as its foundation. Utilizing these it simulates the propagation of light through a medium with the permittivity ϵ and the permeability μ:

$$\begin{aligned} &\frac{\mathrm{d}\vec{B}}{\mathrm{d}t} + \vec{\nabla} \times \vec{E} = \vec{0} \\ &\frac{\mathrm{d}\vec{D}}{\mathrm{d}t} - \vec{\nabla} \times \vec{H} = \vec{j} \\ &\vec{B} = \mu\vec{H} \\ &\vec{D} = \epsilon\vec{E} \end{aligned} \tag{2.1}$$

In the following the general mechanism of the FDTD method is presented using a minimal example which is not related to the previously presented geometric problem.

In order to exemplify how this method works, let's consider the one-dimensional propagation of linearly polarized plane wave ($E_y = E_z = H_x = H_z = 0, \frac{\mathrm{d}H_y}{\mathrm{d}x} = \frac{\mathrm{d}E_x}{\mathrm{d}y} = 0, \vec{k} = k_0 \cdot \vec{e_z}$) in vacuum ($\vec{j} = \vec{0}, \mu = \mu_0, \epsilon = \epsilon_0$). Under these conditions Eq. (2.1) can be reformulated to:

$$\begin{aligned} \frac{\mathrm{d}H_y}{\mathrm{d}t} &= -\frac{1}{\mu_0}\frac{\mathrm{d}E_x}{\mathrm{d}x} \\ \frac{\mathrm{d}E_x}{\mathrm{d}t} &= -\frac{1}{\epsilon_0}\frac{\mathrm{d}H_x}{\mathrm{d}x} \end{aligned} \tag{2.2}$$

In order to obtain a numerical solution of Eq. (2.2), a grid in space and time ($z = i' \cdot \Delta z, t = n' \cdot \Delta t$) is defined, where i' and n' take the values of half-integer values $\left(i', n' = 0, \frac{1}{2}, 1, \frac{3}{2}, 2, \frac{5}{2}\right)$. Utilizing the defined grid, the values which any time and space-dependent property can be expressed as a function of i' and n' instead ($F(i', n')$). Estimating both the time and spatial derivative by the central difference approximation yields:

$$\begin{aligned} \frac{E_x(i, n+\frac{1}{2}) - E_x(i, n-\frac{1}{2})}{\Delta t} &= -\frac{1}{\epsilon_0} \cdot \frac{H_y(i+\frac{1}{2}, n) - H_y(i-\frac{1}{2}, n)}{\Delta z} \\ \frac{H_y(i+\frac{1}{2}, n+1) - H_y(i+\frac{1}{2}, n)}{\Delta t} &= -\frac{1}{\mu_0} \cdot \frac{E_x(i+1, n+\frac{1}{2}) - E_x(i, n+\frac{1}{2})}{\Delta z} \end{aligned} \tag{2.3}$$

Eq. (2.3) shows some major attributes of the FDTD method. By considering the values of i and n to be integer values ($i, n = 0, 1, 2, 4, ...$) the electric E_x and magnetic H_y fields can be calculated in alternating spatial and temporal points of the grid. We see that only integer values of i' and half-integer values of the temporal index n' are required to calculate every expression of the electric field E_x which is required in order to solve Eq. (2.3). The values of the magnetic field H_y on the other hand are only required for half-numbered values of i' and integer values of n'.

This implies that the electric field E_x only needs to be calculated for every second space and time grid point, while the magnetic field H_y has to be calculated for every other grid point in space and time. This can be considered as an interleaving of the electric and magnetic field in both space and time. By alternately calculating the electric and magnetic field after every half time step Eq. (2.3) can be treated. This calculation only has to be performed for alternating grid point positions for either field (Fig. 2.16).

The electric field at the position i at the time step $n+\frac{1}{2}$ ($E_x(i, n+\frac{1}{2})$) can be calculated by utilizing the electric field, which was calculated for the previous electric field time step $(n - \frac{1}{2})$ $E_x(i, n-\frac{1}{2})$ and by calculating $\frac{\mathrm{d}H_y}{\mathrm{d}z}$ from the two calculated surrounding

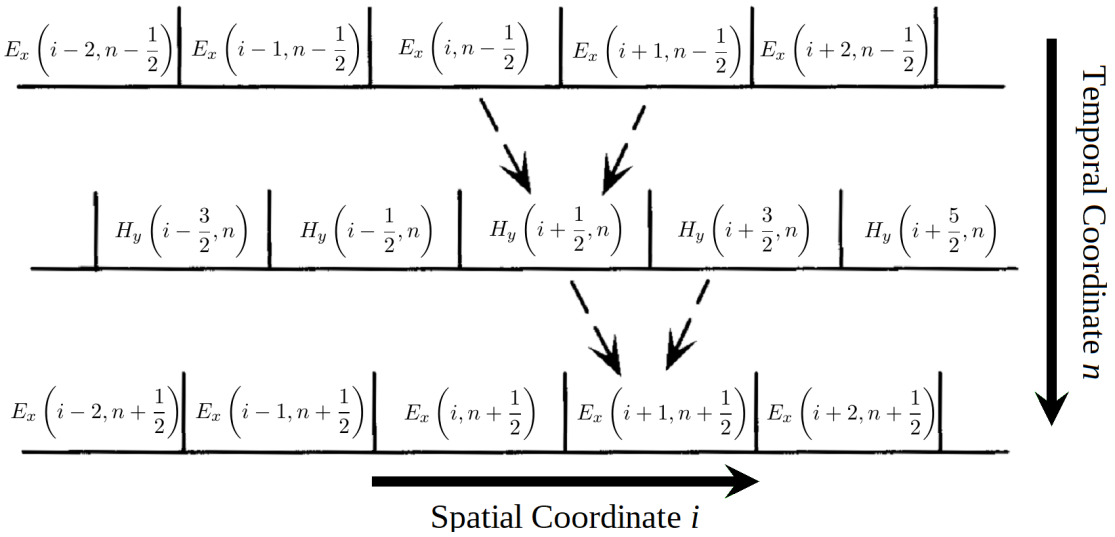

Figure 2.16: Interleaving of the electric and magnetic field in space and time. For the FDTD simulation the electric and magnetic field are calculated alternately for each half time step (Δt). From the spatial perspective, the positions of the electric and magnetic field grid can be considered to be interleaved spatially (Sullivan (2000)).

magnetic field values which were calculated at the previous time step (n) $H_y(i-\frac{1}{2},n)$ and $H_y(i+\frac{1}{2},n)$. The magnetic field for the next time step $(n+1)$ $(H_y=(i+\frac{1}{2},n+1))$ can be calculated utilizing the same procedure.

The method explained here can be transfered from one into three spatial dimensions, resulting in a multitude of different space points from which the electric and magnetic field components are being obtained for each spatial simulation cell (Fig. 2.17). In three dimensions the usage of interleaving spatial and temporal grid points allows to satisfy perfectly conductive boundary conditions (Yee (1966)), at the edges of the simulated space. These boundary conditions describe edges of the simulation space which act like perfectly absorbing material nullify any incident power. This allows to study power flows, which can be understood to leave the simulated space.

A benefit of this method is that its calculations are performed in time domain. This means that electromagnetic pulses of finite pulse duration and their interaction with matter can be easily simulated. This is possible since the FDTD method requires the usage of broad-band sources, which also allows to study the interaction of different selected wavelengths with the specimen from only a single simulation run.

The solutions of the Maxwell equations Eq. (2.1) obtained by FDTD give the electric $(\vec{E}(\vec{x},t))$ and magnetic $(\vec{H}(\vec{x},t))$ field at every other point of the spatial grid $\vec{x}$ and for

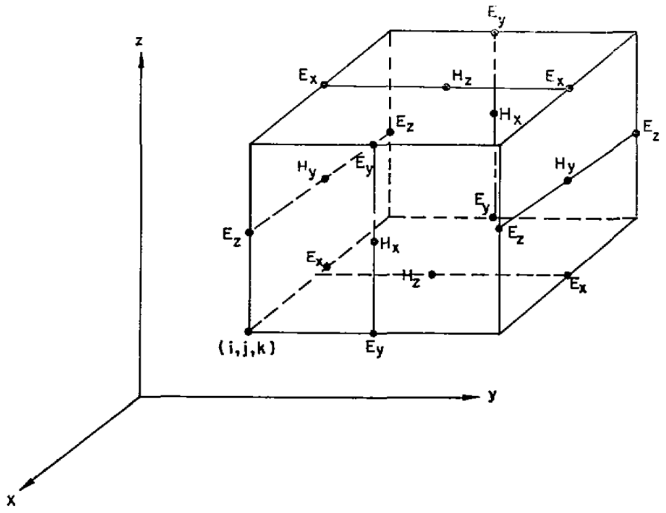

Figure 2.17: Example of a simulation cell of the three-dimensional FDTD simulation space. The different components of both the electric and magnetic field are all calculated at different positions inside of the unit cell itself (Yee (1966)).

every other simulated time t. Since the sources used in the simulation have a broad-band nature in frequency domain, a specimen's response to a specifically chosen frequency ω requires a Fourier Transform of the simulation results. By only investigating the Fourier component of $\vec{E}(\vec{x},t)$ and $\vec{H}(\vec{x},t)$, which has the frequency ω the specimen's response to a monochromatic excitation with frequency ω can be investigated.

2.3.2 Geometric Evolution and depth of analysis

The geometry on which the FDTD simulations are performed is based on an idealized geometry of the specimen which is investigated in the context of the PAP experiment (Fig. 2.18). The focus of these simulations is the behavior of a single PL emitting quantum well (QW), which represents the PL emitting QW#1 (Section 2.1.1). The absorption behavior of this nanostructure is studied by calculating the electric field induced by the laser pulse (which is induced by a plane wave source in the simulation) present in the QW. The distribution of the PL emission is calculated in a separate simulation in which a dipole-antenna emission source is placed inside of the center of the QW. These simulations are performed for a single geometry first, but since the specimen develops its shape during the APT experiment, they are performed for a set of different geometries. In this section the idealized shapes of the specimen, on which the FDTD simulations are performed are explained.

The successive removal of surface atoms during a specimen's field evaporation corresponds to continuous evolution of the tip geometry during the performance of an APT experiment. Since the specimen is of a size, which is similar to both the exciting laser pulse's wavelength and the PL response's wavelength, a small modulation of the specimen's geometry (on the nanometric scale) can cause a large change of the absorption and emission behavior.

In order to take the effect of the developing tip geometry into account for the FDTD simulations a series of tip geometries is defined. These were used in order to perform both absorption and emission simulations. This set of tip geometries represents the geometric evolution of an atom probe specimen evaporating during an APT experiment. By performing FDTD simulations at different stages of the specimen's geometric development, the measured PL-signal intensity can be simulated for different tip geometries between the onset of the specimen's field evaporation and its end. The progression of the evaporation front is described by the depth-of-analysis d (see Fig. 2.15a). For the (Mg,Zn)O system (Section 2.1.1) d describes the distance between the current tip's apex and the QW, which can be found embedded inside the specimen.

A high value of d corresponds to an early evaporation state, while a value of $d \to 0$ indicates that the evaporation front closes in on the QW. $d = 0$ finally indicates, that the QW has been completely evaporated. $d < 0$ indicates, that the evaporation front has already penetrated beyond the QW in depth. For the (In,Ga)N system (Section 2.1.2) $d = 0$ describes the final evaporation state, before the end of the experiment, while higher values of d describe earlier evaporation stages of the specimen.

For the FDTD simulations an idealized geometry of an APT specimen was defined. The main purpose of this idealized geometry is that it should be easily modifiable, so that the different evaporation stages, which the APT specimen undergoes during its geometrical development can be easily represented in the simulation space. Also it is convenient to keep the number of parameters, which describe the idealized specimen minimal, in order to avoid a redunantly complex description of the specimen. The specimen geometry is introduced into the simulation space as solid of revolution. This is possible since the tip shaped has a rotational symetry around the tip main (x) axis. The specimen itself is described as the solid of revolution which originates from revolving the silhouette function ($\tilde{s}(r)$) around the $x-$axis.

Fig. 2.18 shows a shematic of the generalized tip geometry. The parameters describing the specimen geometry are the top radius of curvature (r_0), the top radius (r_t), the taper angle (τ), the depth of analysis (d) and the top sphere segment height (δt).

Since the specimen is rotationally symetrical around the x-axis, it can be completely

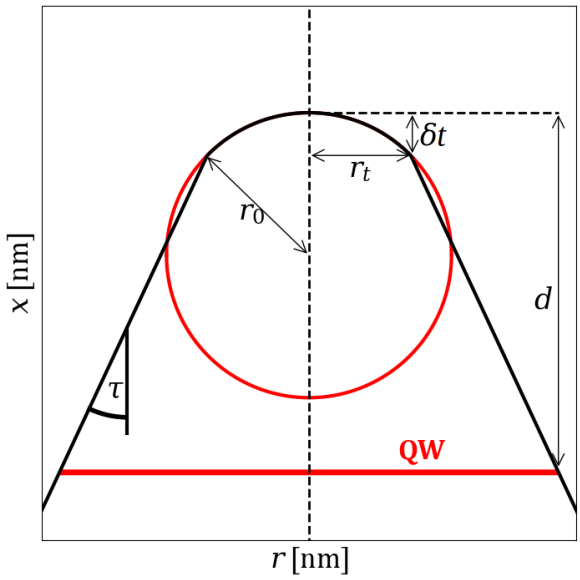

Figure 2.18: Schematic geometry of the idealized tip shape.

described by its silhouette $\tilde{s}(r)$ along the r-axis ($r = \sqrt{y^2 + z^2}$). The main quantity used to describe the specimens field evaporation is the apex radius of curvature r_0. This radius of curvature (r_0) and the cone-top-radius (r_t) are considered to be proportional to each other (with $\beta = 1.4$):

$$r_0 = \beta \cdot r_t \tag{2.4}$$

This relationship describes a discontinuity of the silhouette's slope, where the top sphere segment touches the linear backbone of the specimen.

The third quantity, which characterizes the tip's geometry is the taper angle (τ). Since the depth of analysis (d) is the means by which the evaporation progress is measured, a relation between the radius of curvature and the depth of analysis needs to be formulated. The height of the top sphere segment (δt) can be estimated using simple trigonometry:

$$r_0^2 = r_t^2 + (r_0 - \delta t)^2 \Rightarrow \delta t = r_0 \cdot \left(1 - \sqrt{1 - 1/\beta^2}\right) \tag{2.5}$$

For $r \geq r_t$, the silhouette ($\tilde{s}(r)$) can be defined by its slope (given by the taper angle τ):

$$\frac{\mathrm{d}\tilde{s}(r)}{\mathrm{d}r} = -\cot(\tau) \Rightarrow \tilde{s}(r) = -\cot(\tau) \cdot r + K_1, \text{ for: } r \geq r_t \tag{2.6}$$

The silhouette is also defined, so that the position of the QW corresponds to $x = 0$. The cone-top-radius can thus be associated with the depth of analysis, giving us the unknown constant K_1:

$$\tilde{s}(r = r_t) = d - \delta t = -\cot(\tau) \cdot r_t + K_1 \Rightarrow K_1 = d - \delta t + r_t \cdot \cot(\tau) \tag{2.7}$$

For $r \leq r_t$, the silhouette is defined as a circle's segment. This circle is centered around $x_0 = d - r_0$ and has the radius r_0. Thus the silhouette can be defined for all values of r:

$$\tilde{s}(r) = \begin{cases} -\cot(\tau) \cdot (r - r_t) + d - \delta t & \text{for: } r \geq r_t \\ r_0 \cdot \sqrt{1 - \dfrac{r^2}{r_0^2}} + d - r_0 & \text{for: } r \leq r_t \end{cases} \tag{2.8}$$

The tip geometry described in Eq. (2.8) is defined inside of the Lumerical software's FDTD solver. In this geometry, there is a direct connection between the radius of curvature r_0 and the depth of analysis (d) as well.

The progressing field evaporation leads to a reduction of the simulated geometry's depth of analysis d as well as an increase of its radius of curvature r_0. Consider two geometric states of the specimen at the same radial coordinate, which itself corresponds to a x-coordinate at a large distance from the evaporation front ($r > r_t$). Since the interesting radial coordinate is far away from the evaporation front for both evaporation states, its corresponding x-coordinate will also be the same:

$$\begin{aligned} &\tilde{s}(r, d = d_1, r_0 = r_1) = \tilde{s}(r, d = d_2, r_0 = r_2) \\ &-\cot(\tau) \cdot (r - r_1/\beta) + d_1 - \delta t(r_1) = -\cot(\tau) \cdot (r - r_2/\beta) + d_2 - \delta t(r_2) \\ &d_2 - d_1 = (r_2 - r_1) \left(1 - \sqrt{1 - 1/\beta^2} - \frac{\cot(\tau)}{\beta}\right) \end{aligned} \tag{2.9}$$

By considering the difference between r_1 and r_2 (and thus also d_1 and d_2) to be incremental the differential relation between r_0 and d can be expressed as:

$$\frac{\Delta d}{\Delta r_0} = 1 - \sqrt{1 - 1/\beta^2} - \frac{\cot(\tau)}{\beta} \tag{2.10}$$

With the tip original radius of curvature r_0' and the original depth of analysis d_0 known,

the radius of curvature of a later stage of field evaporation r_0 can be expressed as a function of the depth of analysis:

$$r_0 = \frac{\Delta r_0}{\Delta d} \cdot (d - d_0) + r_0' = \left(1 - \sqrt{1 - 1/\beta^2} - \frac{\cot(\tau)}{\beta}\right)^{-1} \cdot (d - d_0) + r_0' \qquad (2.11)$$

Using Eq. (2.11) r_0 and r_t can be eliminated from Eq. (2.8), allowing to characterize the tip's geometry only by the depth of analysis d.

In the context of the FDTD simulations of the ZnO/(Mg,Zn)O, the parameters defining the geometry of the specimen change with the tip's progressing field evaporation. The depth of analysis starts at a value of $d = 120$ nm and goes against $d = 0$ nm once the QW is getting close to be fully field evaporated. The radii of curvature start at $r_0 = 40$ nm for early evaporation states and reach $r_0 = 140$ nm for the later evaporation states of the specimen. Both the taper angle $\tau = 25°$ and the ratio between the radius of curvature and the top radius $\beta = 1.4$ are considered to be static values and do not change during the simulation of the progressing field evaporation of the specimen.

The tip defined in this section serves as a subject for the following FDTD investigations. In order to simulate the dependence of the detected PL-signal on the tip's geometric evolution during its field evaporation, the development of the generated amount of charge carriers as well as the development of the detection efficiency need to be studied. In the following sections, the tip laser-Absorption behavior (Section 2.3.4), as well as the distribution of its PL emission (Section 2.3.5) is being studied for different tip geometries. These geometries serve to describe the evolution of the field evaporating APT-tip.

2.3.3 Dielectric Function and Optical modulations

With the silhouette of the specimen well defined, the dielectric function of the material filling it needs to be defined. The fashion of how the dielectric properties of the analysed specimen is characterized is presented in depth in Weikum et al. (2023). The text and the illustrations of this section is the same as the text presented in the section "2.C.4. Modulation of the Optical Properties" of this previously published work.

A specimen, which is mounted in an APT set-up can be expected to show modified optical properties, when compared with bulk material. These modulated optical properties are caused by the preparation route via focused-ion-beam (FIB) milling or by the high electric field, which is being applied to the specimen in APT. While the FIB milling can be expected to cause the specimen's initial surface to be amorphized (Vella et al. (2018) Bogdanowicz et al. (2018)), the high electric fields, which penetrate the APT-specimen

can be expected to drastically change the electronic properties of the material, which is close to the tip apex Silaeva et al. (2014). The results of the optically modulated tip's properties are being compared to the case of unmodulated properties (Non-Degenerate Surface Section 2.3.3.1).

When the APT analysis starts, the sample has an amorphous surface of about ten nanometers due to the FIB milling. After the field-evaporation of the amorphous surface layer, the analysed surface is crystalline and the static electric field, which is surrounding the sample, penetrates inside the sample on a few tens of nanometers. This huge electric field creates a high density of free carriers (holes) at the surface and induces a drastic reduction of the band-gap of the material. These two effects are combined and happen at the same time but they will be described separately in the following.

The Non-Degenerate Surface simulation assumes the tip's surface and apex to have the same optical properties as bulk material, which represents the disregard of any surface amorphization or field-related optical modulation effects. The simulations of the optically modified specimen (Amorphized Tip's Surface, Free Hole Apex, Perfectly Reflective Apex) also consider the specimen to have the same optical properties as introduced into the Non-Degenerate Surface simulation, with the exception of the regions, which are considered to be optically modulated (Fig. 2.19). The real (η) and imaginary (κ) part of the refractive index, which is used to simulate the optical properties of the respective regions is shown in Table 2.1.

Table 2.1: The different simulated materials' complex refractive index ($n = \eta + i\kappa$) and absorption coefficient (α). The excitation wavelength (270 nm) describes the absorption, while the response (365 nm) describes the specimen's emission properties.

λ	270 nm			365 nm		
$n = \eta + i\kappa$	η	κ	$\alpha[\mu\mathrm{m}^{-1}]$	η	κ	$\alpha[\mu\mathrm{m}^{-1}]$
ZnO	1.89	0.52	24.2	2.41	0.56	19.3
(Mg,Zn)O	1.97	0.53	24.7	2.12	0.07	2.4
Amorphized Tip's Surface	2.00	0.28	13.0	2.00	0.02	0.7
Free Hole Apex	1.85	0.62	28.9	1.91	0.20	6.9
Perfectly Reflective Apex	1.00	10^5	$5 \cdot 10^{\,6}$	1.00	10^5	$3 \cdot 10^{\,6}$

2.3.3.1 Non-Degenerate Surface

In order to obtain the dielectric function of (Mg,Zn)O the optical constants of ZnO (Fig. 2.1,Yoshikawa and Adachi (1997)) were shifted by the difference between the PL energy of (Mg,Zn)O and ZnO (0.55 eV) (Fig. 2.5, Dalapati et al. (2021)). For the purpose of the treatment of the light's propagation by the FDTD solver, both QW#1 and QW#2 are considered to have the same dielectric function as bulk ZnO. The most significant difference in the optical behavior of ZnO and (Mg,Zn)O, is that the (Mg,Zn)O phase shows a much lower imaginary part of the refractive index for the wavelength of the PL emission (365 nm). This implies, that the PL emitted from the QW can pass through the surrounding (Mg,Zn)O-phase without any major absorption losses.

2.3.3.2 Amorphized Tip's Surface

In order to simulate the effect of the amorphized surface (Fig. 2.19-(a)) on the tip specimen, the absorption coefficient of amorphous ZnO was estimated first. By utilizing transmission spectroscopy data of amorphous thin film ZnO samples Zawadzka et al. (2014), the absorption coefficient can be estimated. The interference fringes below the absorption edge suggest the real part of the refractive index η to take values of roughly 2 (Zawadzka et al. (2014)). By assuming that the above band gap loss in transmittance mostly stems from light absorption (the reflectivity is assumed not to significantly change when compared to below band gap reflectivity), the absorption coefficient of ZnO can easily be estimated for different wavelengths. By blue-shifting the values obtained for the refractive index of ZnO by 0.55 eV, the refractive index of amorphous (Mg,Zn)O is estimated. This rough approximation allows to obtain the values for κ and thus for the absorption coefficient (α).

The amorphization is FIB-preparation induced and the progressing field evaporation of the tip creates an amorphous surface. By removing portions of the FIB-amorphized surface for a progressing evaporation front within the FDTD-calculations, its development during the specimen's field evaporation is taken into account (Fig. 2.19-(b)).

Here and for the following models, we chose modified layers with thickness of 12 nm. The choice is motivated by the fact that the adaptive mesh of our emission simulations takes values of roughly 6 nm close to the QW1. However, this value is also close the typical amorphization depth due to Ga ions and to the over which free charges build up Silaeva et al. (2014).

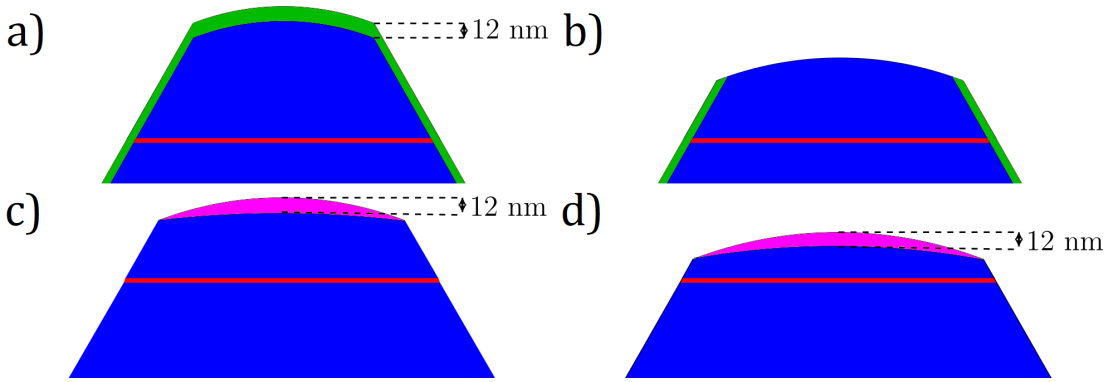

Figure 2.19: The amorphized surface (shown in green) of the simulated geometry before any evaporation takes place ($d = 120$ nm) and b) after some of the specimen has been evaporated. The amorphized surface is being evaporated during the tip's evaporation as well. It is assumed, that the FIB-beam amorphizes the specimen surface up to a depth of 12 nm. c) The electrostatically modified apex (shown in magenta) of the simulated geometry in an early evaporation and d) a later evaporation stage. The electric field is assumed to penetrate up to a depth of 12 nm. The electrostatically modified zone is considered move along together with the progressing evaporation front.

2.3.3.3 Free Hole Apex

To describe the modulation of the specimen's optical properties by electric field effects, the optical properties of the tip apex are being modified for the performed FDTD simulations (Fig. 2.19-(c)). Since the electric field penetrates the tip apex for every evaporation stage, the region of the modulated optical properties does not shrink during the tip's field evaporation, but instead moves together with the increasing depth of analysis (Fig. 2.19-(d)).

Considering that the free holes induced by the electric field accumulate close to the specimen apex, their effect on the specimen optical properties can be described as a modulation of the (Mg,Zn)O barrier material's dielectric function:

$$\epsilon_{\mathrm{Apex}}(\omega) = \epsilon_{\mathrm{MgZnO}}(\omega) - \frac{1}{\omega^2 + i\omega/\tau} \cdot \frac{e^2 p}{\epsilon_0 \epsilon_r m} \tag{2.12}$$

where τ is the electron motion's damping time, p is the hole concentration, $\epsilon_r = 8.5$ is the electric permittivity of the material and m is the holes' effective mass. By defining the optical properties of a region close to the specimen apex (Fig. 2.19-(c,d)) with the free carrier model (Eq. (2.12)) in Lumerical's FDTD solver, we were able to study the effect of such modified surface properties on the absorption and emission behavior. In

simulation space, the modified region has a thickness of up to 12 nm at the tip's center and becomes thinner close to the edges of the spherical portion of the tip. By considering this region to be present for every simulated tip geometry, the carrier accumulation close to the apex is taken into consideration for the FDTD-simulations. For the effective mass of holes in (Mg,Zn)O, the value for ZnO was taken ($m = 0.59\ m_0$) Reynolds et al. (1996), the carrier damping time $\tau = \frac{\mu \cdot m}{e} = 3.4 \cdot 10^{-16}$ s was estimated from a hole mobility of $\mu = 1\ \frac{\mathrm{cm}^2}{\mathrm{V \cdot s}}$ Ozgur et al. (2005). For the hole concentration p a value of $5 \cdot 10^{22}\ \mathrm{cm}^{-3}$ was chosen, which is one order of magnitude higher than reported in Silaeva et al. (2014). Eq. (2.12) shows that the modulation of the dielectric function is proportional to the density of the free charge carriers. If the over-estimation of the charge carrier density doesn't cause any major changes in the absorption-weighted yield behavior, the effect of a more realistic (and thus lower) concentration of accumulated free charge carriers close to the tip apex on the specimen PL emission properties is not significant either.

2.3.3.4 Perfectly Reflective Apex

Since the holes, which accumulate close to the specimen apex, exist inside of a potential sink, additional resonances of the surface holes can be expected to arise. Also the high electric field close to the apex has been shown to lead to a drastic reduction of the band gap (Silaeva et al. (2014)). The Free Hole Model does not consider these additional resonances.

In order to account for the effects introducing stronger resonances at the apex surface, a hypothetical modulation of the optical properties of the tip apex was taken into consideration. By choosing a high value for the imaginary part of the refractive index $n = \eta + i\kappa$, a perfectly reflective top apex is introduced. The same geometry as for the Free Hole Apex has also been used for the simulation of this Perfectly Reflective Apex model (Fig. 2.19-(c) and Fig. 2.19-(d)). At the interface between vacuum ($n_v = 1$) and the Perfectly Reflective Apex ($n_P = 1 + 10^5 i$) the fraction of light, which is not being reflected ($1 - R$) amounts to $4 \cdot 10^{-10}$ at normal incidence:

$$R = \left| \frac{n_P - n_v}{n_P + n_v} \right|^2 = 1 - 4 \cdot 10^{-10} \approx 1 \tag{2.13}$$

Thus almost the entirety of the light hitting the Perfectly Reflective Apex is being reflected right at this interface. The optical properties of the Perfectly Reflective Apex serve to simulate a top layer, which is characterized by extremely strong resonances with both the exciting laser pulse and the emitted PL signal.

2.3.4 fs-Laser-Absorption and PL-Emission Intensity

In the context of the PAP, the fs-laser pulse both serves as a trigger for the field evaporation of surface ions and as a photoexcitation of the system's charge carriers. Since the absorption of the laser's radiation (270 nm), by the specimen represents an interband excitation for all phases present in the (Mg,Zn)O system, the relaxation of these excited charge carriers into the valence band causes the PL-emission. In the linear optical regime, the intensity of the PL, which is emitted from the specimen is proportional to the amount of the laser-generated photocarriers. Thus the laser intensity, which is being absorbed by the specimen can be considered to be proportional to the intensity of its PL response.

This paragraph describes the simulation basis and the procedure for the evaluation of the QW's fs-laser pulse absorption as a function of the specimen's field evaporation progress. By performing FDTD simulations, the QW's absorption strength is estimated. This is done by evaluating the value of the laser-induced electric and magnetic field inside of the QW for a set of tip geometries, which mimic the specimen's geometric development due to its field evaporation (Section 2.3.2).

A screenshot of how the simulation space is set-up inside of the Lumerical's FDTD solver is shown in Fig. 2.20. This set of simulations was performed in a simulation volume measuring $4.0\mu\text{m} \times 4.0\mu\text{m} \times 1.8\mu\text{m}$. The short side of this volume ($1.8\mu\text{m}$) is the z-axis, along which a light source injects its energy into the system. The light source itself has a center wavelength of 350 nm and a spectral width of 350 nm. While this simulated laser pulse does not describe the actual laser pulse's behavior in time domain, this configuration still gives a high intensity at the wavelength of the exciting laser pulse, which has a wavelength of 270 nm (4.6 eV). After a Fourier transformation of the simulated results (in time domain), the system's optical response to the desired wavelength is extracted. The benefit of simulating a source element, which has a larger spectral width than the actual source is, that its pulse length is reduced in time domaine, which reduces the required simulation time. The light source representing the laser, which was introduced into the simulated space is a plane wave propagating along the z-direction and is π-polarized, with respect to the tip's main axis ($\vec{E}||x$).

Inside of the simulation volume, a mesh volume of the size $1.5\mu\text{m} \times 1.5\mu\text{m} \times 1.5\mu\text{m}$ is defined. Both the simulation volume and the mesh volume are centered around the middle of the PL-emitting QW. Inside of this mesh volume, the detector space was set-up.

In Lumerical's FDTD solver, the monitor element serves as a way to define at which points of the spatial grid the simulated data are saved in order to be made available for post processing and data analysis. Two monitor of the same size were added into the

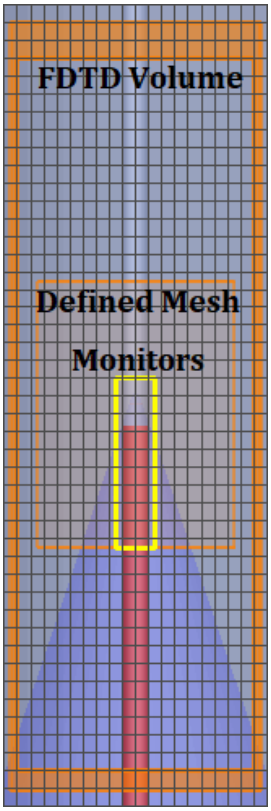

Figure 2.20: Screenshot of the simulation space of the FTDT simulation. The grey object which lays over the other objects is an etching mask.

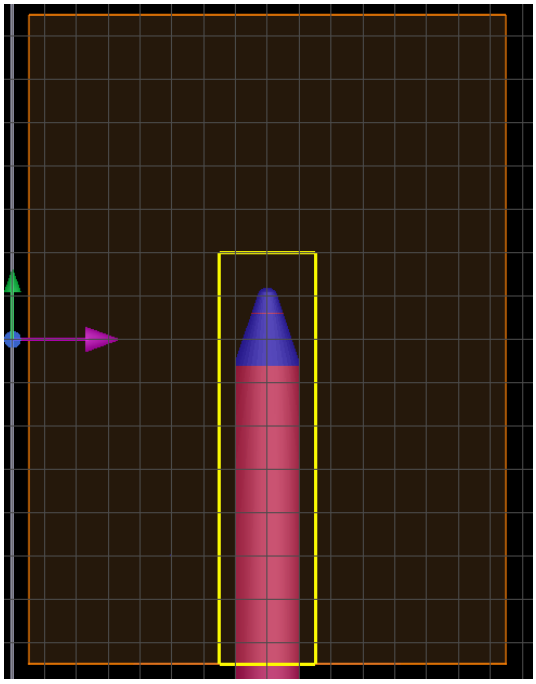

Figure 2.21: Edited screenshot of the simulation space. The etching mask is replaced by introducing its effect (the remove of all material overlapping with it) into the image.

mesh volume. An index monitor and a field monitor cover the same volume (950nm × 300nm × 300nm), which is set-up in the proximity of the QW. Their output contains the refractive index and the electric field strength, at any mesh points inside of the monitor volume, as well as the position of the individual mesh points in their shared volume.

Additionally a movie monitor was added into the simulation space. This monitor visualizes the value of the electric field as it is generated by the simulated pulse. The exported video file shows the development of the electric field as a function of the simulated pulse's propagation time.

Adaptive meshing was used in order to perform these simulations and the spacing of the meshpoints is of the order of 3 nm for every simulation and for the entirety of the monitor space.

The simulation takes into account the specimen's geometry and its dielectric proper-

ties as described in Section 2.3.2. A screenshot of the geometry, as it is implemented in Lumerical is shown in Fig. 2.20. While the screenshot does not give a clear description of the actually simulated geometry, it helps understanding how the geometry is implemented in the software. The grey haze, which lies above the specimen represents a hollow cylinder and covers parts of the cone-like specimen shape (see: Section 2.3.2). This hollow cylinder represents an etching mask in the context of Lumerical's FDTD solver. As such, it overrides the dielectric function of all the other material, which is covered by it with the dielectric function of vacuum. The hollow cylinder has an inner radius of 100 nm and straightforwardly, the material outside of its inner diameter is considered to be "etched" by the program giving it the frequency independent optical properties of vacuum ($n = 1, k = 0$). The result is a cone-like specimen, which is cut-off at a radius of 100 nm Fig. 2.21.

The monitor data obtained from the FDTD simulations allow access to the electric field vector $\vec{E}(\vec{r}_j)$ as well as the dielectric function $\epsilon\,(\vec{r_j})$ at any grid point's position $(\vec{r}_j)$ in the simulated space. From the spatially resolved electric field, the amount of absorbed power can be calculated at every Yee cell position $(\vec{r}_j)$:

$$P(\vec{r_j}) = \frac{1}{2}\omega \left|\vec{E}\,(\vec{r_j})\right|^2 \cdot \mathrm{Im}\,(\epsilon\,(\vec{r_j})) \tag{2.14}$$

This amount of absorbed power can be integrated over the area ($\mathrm{d}A$) of the QW's cross section in order to obtain a measure of the total amount of light, which is absorbed by the QW. Since the simulation space is discretized in the context of the FDTD simulation, this integral can be transformed into a sum. Due to the discretisation of space, there are no grid points at the center of the QW's plane. In order to gain access to the electric field vector $\vec{E}$ at the center of the QW, its values are being interpolated at regular grid positions $(\vec{r_j})$. These positions have a regular spacing of $\tilde{a} = 1.4$ nm. By inserting the interpolated electric field values into Eq. (2.14), the absorbed power at these interpolated positions can be calculated. By summing over all these interpolated grid positions, the total amount of energy absorbed by the QW can be obtained:

$$\tilde{A} = \int_{\mathrm{QW}} P\,(\vec{r})\,\mathrm{d}A \approx \sum_{j\in\mathrm{QW}} \frac{\tilde{a}^2}{2}\omega \left|\vec{E}(\vec{r_j})\right| \cdot \mathrm{Im}\left(\epsilon(\vec{r_j})\right) \tag{2.15}$$

By performing the above mentioned absorption simulation on the defined set of tip geometries, the development of the PL intensity emitted from the QW, as a function of the developing tip geometry is calculated. The absorbed power $\tilde{A}$ is calculated for every tip geometry i.

The maximum value of these absorbed laser-powers $\max\left(\tilde{A}(i)\right)$ is calculated. Dividing every geometry's absorbed power by the power absorbed by the geometry, which has shown the strongest absorption gives the relative absorbed power $A(i) = \frac{\tilde{A}(i)}{\max\left(\tilde{A}(i)\right)}$, which is calculated for every simulated geometry (i). By doing this, the relative development of the emitted PL power is calculated in order to estimate the development of the QW's PL emission strenght during the field evaporation of the specimen.

2.3.5 PL-Emission Distribution

The relaxation of the excited photocarriers causes the system's PL response. While the total strength of the PL emission is calculated according to Section 2.3.4, the development of the tip geometry is also expected to change the distribution of the emitted PL signal. This is important in the context of our analysis, because the PL detection system used in the PAP has a small field of view. With a small field of view, a minor change in the spatial distribution of the emitted energy can already suffice to significantly change the detected intensity.

The APT specimen analysed by the PAP has spatial dimensions in the order of the wavelength of the PL response (365 nm), and undergoes a removal of volume on similar lengthscales due to its field evaporation. Such a removal of matter close to the apex can be expected to also modify the distribution of the emitted PL-power, by modifying the propagation properties of the PL, which passes through the specimen and towards the detector.

Because the geometric evolution of the specimen influences the spatial distribution of the QW's far-field PL emission, the fraction of the emitted PL which is being caught by the PL-spectrometer's field of view is also dependent on the tip's evaporation progress. This fraction of the QW-emitted PL signal, which is being caught by the PL-detection system's field of view is refered to as the QW PL yield (f).

In order to obtain information on the development of the QW PL yield during the APT tip's field evaporation, a series of FDTD simulations was performed on the same set of tip geometries, on which the laser-absorption simulations were already performed in Section 2.3.4.

A screenshot of the simulation space within the FDTD solver of the Lumerical software package is shown in Fig. 2.23. The emission simulations are performed on a simulation volume of (5.2 μm×5.2 μm×5.2 μm), which is centered at the QW. In order to investigate the propagation behavior of the PL signal emitted by the specimen, an electric dipole antenna source is placed in the center of the QW. This dipole source emits

light in a wavelength range from 0.2 μm to 1 μm and gives a strong signal at the PL emission's experimentally obtained wavelength of 365 nm (3.4 eV).

The orientation of the dipole emission source is not as straightforward as was the polarization of the plane-wave, which was used to describe the laser pulse discussed in the previous section Section 2.3.4. While the exciting laser's has a polarisation which is well defined by the polarizer utilized for the power regulation (**4.** in Fig. 2.13 a)), the emitted PL is simulated utilizing a different source of the Lumerical software package, which is a dipole emitter instead of plane wave. Since the polarization of the emitted PL is generally unknown, multiple dipole emission sources with different orientations are used for the FDTD simulations.

In order to take this lack of information into consideration the FDTD simulations were performed on selected dipole orientations. A comparison of the simulation results obtained considering the differently oriented dipole orientations with the experimentally observed behavior allows an evaluation about what orientation best describes the experimentally observed behavior (Weikum et al. (2023)). Additional polarisation resolved PL-experiments in the context of the PAP instrumentation allow to gain additional insights concerning the specimen's PL emission behavior (Dalapati et al. (2022)) and is described in Section 2.3.8.

The simulated APT tip which is used for studying the far-field distribution of the PL signal, which is emitted from the QW is being investigated for emission along three different perpendicular axes. For each of these three different emission dipole orientations, a separate series of simulations is performed on the whole set of defined geometries. This allows to study the effect of the tip's field evaporation on the PL emission behavior of differently oriented dipoles. The three dipoles which were selected for the simulation of the specimens far-field PL distribution are oriented along three different perpendicular axes (Fig. 2.22):

- the tip's main axis (x)
- the optical axis (z)
- the y axis perpendicular to both of these ($\vec{e_y} = \vec{e_x} \times \vec{e_z}$)

Fig. 2.23 shows a x-oriented dipole source placed in the system's simulation space.

Inside of the previously mentioned FDTD volume (5.2 μm×5.2 μm×5.2 μm), a mesh stretching over a volume of (5.0 μm×5.0 μm×5.0 μm) was introduced. The mesh volume is (like the FDTD volume) centered at the QW.

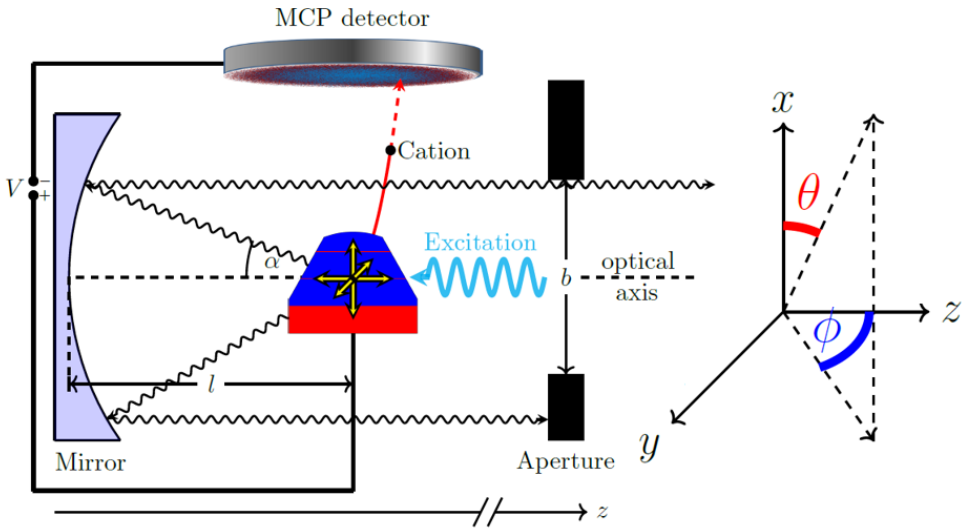

Figure 2.22: The PAP set up and the corresponding axes orientations. The tip's main axis (x) also describes the average trajectory of the emitted ions. The optical axis (z) is used to guide the exciting laser pulse to the sample and to collect the PL emission. The y-axis is perpendicular to both previously mentioned axes. (Weikum et al. (2023))

On the edges of this defined mesh, two-dimensional field monitors are placed. These record both the electric and magnetic field in order to quantify the energy flow through them. In order to calculate the outflux of PL intensity into every direction a total of six field monitors form a box around the PL-emitting QW. These detector elements fully encase the simulated specimen and thus allow obtaining electric and magnetic field at every mesh point on the edges of the mesh. By only recording the fields close to the edges of the simulation space (instead of the whole simulation space) the RAM required to perform the simulation is drastically reduced.

The simulation mesh ($\vec{\widetilde{x}_i} = (x_i, y_i, z_i)$), which was used for this set of simulations is an adaptive mesh (e.g. it is procedurally generated for every simulated geometry) and not a regular mesh. It gives a high spatial resolution to more geometrically delicate portions of the simulated specimen. Since the adaptive mesh is separately calculated for every tip's geometry, the grid points where the fields are being recorded are slightly different and thus the output from the electric and magnetic field monitors is not directly comparable for different simulated tip geometries.

In order to study the development of the specimen's far field PL emission during its field evaporation, a comparison of the PL signal emitted from the different geometries

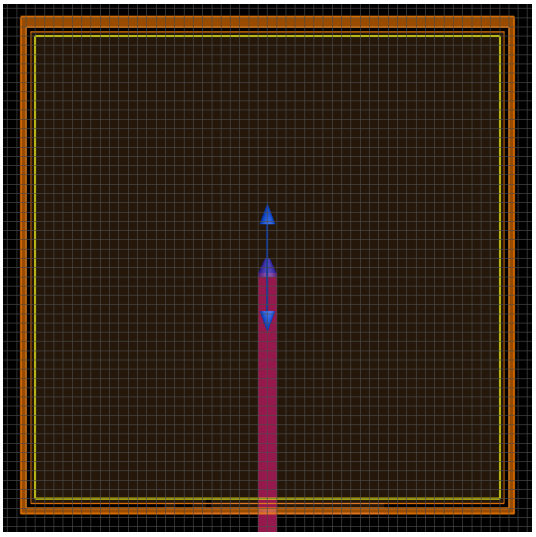

Figure 2.23: Edited screenshot of the defined space for the FDTD emission simulations. Like in Fig. 2.21, the etching mask was removed from the picture in order to obtain a better idea of the tip geometry.

representing the evaporation process is necessary. The dipole emission source which describes the QW originates at the origin of the cartesian coordinate system (0,0,0). All six field monitor planes have the same distance from this point. To allow a comparison of the PL signal emitted from the different tip geometries, an interpolation routine was used. For the study of the far field PL emission distribution, the grid generated for interpolation $\vec{\tilde{r}_i} = (r_i, \phi_i, \theta_i)$ is defined in spherical coordinates:

$$\begin{aligned} \theta_i &= \arccos\left(\frac{x_i}{|\vec{\tilde{x}_i}|}\right) \\ \phi_i &= \mathrm{sign}(y_i) \cdot \arccos\left(\frac{z_i}{\sqrt{y_i^2 + z_i^2}}\right) \\ r_i &= |\vec{\tilde{x}_i}| \end{aligned} \tag{2.16}$$

Utilizing Eq. (2.16), the cartesian coordinates $(\vec{\tilde{x}_i})$ of the detectors' grid points are transformed into the spherical coordinate system $(\vec{\tilde{r}_i})$. Since every single simulation was performed on a separate simulation grid, the detectors' coordinates $\vec{\tilde{x}_i}$ (and thus also $\vec{\tilde{r}_i}$) differ slightly between the different performed calculations.

An interpolation of the electric and magnetic field values at the original grid positions transformed to spherical coordinates characterized by i ($\vec{E}(\vec{\tilde{r}_i})$ and $\vec{H}(\vec{\tilde{r}_i})$) is performed

onto the regular grid in spherical coordinates characterized by j (providing $\vec{E}(\vec{\tilde{r}_j})$ and $\vec{H}(\vec{\tilde{r}_j})$). Since the transformed grid points $\vec{\tilde{r}_j}$ are the same for every simulated tip geometry, the knowledge of $\vec{E}(\vec{\tilde{r}_j})$ and $\vec{H}(\vec{\tilde{r}_j})$ allows to compare the power of the emitted PL into the direction $\vec{\tilde{r}_j}$ for different evaporation stages of the tip. This means that it is possible to directly compare the far field distribution of the emitted PL intensity.

These new grid's points ($\vec{r_j}$) are regular in ϕ and θ (with a spacing of 1°) and the plane which contains them has the same distance from the PL emitting QW as the original grid's ($\vec{\tilde{r}_i}$) detector planes. On the new grid $\vec{r_j}$ the electric and magnetic field values ($\vec{E}(\vec{\tilde{r}_j})$ and $\vec{H}(\vec{\tilde{r}_j})$) are interpolated from the field values at the positions of the spherically transformed monitor point positions ($\vec{\tilde{r}_i}$).

From the electric and magnetic field vector, which are recorded by these monitor elements, the outflux of power is measured by calculating the Poynting vector at the grid points ($\vec{r_j}$):

$$\vec{\tilde{P}}(\vec{r_j}) = \vec{E}(\vec{r_j}) \times \vec{H}^*(\vec{r_j}) \tag{2.17}$$

The norm of the Poynting vector's real part $|\mathrm{Re}(\vec{\tilde{P}})|$ describes the amount of power passing through a grid point, while its normalized vector $\frac{\mathrm{Re}(\vec{\tilde{P}})}{|\mathrm{Re}(\vec{\tilde{P}})|}$ describes the direction of the flow.

Consider a point source, which emits light into every direction. The energy, which flows to every sphere with radius r around the point source is the same. Thus density of the energy flux $I(r)$ through all these spheres is given by the total amount of emitted energy $\tilde{I}_o$ and the surface area of the sphere $4\pi r^2$:

$$I(r) = \frac{\tilde{I}_o}{4\pi r^2} \tag{2.18}$$

Since the detector elements in the FDTD solver are located at a high distance (2.5 μm distance from the emission source), compared to the emission's wavelength of 365 nm, the emitted signal is considered to show only far-field effects at the position of the detector elements. For the calculation of the spatial distribution of the emitted power, it has to be taken into consideration that different points of the planar detector elements have different distances from the source of the PL emission (the QW). This is performed by utilizing the relation Eq. (2.18) in order to transform the calculated Poynting vector

$\vec{\tilde{P}}(\vec{r_j})$ (Eq. (2.17)) into the normalized Poynting vector $\vec{P}(\theta, \phi)$:

$$\vec{P}(\theta,\phi) = \frac{\vec{\tilde{P}}(\vec{r_j})}{4\pi\vec{r_j}^2} = \frac{\vec{E}(\vec{r_j}) \times \vec{H}^*(\vec{r_j})}{4\pi\vec{r_j}^2} \tag{2.19}$$

This equation takes into account, that different regular grid points $\vec{r_j}$ have different distances from the simulated PL source. This has to be taken into consideration in order to represent the emitted power in a spherical coordiate system instead of the Cartesian coordinate system. After this transformation Eq. (2.19), the power of the simulated PL emission can be represented as a function of just the two angles (ϕ and θ) of the spherical coordinate system. This representation gives the spatial distribution of the far field emission power of the specimen's PL signal.

Each grid element ($\vec{r_j}$) in spherical coordinates represents a solid angle (Ω) increment. The corresponding Poynting vector gives the transmitted power ($\tilde{P}$) per solid angle increment of the grid $\frac{\tilde{P}}{\mathrm{d}\Omega}$. In the regular grid with spherical coordinates, the different grid points represent different solid angles, where each of these grid points with a given θ and ϕ represents a solid angle increment:

$$\mathrm{d}\Omega = \sin\theta \cdot \mathrm{d}\theta \cdot \mathrm{d}\phi \tag{2.20}$$

where $\mathrm{d}\theta$ and $\mathrm{d}\phi$ represent the grid spacing (1° in our case).

By evaluating Eq. (2.17), the flow of power $\tilde{P}$ from the PL-emitting QW through the detector the solid angle increment characterized by θ and ϕ is quantified:

$$\begin{aligned} \tilde{P}(\theta,\phi) &= \frac{1}{2}\mathrm{Re}\left(\vec{P}(\theta,\phi)\right) \cdot \frac{\vec{r_j}}{|\vec{r_j}|} \cdot \mathrm{d}\Omega \\ &= \frac{1}{2}\mathrm{Re}\left(\vec{P}(\theta,\phi)\right) \cdot \frac{\vec{r_j}}{|\vec{r_j}|} \cdot \sin\theta \cdot \mathrm{d}\theta\mathrm{d}\phi \end{aligned} \tag{2.21}$$

Eq. (2.21) allows to represent the emitted power as a function of the two spherical angles θ and ϕ. This representation allows to visualize the QW's far field PL emission in the form of a heat map where the emitted power $\tilde{P}$ is colorcoded against the two angles θ and ϕ. An example of such an emission map is shown in Fig. 2.24. The emission maps give direct information about the amount of energy, which is being emitted into different directions.

The most instrumentally relevant portion of emitted PL-radiation is the fraction of PL, which is being directed towards the hemispherical mirror. Since it is the only portion of the emitted PL radiation, which falls into the field of view of the PL-detection set-

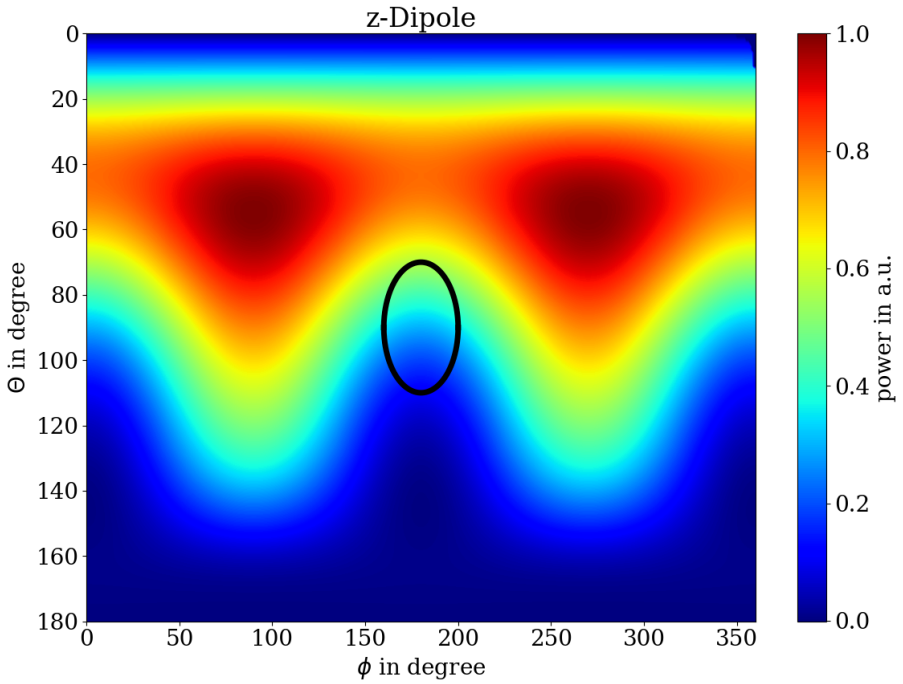

Figure 2.24: An example of an emission map. The emitted power is shown as a function of the direction of the emission (see Fig. 2.22). The black circle in the center of the emission map represents the PL detection system's field of view.

up, it is also the only radiation, that can be detected by the PL-spectrometer. In the emission maps, this portion of space is marked by a black circle in the center of the graph (see: Fig. 2.24). By integrating over the power $\tilde{P}$, which falls into the PL-spectrometer's field of view, the amount of detectable power (from a purely geometric standpoint) is estimated. The fraction of the total PL power, which is geometrically detectable is refered to as the emission yield. In the following section, a geometric estimation of the PAP's PL-detection set-up's field of view is presented.

2.3.6 The PL-spectrometer's Field of View

The PAP allows the user to analyse the PL which is emitted from a field emitter tip utilizing a spectrometer. Only a small portion of the emitted PL falls into the field of view of the detection set-up. A spherical mirror with a focal length l =2.5 cm (Fig. 2.25) is utilized in order to focalize the laser excitation on the specimen. The same spherical mirror is used to collect the specimen's PL emission and to guide it into the PL spectrometer, which lies on the optical axis (z-axis). Assuming that all optical beams are perfectly collimated after being reflected by the spherical mirror, the field of view of the

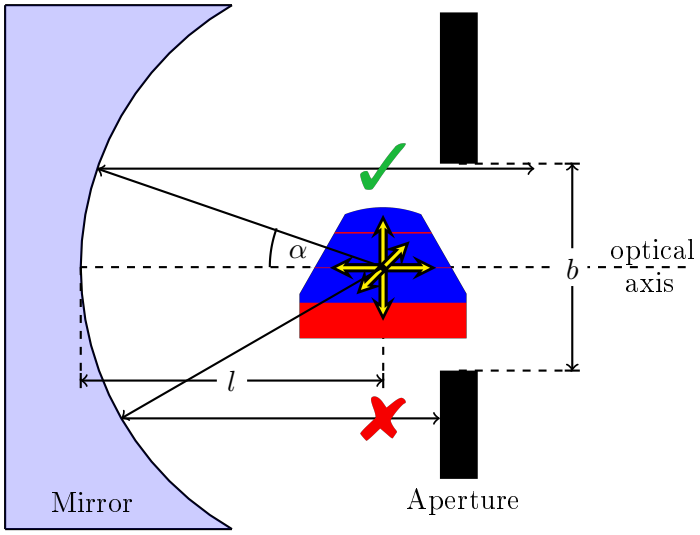

Figure 2.25: Geometry of the optical path. The periscope, which constitutes the smallest aperture of the set up is in fact much further away from the mirror than the atom probe tip is. Only those beams which have a lower emission angle α, than the critical angle α_c are able to pass through the aperture.

PL set up is given by the smallest aperture in the optical path between the spherical mirror and the lens which feeds the beam into the monochromator.

This smallest aperture in the optical beam path is given by a periscope and has a value of b =1.8 cm. Thus the critical angle of emission α_c can be easily calculated using trigonometry (see Fig. 2.25):

$$\tan(\alpha_c) = \frac{b/2}{l} \Rightarrow \alpha_c = \tan^{-1}\left(\frac{b/2}{l}\right) = 20^\circ \tag{2.22}$$

The critical angle of emission, is the angle of the beam emitted from the sample, which is the most off the optical axis and still being caught by the PL set up. From this critical angle an angular aperture of 40° and a numerical aperture of 0.34 can be calculated.

A first estimate of what fraction of the emitted PL can be expected to be caught by the detection system can be made utilizing the detection system's solid angle (Ω), which can be calculated using the critical emission angle α_c:

$$\Omega = \int_0^{2\pi}\int_0^{+\alpha_c} \sin\theta \; \mathrm{d}\theta\mathrm{d}\phi = 2\pi \cdot \int_0^{+\alpha_c} \sin\theta \; \mathrm{d}\theta = 2\pi \cdot (1 - \cos\alpha_c) \approx 0.38 \tag{2.23}$$

The fraction of the space surrounding the QW which is covered by the PL-detection

system's field of view gives a first estimate of the expected PL emission's yield f. By dividing the field of view's solid angle by the total solid angle (4π) this fraction can be calculated:

$$f \approx \frac{\Omega}{4\pi} \approx 3\% \tag{2.24}$$

Eq. (2.24) gives an estimation of the PL detection system's yield when considering an isotropically emitting point source, which is located inside of a completely homogeneous non-absorbing medium.

In reality, the dipoles, which give rise to the PL emission (electron-hole pairs) oscillate along a certain direction, perpendicular to which the majority of the power is being emitted. Thus, different dipole orientations will lead to different distributions of the emitted radiation. Also the specimen's geometry will have a significant influence on the way the emitted PL propagates. The rough estimate shown in Eq. (2.24) only serves to give a general idea about the fraction of emitted PL intensity, which is expected to be detected.

In order to obtain the total fraction of emitted light, which is being caught inside of the PL detection system's field of view, the scalar product of the normalized Poynting vector's real part $\mathrm{Re}(\vec{P})(\theta,\phi)$ and the corresponding unit vector $\vec{r_0}(\theta,\phi) = (\cos(\theta), \sin(\theta)\cdot\sin(\phi), \sin(\theta)\cdot\cos(\phi))$ is calculated. With these values known the fraction of light falling into the PL detection system's field of view can be calculated:

$$f = \frac{2\pi \int_0^{+\alpha_c} \mathrm{Re}(\vec{P})(\theta,\phi)\cdot\vec{r_0}(\theta,\phi)\sin\theta \ \mathrm{d}\theta}{2\pi \int_0^{+\pi} \mathrm{Re}(\vec{P})(\theta,\phi)\cdot\vec{r_0}(\theta,\phi)\sin\theta \ \mathrm{d}\theta} \tag{2.25}$$

The Poynting vectors are available on a regular θ,ϕ-grid (see Eq. (2.19)). Using the flow of power passing through every $\mathrm{d}\phi\mathrm{d}\theta$-increment ($\tilde{P}(\theta,\phi)$) (Eq. (2.21)) the integrals in Eq. (2.26) can be reformulated to sums. Dividing the power flow which falls into the PL spectrometer's field of view (FoV) by the total outflow of power delivers the fraction of detected PL:

$$f \approx \frac{\sum\limits_{\forall(\phi,\theta)\in \mathrm{FoV}} \tilde{P}(\theta,\phi)}{\sum\limits_{\forall(\phi,\theta)} \tilde{P}(\theta,\phi)} \tag{2.26}$$

Using Eq. (2.26) the geometric yield f is calculated from the monitor data extracted from the FDTD simulations.

2.3.7 The Absorption-Weighted Yield

Combining the laser-absorption behavior and the PL-emission distribution allows to describe the behavior of the detected PL intensity as a function of the tip's geometric evolution during its field evaporation. This is performed by introducing the absorption weighted yield F_l for a specific tip geometry l.

The relative absorption A_l (Section 2.3.4), which describes the absorption of the exciting laser pulse at the QW's position is calculated. This quantity allows to estimate the development of the concentration of generated photocarriers for the different evaporation states of the tip,which can be considered to be proportional to the resulting PL signal. By comparing the A_l values for different evaporation progresses their relative PL intensity can be estimated.

The geometric yield f_l (Section 2.3.5) on the other hand describes the fraction of PL, which falls into the detection system's field of view. This quantity also depends on the simulated tip geometry l. By comparing the f_l-values of different simulated tip geometries, the development of the detection system's detection efficiency can be analysed as a function of the specimen's evaporation progress.

Combining these two quantities (A_l and f_l) allows to represent the development of the detected PL intensity theoretically. The detected PL signal is proportional to both the emitted PL intensity and to the geometric yield. Thus a quantity, which is supposed to explain the behavior of the experimentally observed PL-intensity during the specimen's field evaporation also has to be proportional to both A_l and f_l. The absorption weighted yield F_l is defined as the product of the A_l and f_l:

$$F_l = A_l \cdot f_l \tag{2.27}$$

F_l can thus be considered to be the yield of a specific dipole emission, weighted by the amount of laser-intensity which is being absorbed at the QW's position. The development

of the PL emission during the specimen's field evaporation can be numerically explained by calculating F_l for every simulated tip geometry l.

The absorption weighted yield gives a good description of the detected PL intensity under some specific conditions:

Low Carrier Mobility:

- The estimation of the total emitted PL power in Section 2.3.4 only takes the laser power absorbed at the QW into consideration. Charge carriers are able to move into the QW and are able to drift or diffuse out of the QW. Such migrations, while not taken into consideration, can modify the amount of charge carriers inside of the QW, resulting in modifications of the emitted PL intensity.

- This modification is caused by drift and diffusion. The diffusion's effect can be minimized by performing the experiment at a low specimen temperature. The voltage applied to the specimen generates a high electric field inside of the specimen. This externally applied field penetrates into the specimen for a few nanometers from the specimen's apex (Silaeva et al. (2014)). Thus only for those evaporation states, where the QW is very close to evaporating, the charge carriers will experience any drift effects.

Well Collimated Beam after reflection by the mirror:

- The treatment of the PL emission presented in Section 2.3.4 considers a perfectly collimated beam after the PL's reflection by the utilized spherical mirror. Since the utilized spherical mirror is not a parabolic mirror, there is no possible orientation and position of the mirror, which is able to fully collimate the PL emitted from the specimen. The estimated geometric yields f_k have to be considered upper bounds for fraction of light which is actually being caught by the PL detection set up.

- A parabolic mirror allows a better collimation of the light collected from the specimen. Still the impossibility to change the orientation and position of a parabolic mirror during a measurement would make it hard to obtain perfect alignment of the utilized specimen.

Unless stated otherwise, completely immobile charge carriers and a perfectly collimation of the emitted PL intensity are assumed for the discussion of the absorption weighted yield F_k.

2.3.8 Polarization

This section deals with the general interpretation of the polarization filtered PAP measurements. A major problem for the interpretation comes from the fact that the used spherical mirror does not only change the wave-vector of the incident light (coming from the sample), but also its polarisation. In this section some geometrical considerations about the effect of the mirror and the polarizer on the electric and magnetic field are presented.

Before tackling the electric and magnetic field, it's helpful to first introduce a formalism for the effect of the spherical mirror on the wave vector. In the already introduced coordinate system, the beam line follows the z-axis. For the actual measurement performed by the PAP, the radiation emitted from the quantum well is caught by a parabolic mirror, which guides the wave-vector of the light emitted by the quantum well ($\vec{k_0}$) onto the beam path along the z-axis ($\vec{k_1} = |\vec{k_0}| \cdot \vec{e_z}$), where $\vec{e_z}$ is the unit vector of the z-axis. This can be understood as a linear transformation:

$$\vec{k_0} \rightarrow \vec{k_1} = \mathbf{M}(\vec{k_0})\vec{k_0} = |\vec{k_0}| \cdot \vec{e_z} = |\vec{k_0}| \cdot \begin{pmatrix} 0 \\ 0 \\ 1 \end{pmatrix} \tag{2.28}$$

where $\mathbf{M}$ is a mirror matrix, which is unique for every incident wave vector ($\vec{k_0}$) and guides each incident wave vector into a beam path targeting the μPL set up ($\vec{k_1} = |\vec{k_0}| \cdot \vec{e_z}$).

In the following a method for generating the mirror matrices $\mathbf{M}(\vec{k_0})$ for every incident $\vec{k_0}$, in order to apply $\mathbf{M}(\vec{k_0})$ to the electric ($\vec{E}(\vec{k_0})$) and magnetic ($\vec{H}(\vec{k_0})$) field vector in order to obtain their values after reflection is introduced.

A mirror matrix in 3D has three Eigenvalues. The single Eigenvalue λ =-1, has an Eigenvector ($\vec{m_1}$) which is the normal vector of the mirror plane and the double Eigenvalue λ =+1, which has an Eigenspace ($\vec{m_2}, \vec{m_3}$) that forms the mirror plane. All these Eigenvectors can be constructed from the incident wave vector $\vec{k_0}$ and the fixed reflected wave vector $\vec{k_1} = |\vec{k_0}| \cdot \vec{e_z}$ (see: Fig. 2.26).

The mirror plane's normal vector is proportional to the difference between the incident and the reflected beam, while the first Eigenvector is proportional to their sum. The final

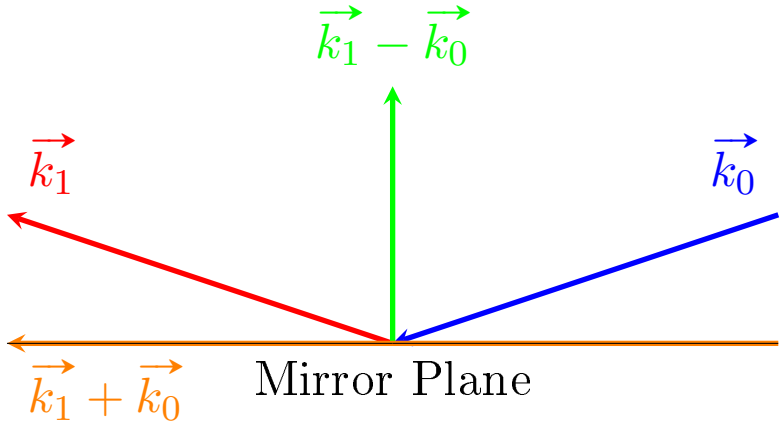

Figure 2.26: Construction of the Eigenvectors of $\mathbf{M}$ ($\vec{k_0} + \vec{k_1}$ and $\vec{k_0} - \vec{k_1}$) by linear combinations of the incident ($\vec{k_0}$) and the resulting ($\vec{k_1}$) wave vectors.

Eigenvector $\vec{m_3}$ can be constructed from the vector product of these two vectors:

$$\begin{aligned}
\vec{m_1}(\vec{k_0}, \vec{k_1}) &= \frac{\vec{k_0} - \vec{k_1}}{|\vec{k_0} - \vec{k_1}|}, \ \lambda_1 = -1, \\
\vec{m_2}(\vec{k_0}, \vec{k_1}) &= \frac{\vec{k_0} + \vec{k_1}}{|\vec{k_0} + \vec{k_1}|}, \ \lambda_2 = +1, \\
\vec{m_3}(\vec{k_0}, \vec{k_1}) &= \vec{m_1} \times \vec{m_2}, \ \lambda_3 = +1
\end{aligned} \tag{2.29}$$

With all Eigenvalues and Eigenvectors known the mirror matrix is constructed for every incident ($\vec{k_0}$) and reflected ($\vec{k_1}$) wave vector:

$$\mathbf{M} = (\vec{m_1}, \vec{m_2}, \vec{m_3})(\lambda_1 \vec{e_x}, \lambda_2 \vec{e_y}, \lambda_3 \vec{e_z})(\vec{m_1}, \vec{m_2}, \vec{m_3})^{\mathrm{T}} \tag{2.30}$$

Since the detection system's field of view is only able to catch the radiation, which is reflected towards it, $\frac{\vec{k_1}}{|\vec{k_1}|} = (0,0,1)^T$ is fixed. $\mathbf{M}(\vec{k_0})$ can be calculated computationally for every incident wave-vector $\vec{k_0}$ of the parabolic mirror.

The effect of the parabolic mirror is described as the linear transformation M_T. Knowing the mirror matrix for an incident wave vector allows to access the change in electric and magnetic field components after reflection, using the same linear transformation as for the wave vector (see Eq. (2.28)):

$$M_T : \vec{E_0}(\vec{k_0}) \rightarrow M_T(\vec{E_0}) = \vec{E_1}(\vec{k_0}) = \mathbf{M}(\vec{k_0})\vec{E_0}(\vec{k_0}) \tag{2.31}$$

$$M_T : \vec{H_0}(\vec{k_0}) \rightarrow M_T(\vec{H_0}) = \vec{H_1}(\vec{k_0}) = \mathbf{M}(\vec{k_0})\vec{H_0}(\vec{k_0}) \tag{2.32}$$

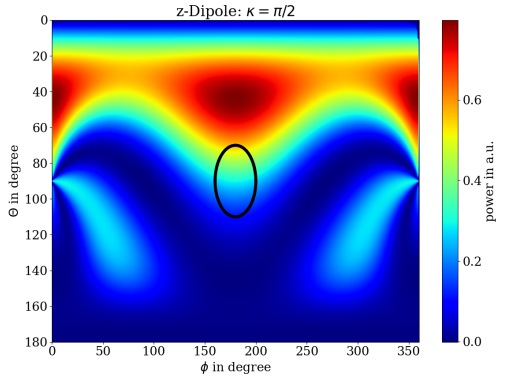

Figure 2.27: Emission map of the z-oriented dipole, with the electric field's y-component removed after reflection.

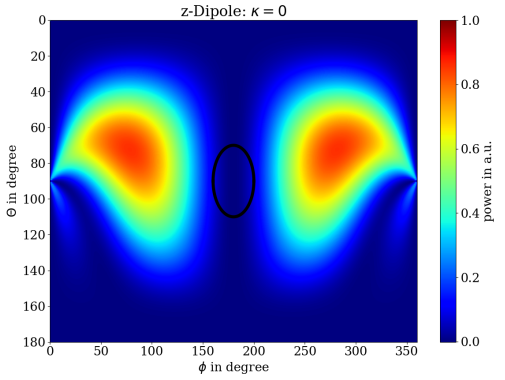

Figure 2.28: Emission map of the z-oriented dipole, with the electric field's z-component removed after reflection.

Using the electric and magnetic field after light's reflection by the mirror ($\overrightarrow{E_1}(\overrightarrow{k_0})$ and $\overrightarrow{H_1}(\overrightarrow{k_0})$), the effect of the Polarizer after the reflection by the parabolic mirror is described by the linear transformations E_T and H_T. The polarization filter removes the electric field component of its orientation (κ). The Polarizer is described by two filtering vectors $\overrightarrow{p_E} = (0, \cos(\kappa), \sin(\kappa))$ (for $\vec{E}$) and $\overrightarrow{p_H} = (0, \sin(\kappa), \cos(\kappa))$ (for $\vec{H}$).

$$E_T : \overrightarrow{E_1}(\overrightarrow{k_0}) \rightarrow E_T(\overrightarrow{E_1}(\overrightarrow{k_0})) = \overrightarrow{E_2}(\overrightarrow{k_0}) = (\overrightarrow{p_E} \cdot \overrightarrow{E_1}) \cdot \overrightarrow{p_E} \tag{2.33}$$

$$H_T : \overrightarrow{H_1}(\overrightarrow{k_0}) \rightarrow H_T(\overrightarrow{H_1}(\overrightarrow{k_0})) = \overrightarrow{H_2}(\overrightarrow{k_0}) = (\overrightarrow{p_H} \cdot \overrightarrow{H_1}) \cdot \overrightarrow{p_H} \tag{2.34}$$

By applying both linear transformations to the amplitudes of the electric field ($\overrightarrow{E_0}$) and magnetic field ($\overrightarrow{H_0}$) are obtained from the simulation results. The effects of both the mirror and the polarizer are introduced as $\overrightarrow{E_2} = E_T(M_T(\overrightarrow{E_0})))$ and ($\overrightarrow{H_2} = H_T(M_T(\overrightarrow{H_0})$.

From these values the Poynting vector effected by the mirror and polarizer, can be calculated for every $\overrightarrow{k_0}$ (wave-vector before reflection) and κ (polarizer orientation):

$$\overrightarrow{P_2} = \overrightarrow{E_2} \times \overrightarrow{H_2}^* \tag{2.35}$$

By inserting this calculated Poynting vector into Eq. (2.21), the distribution of the emitted PL power is calculated. Using Eq. (2.26), the emitted power, which is able to pass through polarizer is then calculated.

Two orientations of the polarizer were taken into consideration for the evaluation of the performed polarization simulations. The y-component ($\kappa = \pi/2$) and the z-component ($\kappa = 0$) of the electric field ($\overrightarrow{E_1}$) were filtered out after reflection.

The emission maps generated using this method to simulate the Polarizer show the

emitted power as a function of the orientation of the original wave-vector before reflection through the mirror ($\vec{k_0}$). Fig. 2.27 and Fig. 2.28 show the emission maps of a z-oriented dipole with the y and z-component filtered respectively. The circle in the middle represents the solid angle which is detected by the μ-PL. The generation polarization resolved emission maps was performed from the same FDTD dataset, which results in the emission map Fig. 2.24 when considering any polarization filtering. After the FDTD simulation, the algebraic operations presented in this section were applied on the output data. It has been confirmed that the emission power distribution shown in Fig. 2.24 indeed is the same as the sum of the two polarizer filtered emission maps Fig. 2.27 and Fig. 2.28.

3. Light-matter interaction within a ZnO Quantum Well

In this chapter the two publications to which the work performed in the context of PhD-thesis have contributed are presented. The material system investigated in both these works is a (Mg,Zn)O/ZnO double quantum well system (Fig. 3.1, Chauveau et al. (2008)). From this planar MBE grown specimen (Section 2.1.1) the APT specimen (Fig. 3.1) which are investigated in this chapter are lifted-out. The PAP experiments on which this chapter is based were performed by Pradip Dalapati.

In Section 3.1 a polarization resolved PAP study of the material system is performed. By comparing these results with PL emission simulation (FDTD), information on the orientation of the PL emitting dipoles can be extracted. Polarization-resolved photoluminescence (PL) and micro-photoluminescence (μPL) yields important information for

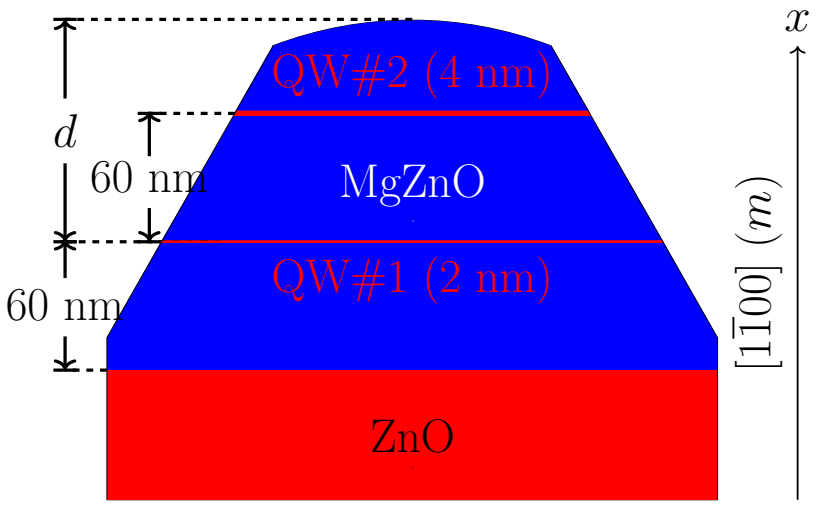

Figure 3.1: The geometry of the sample. The growth direction of the Wurtzite heterostructure is the [1$\bar{1}$00]-direction. The depth of analysis d serves to describe the evaporation progress for the different simulated geometries.

the study of the optical properties of solids. The light emitted by radiative dipoles embedded in solids can be characterized by specific polarization properties that depend on the selection rules of the dipole itself (these, in turn, depend on factors such as the symmetry of the system or the overlap of electronic wavefunctions involved in the transition) but may also depend on the specific shape of the emitting system via the contrast between the refractive indexes of the emitting and of the surrounding medium. This interplay between intrinsic selection rules and system morphology has been previously highlighted in studies on the polarization properties of nanowires: as an example, very thin nanowires tend to emit light polarized along their main axis (x-polarization) unless a selection rule, which may be typical of crystal structures, defects or quantum emitters, forces a polarization perpendicular to the axis (y-polarization) (Ruda and Shik (2005), Rigutti et al. (2010)).

The interest for the study of polarization-resolved PL from nanoscale systems is not limited to nanowires: it has become recently possible to isolate a few or even single quantum-confined light emitters within nanoscale objects realized with a top-down approach, as in the case of lamellas or field-emission tips obtained by focused ion beam (FIB). These structures have a particular interest in correlative microscopy, as they open up the possibility to study the same system by optical spectroscopy (PL (Rigutti et al. (2014), Mancini et al. (2016), Di Russo et al. (2017)) or cathodoluminescence (Schmidt et al. (2015)), spatial modulated spectroscopy (Vella et al. (2018)), etc.) and by microscopy technique with atomic or nearly-atomic spatial resolution, such as transmission electron microscopy (TEM) or atom probe tomography (APT). The correlative analysis may be conducted ex-situ, through a sequential approach (Dalapati et al. (2021)), or even in-situ, as in the case of a CL-equipped TEM or in the recently demonstrated Photonic Atom Probe (PAP) (Houard et al. (2020), Di Russo et al. (2020)). This work is related to this last technique, as it exploits the PAP environment in order to study polarization-resolved μPL from nanoscale tips containing a ZnO-(Mg,Zn)O heterostucture. This last structure has been previously studied by a PAP approach, revealing the optical signatures of the strain induced by the electric field applied to the tip apex in order to promote ion evaporation (Dalapati et al. (2021)).

However, these previous studies did not consider the information carried by the polarization of the emitted light. This issue is addressed in Section 3.1 by focusing on the main spectral components of the PL spectra, i.e. the emission from the ZnO substrate, from the (Mg,Zn)O alloy and, in particular, from the ZnO quantum well.

In Section 3.2 the physical meaning of the PL intensity emitted by the system is the subject of investigation. By simulating both the specimen's laser absorption and PL emis-

sion behavior, the experimentally obtained detected intensities can be reproduced when taking into account the modulation of the tip's optical properties due to the high electric field. Quantum Structures embedded in nanoscale objects show promising properties for their utilization in devices like phosphorescent media (Lee et al. (2000), LEDs Anikeeva et al. (2007)) or for Photovoltaics (Nozik (2002)). Furthermore, they are studied because the coupling of their optical properties with the environment through mechanical (Yeo et al. (2014), Munsch et al. (2017)), thermal (Haro-González et al. (2012)), electrical (Cadeddu et al. (2017)) or magnetic (Jeannin et al. (2017)) effects opens interesting perspectives in the framework of advanced spectroscopy and quantum sensing. In particular, cone-shaped light collectors (Schmitt et al. (2015)) with embedded nanostructures (Tumanov et al. (2018), Kettler et al. (2021), Yeo et al. (2014)) have a geometry adapted to microscopic analysis by transmission electron microscopy or laser-assisted atom probe tomography (La-APT) (Rigutti et al. (2014)).

Furthermore, the PL issued from an evaporating tip exhibits energy and intensity variations. The observed shifts in the energy of quantum well's PL-response have been shown to be related to field-induced mechanical stress and allow thus for its optical measurement (Rigutti et al. (2017), Dalapati et al. (2021)). On the other hand, the mechanisms determining the detected PL signal's intensity as a function of the evaporation progress are still poorly understood.

This specific problem is the object of this section, in which we analysed the elementary case of the PL emission from a single ZnO/(Mg,Zn)O quantum well as a function of the evaporation progress. Our approach consists in the calculation of absorption maps and emission patterns of a dipole localized in the quantum well contained in an APT specimen with evolving shape due to evaporation. Beyond that, we also consider different possible effects which modify the surface's optical properties.

The modification of the surface optical properties of the needle-shaped specimen can be caused by the specimen preparation by focused-ion-beam (FIB), but also by the high electric field ($\approx 10^{10}$ V/m), which is applied during the APT measurement (Section 2.3.3). The calculation is then compared to the experimental evolution of the PL intensity as a function of the progress of the evaporation, which also provides a means to evaluate the specific contribution of each of these effects.

The concepts developed in this chapter provide a better instrumental understanding of the PAP, leading to improved capabilities to interpret its correlated APT/PL information and to open the PAP methodology to the systematic interpretation of the signal generated from more complex semiconductor heterostructures or other materials systems analyzable by APT.

3.1 Polarization Behavior of a non-evaporating PAP specimen

The results shown in this section are published in "Polarization-resolved photoluminescence study of an atom probe tip containing a ZnO-(Mg,Zn)O heterostructure" (Dalapati et al. (2022)).

The PAP experiment which provides the PL information that is the experimental basis for this work was performed at zero voltage making this an in-situ-experiment. The polarization analysis of the specimen's PL response was performed by inserting the polarizer into the PAP set-up (Fig. 2.13). Despite decreasing the PL intensity detected by the PAP's PL spectrometer, this allows to pick the polarization of the light which is guided towards the PAP's PL detection set-up.

Additionally the influence of the specimen orientation on the polarization resolved PL emission is studied. By rotating the specimen in its sample holder around its main axis before its insertion into the measurement chamber the crystallographic direction which is aligned along the optical axis can be chosen to be any direction which lies inside of the QW-plane (see Fig. 2.22). Since the QWs studied in this work are grown along the apolar $[1\,\bar{1}\,0\,0]$-axis, the QW plane is constituted by the apolar $[1\,1\,\bar{2}\,0]$-axis as well as the polar $[0\,0\,0\,1]$-axis.

While the laser pulse which is used to excite the specimen always has an electric field that is oriented along the tip's main axis, resulting in the excitation of dipoles oriented along the crystallographic $[1\,\bar{1}\,0\,0]$-axis independent of the tip's rotational orientation, the emitted PL intensity can be expected to depend on the tip's orientation.

In this section we present the FDTD simulations (Section 2.3) which serve to explain the polarization-resolved PAP-obtained PL signal emitted from an APT tip consisting of a ZnO/(Mg,Zn)O QW heterostructure. The QWs are oriented perpendicular to the tip's main axis.

Here it is shown that the polarization of the PL emission is different for the (Mg,Zn)O barrier material and the ZnO QW which is embedded in it. The results of the polarization resolved FDTD simulations (Section 2.3.8) are able to conclude the orientation of the dipole emitters which constitute the specimen's optical response when taken into the context of the experimentally observed polarization behavior.

3.1.1 Microscopic characterization

The fashion of how the PAP specimen is lifted out from the planar sample is detailed in Blum et al. (2016). A specimen which is lifted out from the sample (Mg,Zn)O-sample (Section 2.1.1) is reported in the scanning electron micrograph in Fig. 3.2c. Consistent results were obtained from four different tip specimens.

The thickness of the different layers and the alloy composition of the (Mg,Zn)O barriers were designed in order to avoid plastic relaxation. The structure is visualized in two different orientations in the electron tomography (ET) images reported in Fig. 3.2a. The ET experiments were performed by Z. Saghi (Univ. Grenoble Alpes, CEA, Leti, Grenoble F-38000, France). The two QW have been numbered here in the order of their growth. Their thicknesses are $t_1 = (2.0 \pm 0.1)$ nm and $t_2 = (3.9 \pm 0.1)$, respectively. Notice that, as TEM performed at 200 keV may damage the sample introducing non-radiative recombination centers, the tip specimen reported in Fig. 3.2a is not one of those analysed by PAP and by polarization-resolved μPL. The substrate-alloy interface and the QW interfaces are clearly marked by a serrated profile, a morphological feature

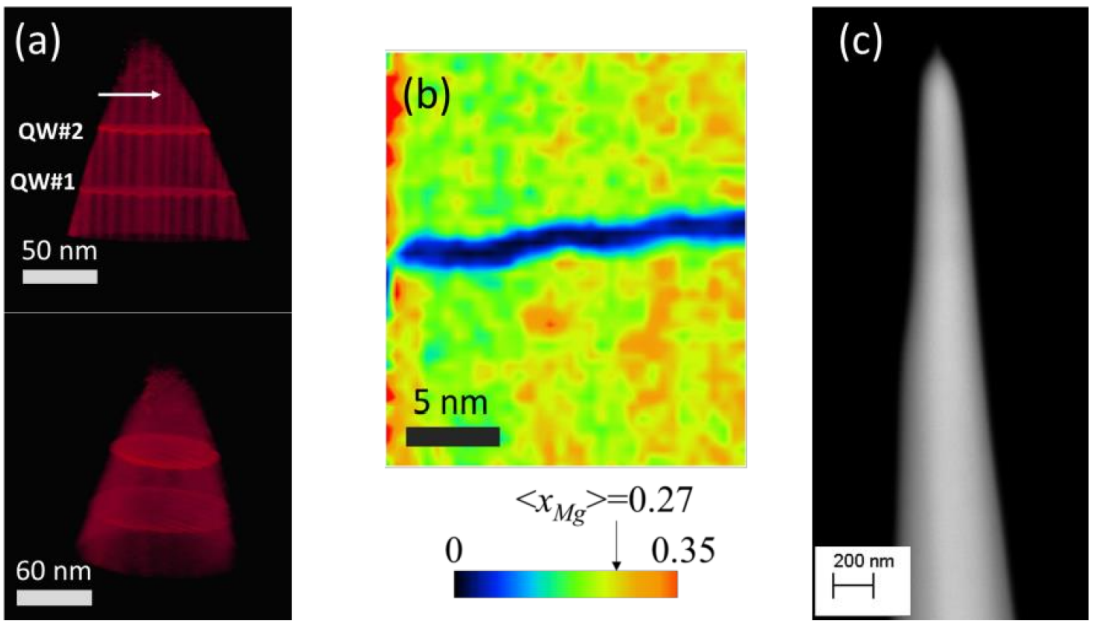

Figure 3.2: The system under study. (a) Electron tomography image of a tip apex containing the ZnO/(Mg,Zn)O heterostructure. (b) Mg site fraction map issued from atom probe tomography analysis of the tip. The fraction map refers to a 2 nm thick slice containing the QW#1. (c) Scanning electron micrograph of the tip studied in this work, as prepared by focused ion beam (Dalapati et al. (2022)).

propagating throughout the epitaxial growth of the structure (Di Russo et al. (2017)). This profile has been found to be related to compositional inhomogeneities within the barriers, with the formation of Zn- and Mg- enriched regions corresponding to the edges pointing towards the substrate and towards the upper surface, respectively. This feature, along with the QW interface profile, is visible in both the top ET image, oriented along the [0 0 0 1]-crystal axis, and on the composition map extracted from APT analysis and reported in Fig. 3.2b. The mechanism leading to such features and its effect on the electronic properties of the system have been discussed in previous works (Di Russo et al. (2017), Dalapati et al. (2021)). According to APT results, the average Mg site fraction, is $< x_{\mathrm{Mg}} >= 0.27$.

3.1.2 Polarization-resolved PL

Unpolarized and polarization-resolved spectra have been collected for two tip orientations, i.e. with the $[1\,1\,\bar{2}\,0]$-axis and with the [0 0 0 1]-axis of the crystal parallel to the optical z-axis. Polarized spectra were collected by varying the polarizer angle by steps of 10°. Within the polarizer reference frame, 0° corresponds to the electric field polarized along the tip axis (x), while 90° corresponds to y-polarization (see: Fig. 2.22). Fig. 3.3 reports the results of the optical spectroscopy study. Selected PL spectra from the tip with the $[1\,1\,\bar{2}\,0]$-axis oriented along the optical axis (in the following, we will refer to this configuration as to the "$[1\,1\,\bar{2}\,0]$-oriented tip", while the alternative configuration will be referred to as the "[0 0 0 1]-oriented tip") are displayed in Fig. 3.3a. For the same integration time (60 s) the unpolarized spectrum is, as expected, around one order of magnitude more intense than the filtered spectra. The decrease of PL intensity upon polarization filtering is the main reason why an analysis of the entire tip's evaporation process as shown in Dalapati et al. (2021) was not performed in a polarization filtered manner. The required illumination time would increase the time required for the PAP measurement by an order of magnitude. Three main spectral contributions can be recognized, the assignments having been discussed in previous works (Di Russo et al. (2020), Dalapati et al. (2021)): the (Mg,Zn)O barrier exhibits a broad emission peaked at the energy E =3.9 eV, the QW#1 has a narrower peak at E =3.47 eV, while the ZnO substrate is peaked at E =3.38 eV and displays a sub-bandgap structure which is partly related to phonon replicas. The polar diagrams of the $[1\,1\,\bar{2}\,0]$-oriented tip, reporting the dependence of the intensity of each spectral component (normalized to its maximum) on the polarizer angle, are shown in Fig. 3.3b, and clearly point out that the ZnO substrate and the (Mg,Zn)O barrier emit moderately x-polarized light, while the QW is moderately y-polarized. The

polarization ratios, defined for each spectral component as $P = (I_y - I_x)/(I_y + I_x)$, are reported in Table 3.1. The intensities I_y and I_x are determined on the basis of the cosine square fit of each polar diagram.

The results of the measurements performed on the [0 0 0 1]-oriented tip are displayed in Fig. 3.3c,d. The polarization behavior of the three spectral components is similar to that recorded for the [1 1 $\bar{2}$ 0]-orientation, with the main difference that the QW signal becomes here strongly y-polarized (P_{QW}=0.76).

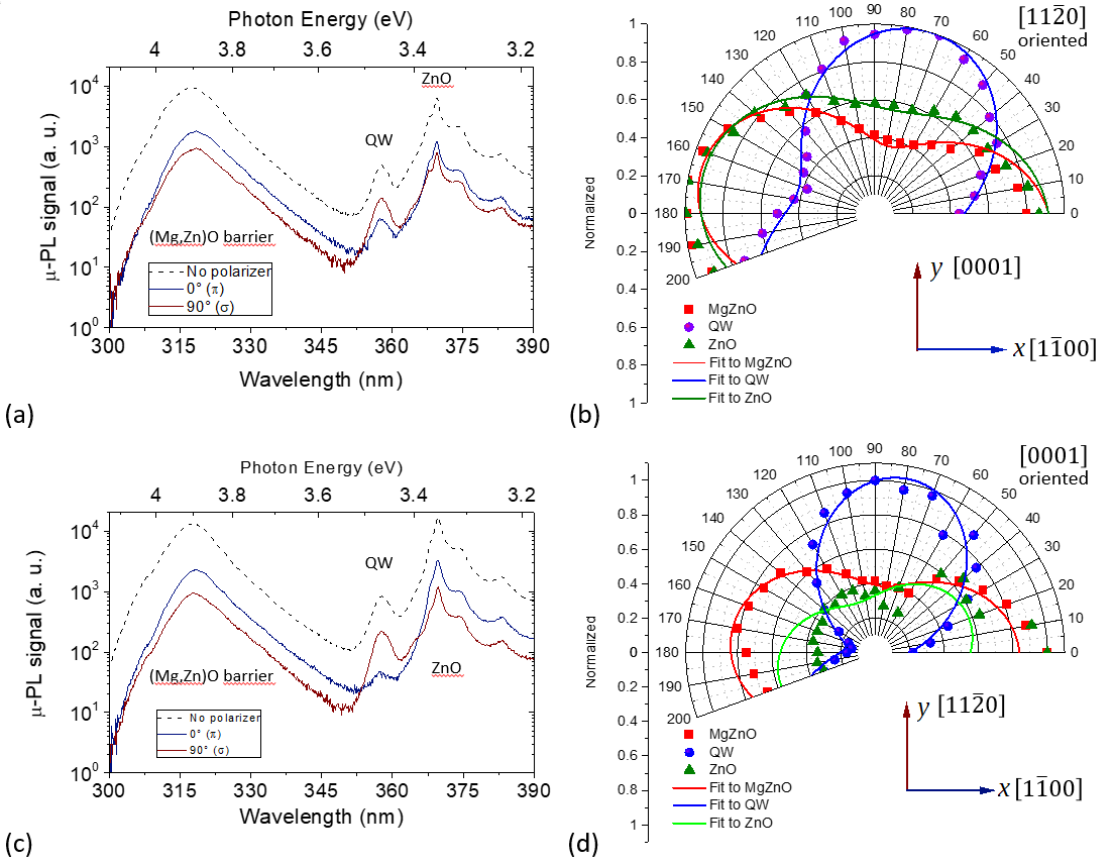

Figure 3.3: Polarization-resolved PL from the atom probe tip: (a) Unpolarized and selected polarized PL spectra from the tip and (b) polarization diagram from the three main spectral components ((MgZn)O barrier, QW#1 and ZnO substrate) when the optical axis corresponds to the [1 1 $\bar{2}$ 0] direction. (c) Unpolarized and selected polarized PL spectra from the tip and (d) polarization diagram from the three main spectral components when the optical axis corresponds to the [0 0 0 1] direction. (Dalapati et al. (2022))

Table 3.1: Polarization ratios ($P = (I_y - I_x)/(I_y + I_x)$) for the different spectral components and tip orientations.

Tip Orientation	ZnO (3.38 eV)	QW#1 (3.47 eV)	(Mg,Zn)O (3.9 eV)
$[1\,1\,\bar{2}\,0]$	-0.27	0.45	-0.44
$[0\,0\,0\,1]$	-0.58	0.76	-0.36

3.1.3 Calculation of Polarization-resolved far field patterns

The studied system differs significantly from a dipole emitting in an isotropic medium. In order to correctly interpret the measured polarization patterns and ratios, we have performed finite difference time domain (FDTD) calculations of the emission patterns of three main dipole orientations, as illustrated in the first column of Fig. 3.4, corresponding to a dipole oriented along the x-axis (tip axis, always $[1\,\bar{1}\,0\,0]$-direction), along the y-axis and along the z-axis (optical axis).

The results of the calculations for the x-oriented dipole emission from QW#1 are displayed in Fig. 3.4a. As expected, the emission pattern is invariant with respect to the rotation around the tip axis. The yield of the detection system, reported in Table 3.2, is around 3.96 % for the x-polarized light, and negligible for the y-polarized light, resulting in a polarization ratio of around -1. A different picture results from the y-oriented dipole, as in Fig. 3.4b. The yield for this dipole is 3.46 % and the detected light is almost exclusively y-polarized, with a polarization ratio close to 1. An intermediate situation concerns the dipole oriented along the optical axis, presented in Fig. 3.4c. As a result of system anisotropy, there is significant light coupling into the spectrometer, with a total yield ($y + x$ polarizations) of 1.4 %, comparable to that of the dipoles oriented perpendicularly to the optical axis. Although the light coupled into the spectrometer is mostly x-polarized, a weaker but significant portion of y-polarized light is also detected, yielding a polarization ratio of -0.87. These facts should be considered when analyzing experimental polarization patterns, as they indicate that the polarization of the light may be significantly influenced by a radiating dipole oriented along the optical axis.

3.1.4 Discussion of the Polarization of the emitted PL

The experimental results and the FDTD calculations allow us to draw several conclusions on the optical properties of the studied sample. The main experimental results point out that the polarization of the ZnO and (Mg,Zn)O emission is moderately oriented along the tip axis, while the QW emission is more strongly polarized perpendicularly to the tip axis, i.e. in the QW plane.

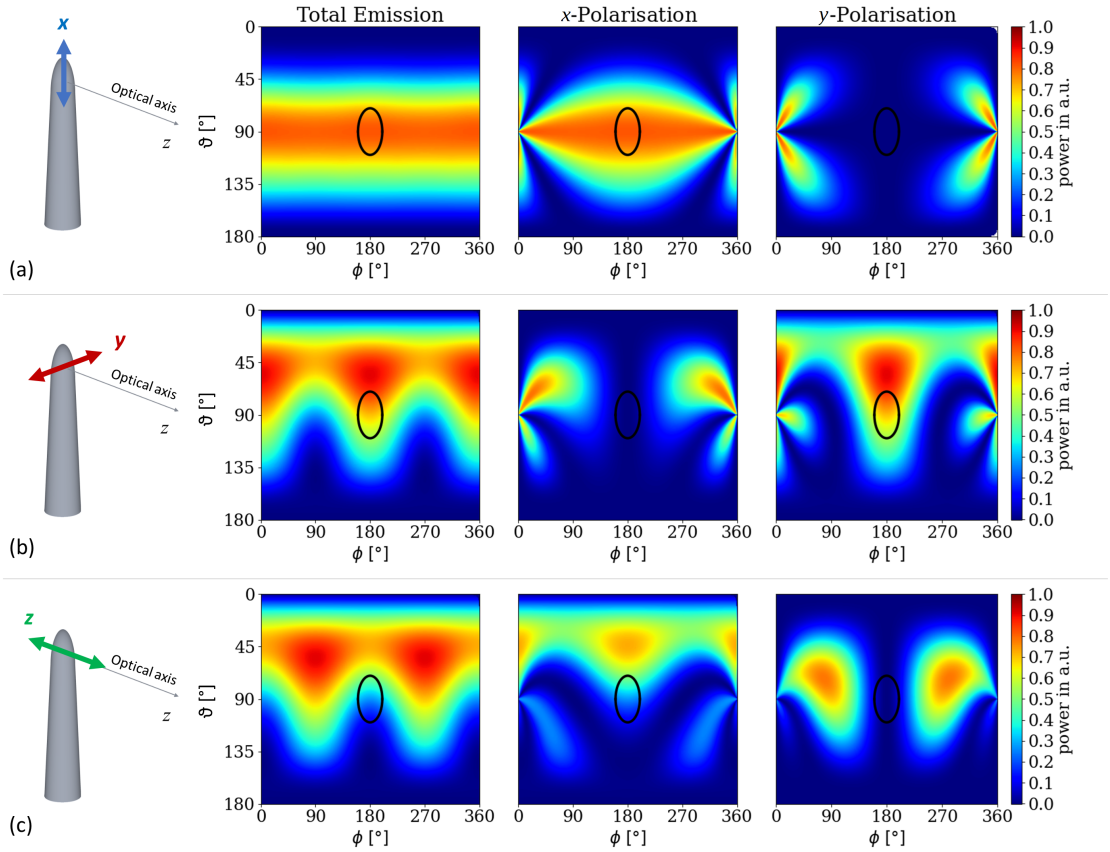

Figure 3.4: Finite-difference time domain (FDTD) calculations showing the three main dipole orientations (first column) and the emitted radiation patterns: total emission (second column), emission detected as x-polarized (third column) and emission detected as y-polarized (fourth column). Line (a) refers to a dipole oriented along the x-axis (alyways crystal $[1\,\bar{1}\,0\,0]$-axis||tip axis), line (b) to a dipole oriented along the y-axis, while line (c) to a dipole oriented along the optical axis. The black circle superimposed to the emission patterns corresponds to the field of view of the spectrometer, as presented in Section 2.3.6. (Dalapati et al. (2022))

3.1.4.1 ZnO substrate

According to past studies (Jacopin et al. (2011)), the ZnO-substrate's signal should appear as strongly polarized perpendicularly to the $[0\,0\,0\,1]$-axis. This would imply a high degree of x-polarization with the tip in the $[1\,1\,\bar{2}\,0]$-orientation and a significantly lower degree of x-polarization with the tip in the $[0\,0\,0\,1]$-orientation. The experimental results, on the contrary, display a moderate y-polarization in both orientations. This is most likely due to the morphology of the tip (we remind that the simulation of the

Table 3.2: Calculated yields in % and polarization ratios for the three main dipole orientations.

		Dipole orientation		
		x	*y*	*z*
Yields (%)	*y* – polarization	0.0006	3.41	0.097
	x - polarization	3.93	0.038	1.36
Polarization Ratio		-0.9997	0.98	-0.87

ZnO substrate does not fall within the scope of our calculations) and to its waveguide effect, which could significantly mix different polarization components from an extended distribution of emitting dipoles.

3.1.4.2 (Mg,Zn)O barrier

A similar situation is found in the case of the (Mg,Zn)O-barrier emission. It is interesting to notice that a previous study of the polarization dependence the absorption edges of m-plane (Mg,Zn)O layers indicates that the lower-energy absorption edge is perpendicular to the [0 0 0 1]-axis for $x_{\mathrm{Mg}} < 0.24$, then the polarization is inverted and for higher Mg content the lower-energy absorption edge is parallel to the [0 0 0 1]-axis (Neumann et al. (2016)). The data from this work indicate a polarization behavior similar to the ZnO. Care should be taken when comparing the two emissions because they are not localized within the same portion of the tip. However, the (Mg,Zn)O emission is more strongly x-polarized when the tip is $[1\,1\,\bar{2}\,0]$-oriented, which suggests a weaker emission from [0 0 0 1]-oriented dipoles. This is in agreement with past works, as we can notice that the average content of the (Mg,Zn)O alloy is $x_{\mathrm{Mg}} = 0.27$, but it is highly inhomogeneous, and it is reasonable to expect that most optical transitions will be due to carriers localized within regions with $x_{\mathrm{Mg}} < 0.27$.

3.1.4.3 ZnO/(Mg,Zn)O quantum well

Most interestingly, the QW#1 emission is polarized perpendicularly to the tip axis, and this y-polarization is stronger when the tip is [0 0 0 1]-oriented. Previous works on the polarization of the PL emitted from thin films containing $[1\,\bar{1}\,0\,0]$-plane ZnO/(Mg,Zn)O quantum wells reported that the PL is strongly polarized perpendicular to the [0 0 0 1]-axis (Matsui and Tabata (2009)). The results of our experimental work differ from those of Matsui and Tabata (2009). On one hand, the polarization along $[1\,\bar{1}\,0\,0]$ appears to be suppressed for the QW PL. On the other hand, when the tip is $[1\,1\,\bar{2}\,0]$-oriented (crystal

$[1\,1\,\bar{2}\,0]$-direction along the optical axis) the light is y-polarized, i.e. polarized along $[0\,0\,0\,1]$, which contradicts the results of Matsui and Tabata (2009). If a certain amount of light from an $[1\,1\,\bar{2}\,0]$-oriented dipole could still couple into the detector, as suggested by the FDTD calculations, it should nevertheless inject in it mostly x-polarized light. This leads us to conclude that the QW#1 PL is mostly polarized within the $[1\,\bar{1}\,0\,0]$-plane. The reason why this occurs is not completely clarified, but some hypotheses can be discussed. It is unlikely that the unusual polarization behavior of QW#1 is driven by the strain relaxation of the barrier. The (Mg,Zn)O alloy is indeed grown as a thin film epitaxially strained on the ZnO substrate. Under these conditions, the QW#1 is unstrained. When a tip is fabricated by FIB, the strain in the heterostructure can partly relax at lateral surfaces, producing in inhomogeneous strain state within the barrier and the QW. The maximum strain state within the QW has been evaluated in a previous work (Dalapati et al. (2021)) as $\epsilon_{aa} \approx 0.3$ % and $\epsilon_{cc} \approx -0.4$ %. Under these conditions, the ZnO valence band states retain about 93 % of the character of the unstrained ZnO. Further admixture among valence band states could be originated by quantum confinement and by the mixing with (Mg,Zn)O states. However, this would not explain why the polarization behavior of this system differs from that of Matsui and Tabata (2009). A further possibility is related to the specific morphology of the quantum well, which is known to produce strong carrier localization effects and could thus lead to further mechanisms of band mixing. It is interesting to notice that this specific morphology is at the origin of the intersubband absorption of infrared light with the electric field parallel to the $[1\,\bar{1}\,0\,0]$-plane (Hierro et al. (2019)). The intersubband absorption mechanism is obviously different from the interband emission treated here, but underlines the importance of QW morphology for optical transitions.

3.1.5 Summary of polarization-resolved PL

In summary, we have conducted a study of the polarization properties of the PL emitted by a ZnO/(Mg,Zn)O-quantum well heterostructure embedded in nanoscale tip fabricated by FIB and analyzable by atom probe tomography. As a peculiar feature of this system, it is straightforward to control the orientation of the tip along its axis, and it becomes thus possible to select specific crystal directions to be parallel or perpendicular to the optical axis. As the analysed system has not a standard morphology such as that of a thin film or of a thin nanowire, FDTD calculations were carried out in order to predict the amount of detected light and its polarization for three main orientations of a dipole emitting at the center of the QW.

3.1.5.1 Polarization behavior of the PL from the ZnO/(Mg,Zn)O heterostructure

The measurements conducted on several tips and here reported for one of them indicate that the ZnO and (Mg,Zn)O PL spectral contributions are moderately polarized along the tip axis, which is in reasonable agreement with previous studies on thin films or on nanowires. On the other hand, the QW PL exhibits a y-like polarization that points out to the presence of radiative dipoles both in the $[1\,1\,\bar{2}\,0]$- and in the $[0\,0\,0\,1]$-direction of the crystal. This result disagrees with previous studies. A tentative explanation of this situation should consider the specific QW morphology and the mechanisms of carrier localization that it induces.

3.1.5.2 Polarization-resolved PAP

The study of the polarization-resolved PL within a PAP is an original experimental method which the development of this instrument has recently made possible. Among the benefits of this method is the possibility to change the tip orientation within the measurement chamber in order to gain insights into the orientation of the dipoles which cause the PL emission of the tip and to relate this the specimen's crystallographic axes. However, we have also shown that the interpretation of such information is not straightforward, as the radiation patterns and the polarization of the detected light are strongly influenced by the tip morphology and composition. Another interesting point is the possibility to orient the tip preliminarily to APT analysis, in order to obtain the highest PL signal or the highest polarization ratio for a given spectral component. The acquisition of polarization-resolved PL in-situ and operando during the APT analysis, within the PAP framework, is possible, provided the attenuation of the PL signal by the polarizing filter does not hinder the acquisition of PL spectra with a correct signal-to-noise ratio.

3.2 Development of the detected PL intensity during PAP analysis

The previous study on the "Polarization-resolved photoluminescence study of an atom probe tip containing a ZnO-(Mg,Zn)O heterostructure" (Section 3.1, Dalapati et al. (2022)) was an in-situ investigation of a specimen which only utilized the PL aspect of the PAP technique. The previously presented work served to clarify that the y-dipole emitter orientation is dominant. However the PAP technique also offers the possibility to record the specimen's PL emission during the performance of an APT experiment (in-operando). In this section the specimen is considered to be aranged so that the specimen's [0 0 0 1]-axis is oriented along the optical axis of the laboratory frame.

This section presents our recent works on the "Influence of dynamic morphological modifications of atom probe specimens on the intensity of their photoluminescence spectra" (Weikum et al. (2023)). By simulating the propagation behavior of light inside of a field evaporating APT-tip specimen, which is investigated by the PAP technique, the clarification of the meaning of the intensity obtained during a PAP experiment is the focus of this chapter. We utilize the PL intensity emitted from the QW#1 as a model to study the PL-detection behavior of the PAP which is emitted from a localized PL emitter. By clarifying the PL detection behavior via simulating both the exciting laser pulse's as well as the tip's optical response's with FDTD calculations of a localized emitter we are aiming to gain insights into the general PL detection behavior of more complex systems. This promises to allow us to better understand the PAP-obtained PL-intensity data that we obtain from more complex heterostructure systems.

A PAP specimen under field-evaporation voltage can be expected to show drastically different electro-optical properties than bulk material. In Section 2.3.3 these electric field induced modulations of the specimen's dielectric function, as well as the impact of the FIB-preparation process are discussed. By taking these optical modulations of the APT specimen into consideration a good agreement between the measured and the simulated PL intensity is obtained.

3.2.1 Experimental Conditions of the in-operando PAP experiment

The PAP experiment of the specimen described in Section 2.1.1 (Section 2.2) was performed using a laser pulse (266 nm) with a repetition rate of 400 kHz. The specimen apex is illuminated by a laser spot with size close to 2 μm and an average power of 10 μW. Thus the pulsed laser illuminates the entire apex region of the tip (of the order of

200 nm size). PL spectra were acquired using the 600 lines/mm grating. The CCD array integration time for each acquisition was set to 90 s. During the PAP analysis in which the tip was field-evaporated, the base voltage rose from 6 to 10.3 kV.

3.2.2 Results of the Investigation of a field evaporating PL emitter

3.2.2.1 Photonic Atom Probe Analysis

The results of the PAP analysis are displayed in Fig. 3.5

PL emission has been observed from the ZnO substrate (3.34 eV), the (Mg,Zn)O barrier material (3.89 eV) and from QW#1 (3.46 eV). Each source of the PL emission can be distinguished by its characteristic energy. This work's attention is focused on the PL emission of the QW, which can only be considered as a localized emitter. Selected PL spectra which were recorded during the field evaporation progress are shown in their totality in Fig. 3.5-(a) and in the QW spectral neighborhood of Fig. 3.5-(c). The position of the evaporation front during the shown PL acquisitions is shown in Fig. 3.5-(b). In this 3D reconstruction, only the Mg atoms are shown, thus the two quantum wells correspond to the regions depleted in Mg-atoms. Some of the Mg atoms are shown in color: these Mg atoms shown in color were evaporated while collecting the PL spectrum displayed with the same color in Fig. 3.5-(a,c).

The depth of analysis d is the distance between the evaporation front and the QW#1 and decreases with the progressing field evaporation of the specimen. The evaporation front being at the position of QW#1 corresponds to $d = 0$, while $d > 0$ indicates, that the progressing evaporation has yet to fully destroy QW#1. During the field evaporation of the tip both the QW PL energy and intensity change as a function of the evaporation progress (Fig. 3.5-(c)). The spectral shift has been shown to be caused by an evolution of stress state within QW#1 Dalapati et al. (2021). QW#2 does not emit any PL signal for any specimen. The lack of emission from QW#2 might be caused by focused ion beam induced damages during sample preparation (Dalapati et al. (2021)). Since QW#1 lies below QW#2 and the focussed ion beam is introduced along the tip main axis it is less exposed to FIB damaging.

The intensity of the signal of the ZnO substrate remains mostly constant during the specimen field evaporation. This is reasonable, since the substrate constitutes the majority of the tip volume and does not loose many atoms due to field evaporation. Since it also represents the tip's portion, which is evaporated last, an almost constant behavior of the signal is to be expected.

The PL signal of the (Mg,Zn)O barrier, on the other hand, monotonously decreases

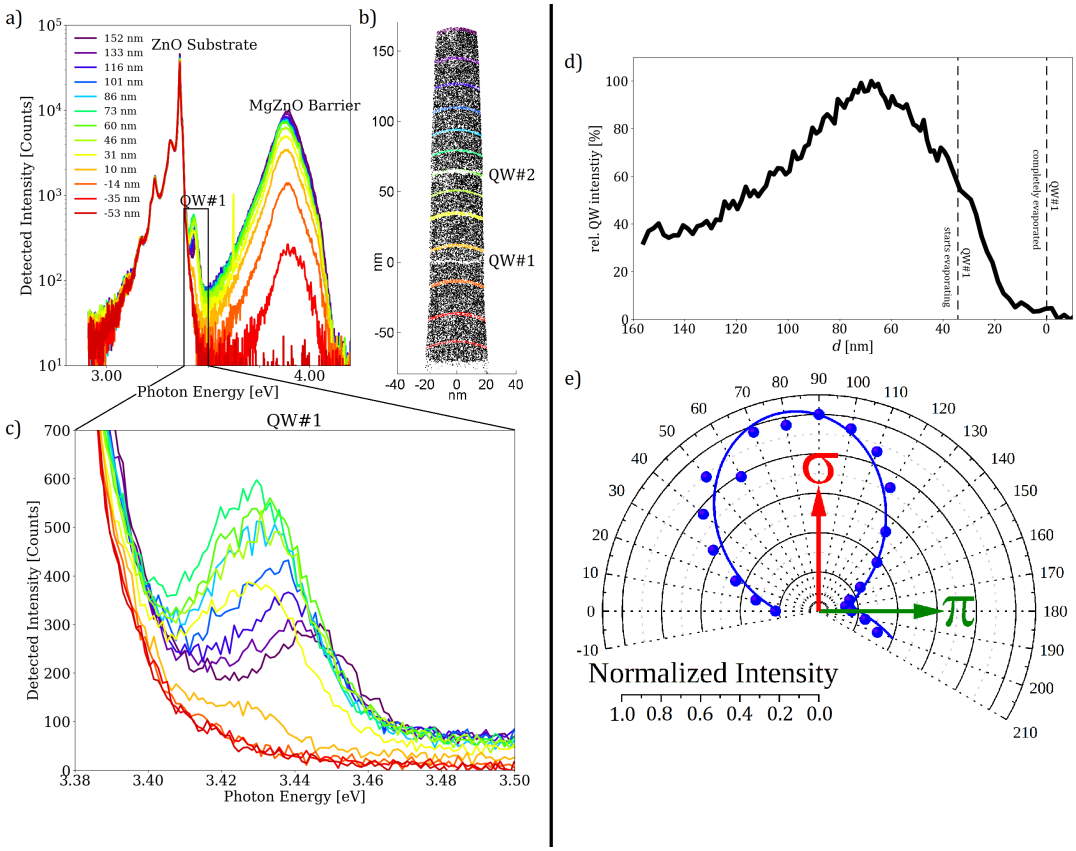

Figure 3.5: a) PL spectra for different evaporation steps Dalapati et al. (2021). The evaporation progress is characterized by the depth of analysis d (see Fig. 3.1). The reconstruction on the right side (b) represents the Mg atoms of the reconstructed volume. Both QWs are visible by the absence of Mg atoms. c) shows the PL response of QW#1. The energy shifts are interpreted in Dalapati et al. (2021). d) the QW's integral PL intensity as a function of the evaporation progress. e) the polarization resolved PL signal of QW#1 for an early evaporation stage. As it is usual in the APT related research, the x-polarization is parallel to the APT tip's main axis and the y-polarization is oriented perpendicular to both the optical path and the tip's main axis. A strong y polarisation can be observed from the experimental data. (Dalapati et al. (2022))

until it vanishes, once the last atoms of the barrier material have been removed from the remaining substrate. Since the characterization of localized PL emission is the focus of this work, the PL emission originating from the barrier and substrate are not the subjects of investigation in this chapter.

The total PL intensity of the QW is calculated by the integration of its spectral signal and can be expressed as a function of the evaporation progress. Fig. 3.5-(d) shows that the QW's PL signal rises during field evaporation in the early evaporation states ($d > 60$ nm). The intensity of the PL emitted by the QW reaches its maximum at $d \approx 60$ nm. This maximum value of the QW's PL intensity represents a more than twofold increase of the initial value. After the maximum of the PL signal is reached, it decreases until the QW#1 has been completely evaporated ($d = 0$).

3.2.2.2 Results of the FDTD calculations

The FDTD (Fig. 3.6) simulations of the specimen's absorption and emission behavior were performed for four different sets of simulation conditions, namely the Non-

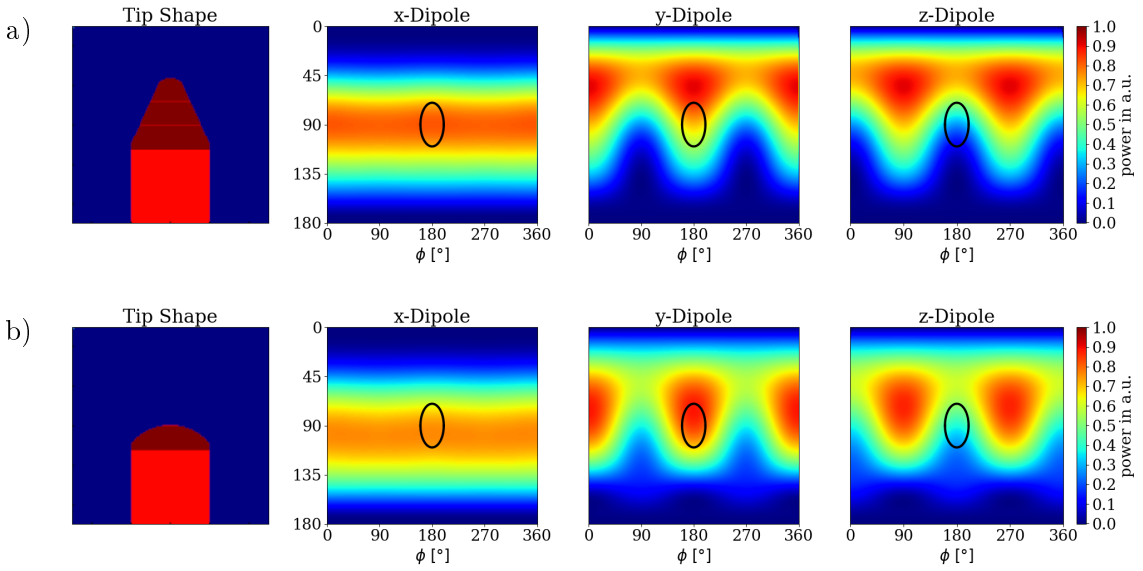

Figure 3.6: Geometric shapes and emission maps for the three dipole orientations of the first (a) and last (b) evaporation state. The field of view of the PL detector is indicated by the black circle the center of the emission maps. For the relation between the axes x, y, z and the polar angle θ as well as the azimuth ϕ, see Fig. 2.22). (Weikum et al. (2023))

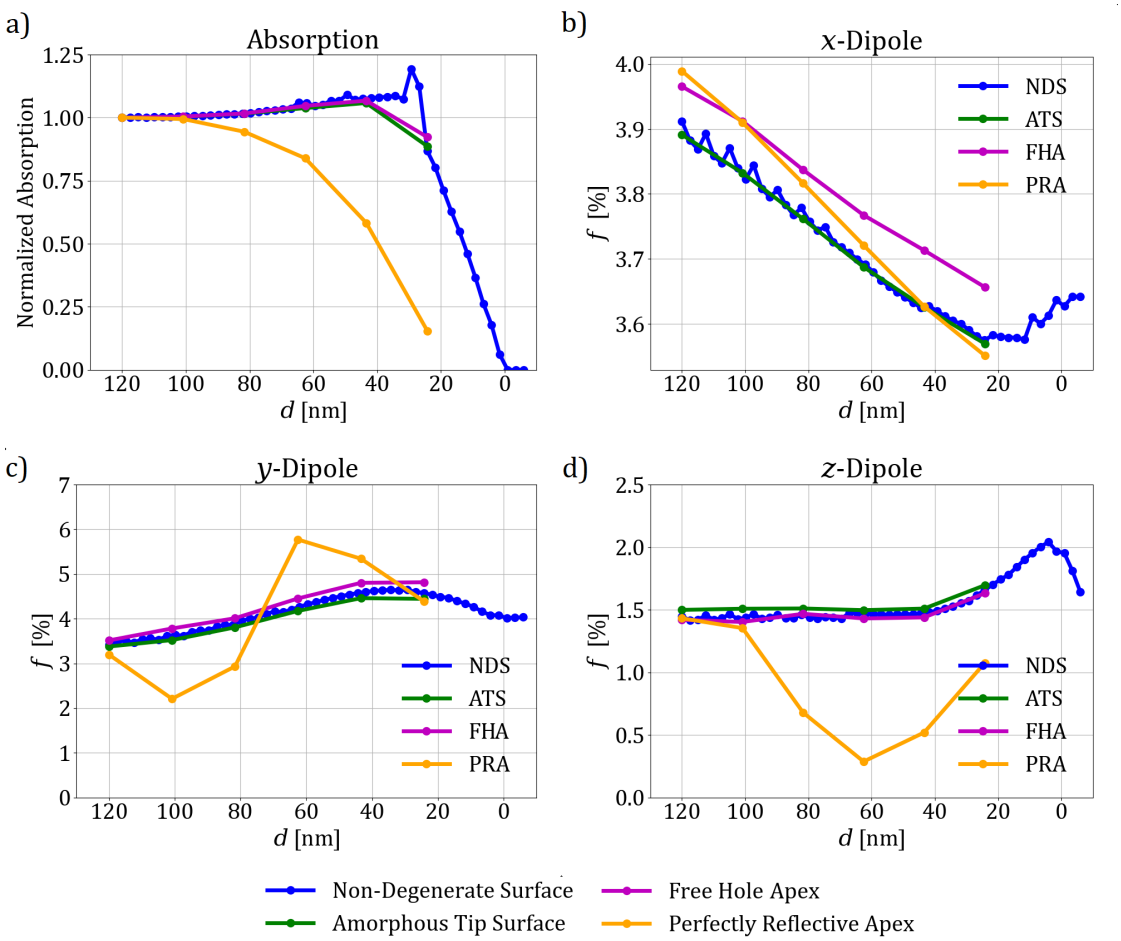

Figure 3.7: The results of the FDTD simulations, which were separately performed on the tip's absorption (a) and the emission (b, c ,d) behavior. The simulations are performed for Non-Degenerate Surface (NDS), Amorphized Tip Surface (ATS), the Free Hole Apex (FHA) and Perfectly Reflective Apex (PRA) conditions (Section 2.3.3). The normalized absorption (a) describes the development of the amount of absorbed laser power and the yield (b ,c, d) show the fraction of emitted light which is being caught by the PL detector's field for view f[%], as a function of the propagating evaporation front for dipole emitters oriented along the x, y, z axis respectively. (Weikum et al. (2023))

Degenerate Surface (NDS) conditions, the Amorphized Tip Surface (ATS) conditions, the Free Hole Apex (FHA) and the Perfectly Reflective Apex (PRA) conditions (Section 2.3.3).

The FDTD simulations on the Non-Degenerate Surface conditions were performed for 47 specimen geometries characterized by different depths of analysis (d), while the Amorphized Tip's Surfaces, Free Hole Apex and Perfectly Reflective Apex conditions

were simulated using a set of six different tip geometries. The results of the development of the relative absorption (Eq. (2.15)) as a function of the specimen evaporation progress (expressed by the depth of analysis d) is shown in Fig. 3.7a. Since the specimen PL emission behavior is a function of the emitting dipole orientation, the simulations were performed considering emission by dipoles oriented along the three cardinal axes x, y and z (see Fig. 2.22). Depending on the orientation of the emitting dipole, the emission pattern and thus also the yield, which is given by the detector's field of view, changes. Fig. 3.7-(b, c, d) shows the yield (Eq. (2.26)) of the differently oriented dipole emissions as a function of the depth of analysis. By multiplying the values of the respective (x, y, z) relative absorption with the yield, the absorption weighted yields are calculated for each dipole orientation. Since each dipole emits most of its power in the plane perpendicular to its orientation, the dipole which is oriented along the set-up's optical axis (z) shows the lowest yields.

Fig. 3.8 shows the simulated absorption weighted yields (F_i, Eq. (2.27)) being compared to the measured QW's PL intensity, which was measured by the experimental Photonic Atom Probe set-up (Dalapati et al. (2021)).

Due to uncertainties about the actual development of the specimen geometry during its evaporation in APT, the FDTD simulation of the APT specimen's PL behavior was performed for an idealized tip's geometry (Section 2.3.2). This approach allows an easier interpretation of the calculation results, while also ensuring, that complicated assumptions about the specimen shape are being avoided. The main goal of the FDTD calculations is to understand the development of the experimentally observed PL behavior as a function of the depth of analysis d, by comparing the absorption weighted yields obtained for different modulations of optical properties (Section 2.3.3) to the experimentally obtained PL intensity. The aim is to find the best match between calculation and experiment and not to find an optimized fit.

3.2.2.3 Comparison between experiment and calculation

Here we discuss to which extent the simulation model accounts for the main features of the behavior of the recorded intensity of the QW PL emission from the evaporating field emission tip. One of the main features of the experimental data, is that the QW intensity already starts diminishing before the PL-emitting QW#1 itself starts evaporating. Secondly the PL emitted by QW#1 shows a rise the evaporation stages $d > 60$ nm. The following discussion focuses on the question, to which extent the simulation, along with the different assumptions on the sample surface, can reproduce these main experimental

features.

For the Non-Degenerate Surface simulations, the premature decline before the field evaporation of QW#1 cannot be observed in the data for the absorption weighted yields (Fig. 3.8-(a)). While the normalized absorption stays mostly constant until the QW#1 itself starts evaporating for this set of simulations (Fig. 3.7-(a)), the x and z-dipoles' yield doesn't show the experimentally observed early rise in the PL emitted by the QW (Fig. 3.7-(b, d)). The y-oriented dipole on the other hand shows an early rise (+30%) in its yield (Fig. 3.7-(c)), thus giving the best (qualitative) description of all three dipole orientation for the Non-Degenerate Surface simulations.

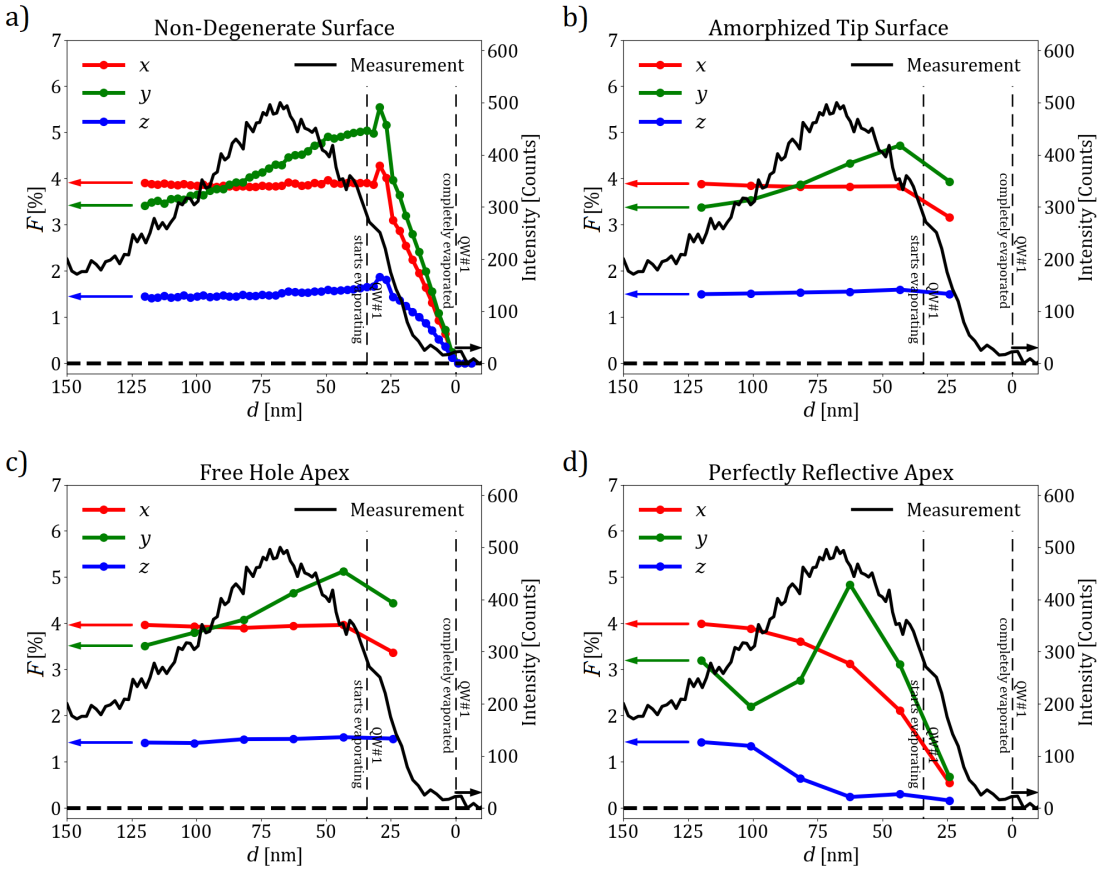

Figure 3.8: Comparison between the measured QW's PL signal and the absorption weighted yields (F[%]), which were simulated for three different dipole orientations. The absorption weighted yields are being compared for simulations of the different properties of the tip. a) Non-Degenerate Surface, b) FIB-amorphized surface, c) Free Hole Apex, d) Perfectly Reflective Apex. (Weikum et al. (2023))

The fact that this simulated dipole orientation best describes the experimental results is supported by the results of Section 3.1, which shows that y-oriented dipole emitters are the dominant source of the QW's PL signal (Fig. 3.5-(d)). While the early increase of the PL has a qualitative representation by the y-oriented dipole in the Non-Degenerate Surface simulations, the premature decline of the PL signal emitted from QW#1 cannot be explained by these simulations.

The simulations performed under the assumption of an Amorphous Tip Surface show a behavior which is very similar to the Non-Degenerate Surface case. Neither in the absorption behavior, nor in the yield behavior of any of the three dipole orientations (Fig. 3.7) there is any significant change when the amorphized tip surface in being introduced. Thus the resulting absorption weighted yields (Fig. 3.8) are virtually the same as well. The introduction of a thin amorphous layer at the specimen surface, which describes its amorphization due to the FIB preparation has been shown to be insignificant to its PL intensity emission behavior. Thus such a surface layer doesn't have to be considered when trying to describe the experimental PL behavior of a localized QW.

The simulations based on the Free Hole Apex only show minor modifications of the absorption and yield behavior (Fig. 3.7). Only for the yield of the x-oriented dipole there is a slight deviation from the Non-Degenerate surface case ($\approx 3\%$ increase). It can be stated, that the perspective that the optical modulations of free holes accumulating close to the tip apex (and the geometric evolution of this region during the tip's field evaporation) give an explanation of the experimentally observed PL behavior is false, since the effect of such a free carrier accumulation neither significantly changes the specimen's absorption nor its yield behavior. For this simulation, the charge carrier density p has been underestimated by about an order of magnitude, when compared to theoretical estimates presented in Silaeva et al. (2014). Since the modulation of the dielectric function, due to free carriers is proportional to the free carrier's density (see: Eq. 2.12), the actual modulations of the specimen optical properties can be expected to be even less significant, than in the presented calculation.

Asides from charge carrier accumulation close to the specimen apex, the effect of band-gap-shrinkage (Silaeva et al. (2014)) also has the potential to modulate the optical properties of the tip's region which is close to the apex. Also the holes, which are located close to the specimen apex can be considered to be bound to the tip's surface. This bonding of the charge carriers to the specimen apex can result in additional resonances being introduced into the system, when compared to the Non-Degenerate Surface case. Both these modulations of the apex's optical properties (band-gap shrinkage and surface-bound electron resonances) result in an increased absorption coefficient of the

electrostatically modulated apex region.

The simulations representing the Perfectly Reflective Apex indicate a drastic increase of the absorption coefficient close to the tip apex. In Fig. 3.7-(a), the Perfectly Reflective Apex simulation shows a prematurely decreasing amount of absorbed power. This is in stark contrast to the absorption behavior of the other simulations (Non-Degenerate Surface, Amorphized Tip Surface, Free Holes Apex), which don't show any decrease before the QW#1 itself start evaporating. While the yield of the x-oriented dipole shows no major change when compared to the Non-Degenerate Surface case, the y and z-oriented yields show deviations from this case (Fig. 3.7). The y-oriented Perfectly Reflective Apex simulation results in the absorption weighted yield, which best describes the QW's general behavior of the measured PL emission (Fig. 3.8-(d)). Since the main source of PL signal has been shown to be y-oriented (Section 3.1), this result is in agreement with experimental polarisation studies. Both features, namely the rise in the QW's PL in early evaporation stages ($d > 60$ nm) and its decline before QW#1 has been completely evaporated, are represented in the development of the simulated absorption weighted yield of the experimentally dominant y-dipole emission.

3.2.3 Conclusion about the detected Intensity data

FDTD simulations on the laser-absorption and emission properties were performed in order to explain the behavior of the Photoluminescence intensity, emitted from a Quantum Well inside of an La-APT needle-shaped specimen as a function of the progressing field evaporation of the specimen. These simulations were performed on a series of specimen geometries, which represents their development during the specimen's field evaporation.

By comparing experimental PAP-data with simulations of the specimen absorption and emission behavior, we are able to qualitatively explain the modulation in the PL signal produced by a nanoscale emitter localized within an evaporating field emission tip. FDTD simulations for different optical modulations of the tip, like the surface amorphization caused by the FIB milling during the sample preparation, the accumulation of free holes close to the tip apex, and a hypothetical perfectly reflective tip apex were also performed. It has been shown, that the consideration of a perfectly reflective tip apex gives a fair quantitative agreement between simulated and experimental data. This results suggests that there are strong resonances between light and the surface bound electrons to be expected in the specimen's high electric field region.

These results represent a first quantitative attempt to reproduce the effect of morphological and structural modifications on the far field emission pattern of a nanoscale

emitter localized within a field emission specimen. The applied methods are per se adapted to the particular domain of Atom Probe Tomography, however they could be easily adapted to broader domains in which nanoscale objects capable of light emission undergo morphology changes or strong interaction with static or propagating electric fields.

4. Correlative PAP Analysis of a (In,Ga)N Laser Diode

While the previous chapter exemplified gainful insights into technique of the PAP by the investigation of relatively simple quantum system, the atom probe's chemical resolution on an atomic level is able to resolve much more complex nano-structures. One example of such a specimen is described in Section 2.1.2. The results of the PAP investigation of this specimen (performed by Abraham Neftali Diaz) are presented in this chapter. For the typical distances between the layers of this specimen an isolated PL analysis of such a specimen would not allow for an easy distinction between the different PL signals. The PAP promises to obtain a picture, which allows to assign the energetic components of the recorded PL spectra to different specimen regions, which facilitates a physical explanation of the observed PL emission.

What makes this specimen a more interesting choice (from a material science perspective) is the complexity of the expected PL signal. Treating a system where optical transition energy is varied by as many factors (doping, alloying, field induced stresses) would pose a challenge for classical PL experiments, since the different phenomena and their influence on the PL signal are difficult to differentiate. The successive field evaporation of the PAP specimen allows for the discrimination of the different phenomena by correlating their presence in the detected PL signal with the progress of the specimen's field evaporation.

The PAP technique's opportunity to record PL spectra of a field evaporating specimen allows to exclude specific contributions to the overal PL by destroying their photoemission centers. The assignment of an energetically distinct PL signal to a structural region of the specimen becomes possible.

This chapter is set up in a way, which takes into account the diverse nature of the physical effects affecting the optical transition energy of the different structural regions of the specimen. After a description of the experimental results obtained by the PAP,

the main factors which modulate the system's optical transition energies are discussed.

4.1 Experimental Details on the Laser Diode PAP study

Fig. 2.11 shows the layer structure of the studied (Al,In,Ga)N specimen. The variation of the doping element (Mg, Si, Ge) as well as of the alloying element (Al, In) concentration are both possible sources of PL emission. The tip-shaped specimen is lifted out from the specimen and then milled utilizing a focussed ion beam (FIB) microscope. The resulting specimen shape is sketched in Fig. 2.11. This procedure is performed using a ZEISS Nvision40, where the lifted-out specimen is mounted onto an electro-polished tungsten post. The produced PAP-specimen is sketched in Fig. 4.1.

The PAP experiment was performed using a laser wavelength of 266 nm. The laser repetition rate was 400 kHz and the time average of the pulsed laser power was 200 μW. During the evaporation of the specimen the applied voltage rose from 3 kV to 9.4 kV. For the PL detection set-up the grating with 600 lines/nm was used and the CCD accquisition time was chosen to be 60 s.

Fig. 4.1a shows the variation of the alloying elements' (In, Al) fraction of the occupied III-sites. The Tunnel Junction (TJ) and laser diode (LD) sections are located within In doped regions in order to reduce the local band gap there and to confine free charge carriers to these regions. The Al-doped top covering of the sample introduces a low refractive index material into the system, which causes the optical modes to be pushed towards the optically active LD region.

Fig. 4.1b shows the different dopant (Mg, Si, Ge) levels which are present in the different layers of the specimen. The TJ represents a p-n-junction and serves to introduce free holes from the substrate into the optically active region. The LD itself is located at the intrinsically doped center of a p-i-n-junction.

Table 4.1: The APT parameters utilized for the reconstruction of the (In,Ga)N-LD specimen.

Parameter	Value
Projection Point (M+1)	1.65
$E\beta$-factor $[\frac{\mathrm{V}}{\mathrm{nm}}]$	7.30
Curvature-factor	1
Detection Efficiency	50%

4.1.1 Specimen Reconstruction Parameters

The full dataset of the PAP experiment consist of the APT and the PL data. The APT reconstruction was performed using the GPM3D-soft's Standard Ebeta algorithm. The utilized reconstruction parameters are shown in Table 4.1. In order to take the Nitrogen-losses (Russo et al. (2018)) of the GaN-system's APT analysis into account for the reconstruction of the specimen, only the atoms occupying the III-sites (Ga, Al, In, Si, Ge, Mg) are considered to have a volume contribution to the reconstruction algorithm. Each of these atoms is assigned with the reconstruction volume of the primitive unit cell of the base material (GaN). This approach to reconstruction assumes that the specimen's Ga-site elements are detected with the full detection efficiency of the system (50% Table 4.1). N-atoms are considered to experience loss effects which reduce their effective detection efficiency, but since the entire primitive unit cell's volume is assigned to the III-site atoms, these losses do not affect the depth which is gained with every evaporated atom (dz, see Section 1.2.1.3).

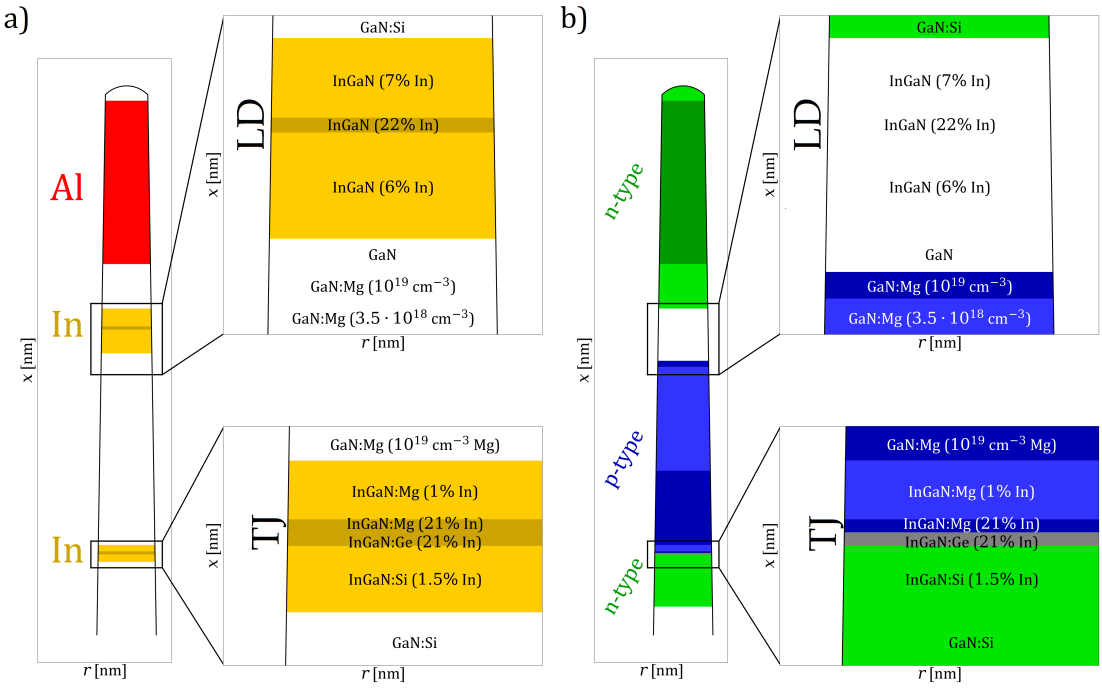

Figure 4.1: Schematic of the FIB-milled specimen, decomposed into its alloying (a) and doping (b) properties.

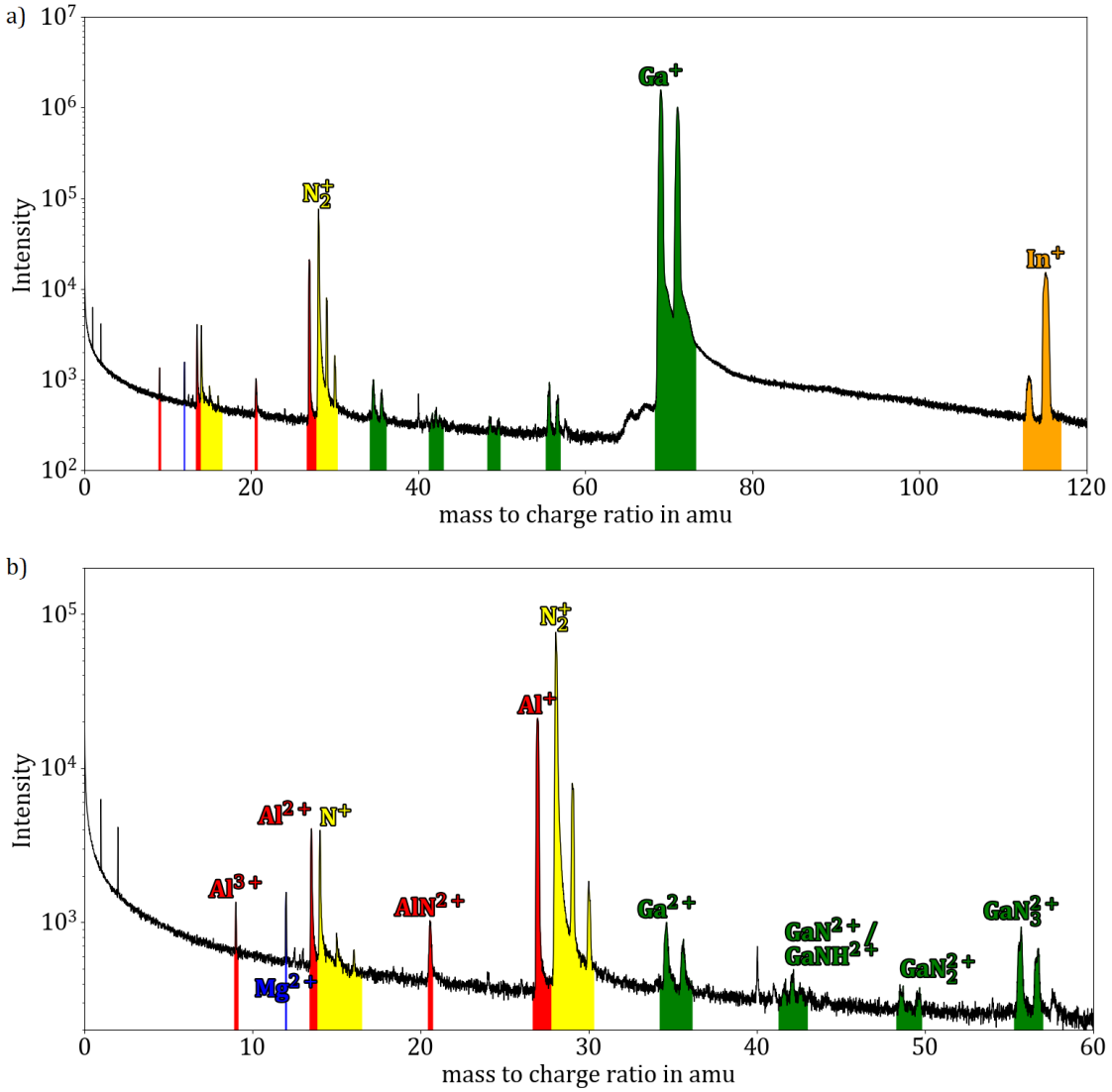

Figure 4.2: a) Total specimen mass spectrum with identified peaks. b) Zoom into the mass spectrum showing the species with a mass-to-charge ratio below 60 amu. The mass windows which are used for the atom identification of the APT reconstruction are color coded.

4.1.2 Mass spectrum analysis

Fig. 4.2 shows the mass spectrum recorded during the performance of the in-operando PAP experiment. The mass windows which define the identified species that constitute the specimen are shown in color code. Table 4.2 shows the isotopic abundances of the elements contained in the specimen. In the full mass spectrum (Fig. 4.2a) main species

evaporated during the PAP experiment (Al^+, N_2^+, Ga^+, In^+) can be easily seen. In the zoomed-in mass spectrum (Fig. 4.2b) the less abundant species can be observed as well. By fitting the mass spectrum for specific ranges of the mass to charged ratio using a sum of Gaussians with a fixed standard deviation for every isotope (σ):

$$I(m) \approx \sum_i a_i \cdot \exp\left(-\frac{(m-m_i)^2}{2\sigma_i^2}\right) + K \tag{4.1}$$

the isotopic abundances of the atomic species can be calculated. a_i are a measure of the isotpoes peak intenstiy and K describes the background signal which is uncorrelated to the laser pulse in the proximity of the peak's mass to chage ratio. m_i is the mass to charge ratio of the isotope i. The elements identified in the mass spectrum (Fig. 4.2) are Al, Mg, N, Ga, In. Since Al only occurs naturally as a single isotope (^{27}Al) we have to rely only on the mass to charge ratio to identify Al peaks. For the other elements however we are able to confirm the chemical nature of the peaks by comparing the experimentally observed isotopic abundances with the literature values shown in Table 4.2. The mass spectra of the most intensive Ga, In and Mg species are shown in Fig. 4.3. From the fits performed on these peaks the experimentally obtained isotopic abundances shown in Table 4.2 are obtained. The doping element Ge only represents such a small fraction of the total

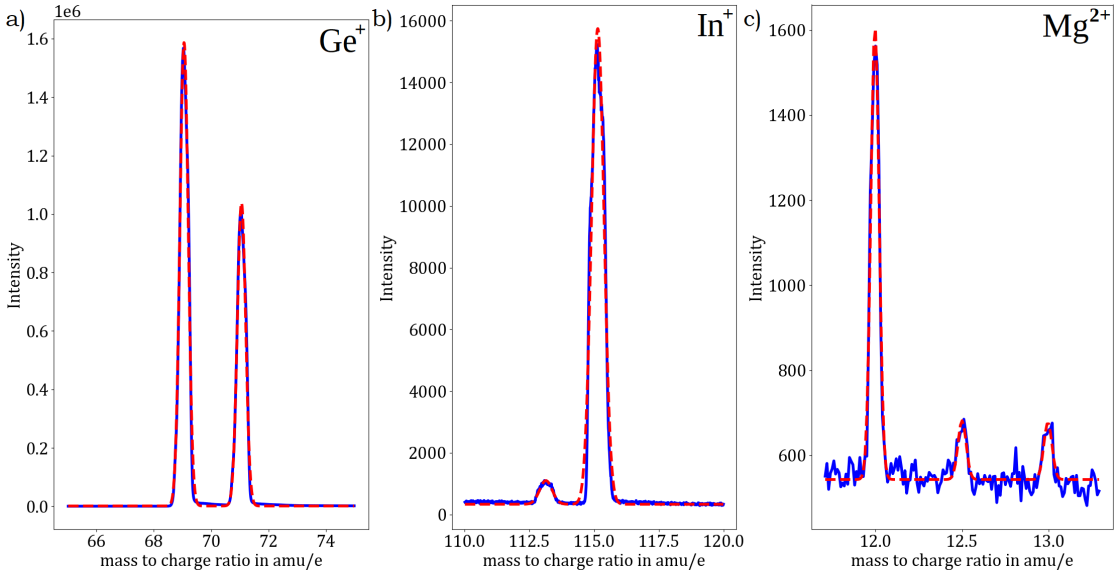

Figure 4.3: Mass spectra of the most intensive peaks of the species which can be identified from their mass to charge ratios. From the Gaussian fits (red, Eq. (4.1)) the isotopic abundances of Ga (a), In(b) and Mg (c) are calculated.

Table 4.2: The isotopic abundances of the elements composing the (In,Ga)N heterostructure. (NIST (2023)) and the abundances obtained by the PAP experiment.

Si	Lit.	**Ge**	Lit.	**Al**	Lit.	**N**	Lit.
^{28}Si	92.2 %	^{70}Ge	20.6 %	^{27}Al	100.0 %	^{14}N	99.6 %
^{29}Si	4.7 %	^{72}Ge	27.5 %			^{15}N	0.4 %
^{30}Si	3.1 %	^{73}Ge	7.8 %				
		^{74}Ge	36.5 %				
		^{76}Ge	7.7 %				

Ga	Lit.	Exp.	**In**	Lit.	Exp.	**Mg**	Lit.	Exp.
^{69}Ga	60.1 %	60.5 %	^{113}In	4.3 %	4.7 %	^{24}Mg	79.0 %	79.7 %
^{71}Ga	39.9 %	39.5 %	^{115}In	95.7 %	95.3 %	^{25}Mg	10.0 %	10.3 %
						^{26}Mg	11.0 %	10.0 %

number of detected atoms that its peaks are not visible in the total mass spectrum due to noise. The Si^{2+} and Si^{+}-peaks on the other hand share their mass-to-charge ratios with the N^{+} and N_2^{+} peaks which are of such a high intensity that the Si doping cannot be quantified anywhere within the specimen. Thus their isotopic abundance cannot be determined in the same way as for Ga, In and Mg. The strong N-signals on the other hand would be able to allow for a calculation of its isotopic abundance. Applying the treatment as shown in Fig. 4.3 to the N^{+}-signal however yields that the relative intensity of the $^{15}N^{+}$ peak to be 7.4 %, which is a value far removed from the literature value of 0.4 %. Since there also is a peak at 16 amu present in the measurement the overrepresentation of the 15 amu signal is assigned to the field evaporation of NH^{+}.

In Fig. 4.2b hydrogen (H^{+} and H^{2+}) can be observed at 1 amu and 2 amu. Also hydrogen replica (NH^{+} and NH_2^{+}) of the N^{+} and the N_2^{+} signal (N_2H^{+} and $N_2H_2^{+}$) signal can be seen at 15 amu/16 amu and 29 amu/30 amu respectively. An issue concerning the detection of hydrogen during an APT experiment is that it cannot clearly be distinguished if the detected hydrogen originates from the actual composition of the specimen or from contamination of the UHV chamber (Rigutti et al. (2021), Yoo et al. (2022)). Due to this circumstance there are no mass windows assigned to the hydrogen containing species investigated in the APT analysis. While the Mg^{2+} signal of the specimen show peaks for all three Mg isotopes (at 12 amu, 12.5 amu, 13 amu) only the peak of the isotope with the highest abundance ($^{24}Mg^{2+}$, 79.0%) is taken into consideration for the APT analysis. This was performed in order to improve the signal to noise ratio. In the following investigations of the specimen's Mg concentration this choice of mass window is taken into account by multiplying the Mg^{2+}-content measured under the exclusion of the $^{25}Mg^{2+}$ and $^{26}Mg^{2+}$ signals by $\frac{1}{79.0\%}$. A very minor Mg^{+} signal can also be found at

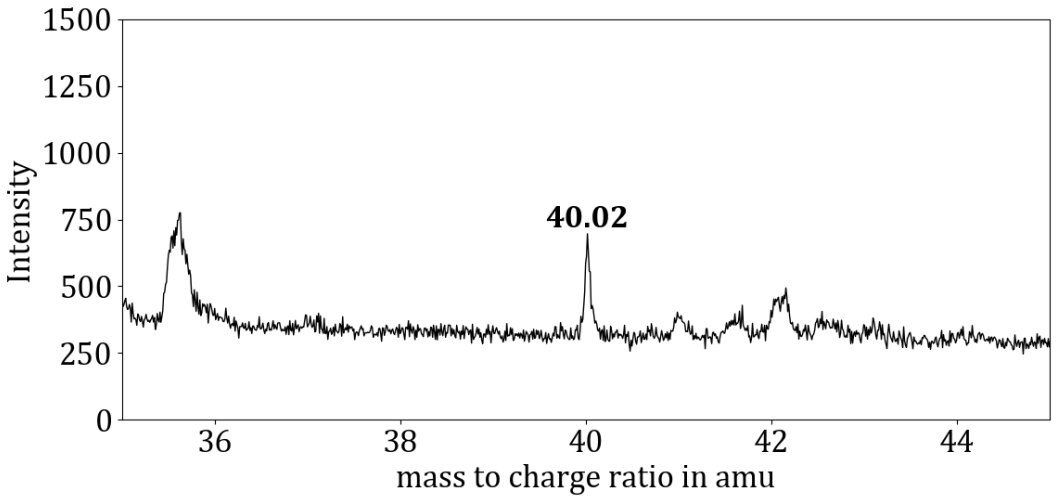

Figure 4.4: The unidentified peak at 40 amu and its surroundings in the mass spectrum.

24 amu. In order to improve the signal to noise ratio of the evaluation, this signal which barely exceeds the noise background is not taken into account for the evaluation of the APT data. Since the Al-containing species in Fig. 4.2b (Al^{3+}, Al^{2+}, Al^{+}, AlN^{2+}) only occur in the Al-rich region which is evaporated at the beginning of the experiment, these signals can be clearly identified to be Al-based. Also several molecular species containing Ga (GaN^{2+}/$GaNH^{2+}$, GaN_2^{2+}, GaN_3^{2+}) are identified.

One peak that remains ambiguous despite our analytical efforts is the signal at 40 amu (Fig. 4.4). This signal can be observed in the space between the lower edge of the Al-rich capping layer and the upper edge of the TJ's cladding layers (InGaN:Mg (1 % In)). There it appears in the Si-doped layers betwen the LD and the Al-rich region, in the LD itself and in the Mg-doped region between LD and TJ. This peak's presence is independent on the presence of Mg, Si and In in the selected region. Thus it is most likely that this peak comes from the elements which are inherent to the specimen (Ga, N). However the isotopic abundances (Table 4.2) suggest that a signal containing Ga would have at least two different isotopes. From the local mass spectra of specific tip sections it is clear, that the 40 amu peak does not have any neighboring peaks coming from different isotopes. This is known because there are sections of the specimen where the three minor signals following the 40 amu peak (41 amu, 41.6 amu and 42 amu) are not present.

4.1.3 Correlation Data on the (In,Ga)N-heterostructure

An overview of the PAP in-operando experiment's results can be seen in Fig. 4.5. Fig. 4.5a) shows the positions of the atoms which are located on a thin 2 nm slice round the tip center. Since a very high number of atoms (107 million) were evaporated during the PAP experiment, the total depth of analyis (1.9 μm) is much larger than the atomic coordinates perpendicular to this axis (30 nm). In order to better visualize the result of the reconstruction, the aspect ratio in Fig. 4.5a) is not 1:1.

From the reconstruction data of the specimen (and not only of the thin slice) concentration profiles were generated. Fig. 4.5b) (In) and Fig. 4.5c) (Mg) show the most interesting correlation with the recorded PL specta. These concentration profiles are however not created by utilizing bins which contain the detection atoms within certain z intervals of constant size as usual for APT data visualization. Instead every evaporated atom is assigned to the bin of the PL spectrum (i) which is recorded during its field evaporation. This bin is then assigned to a depth of analysis value (d_i) which is calculated as the mean of the lowest and highest d-values of the atoms inside of it. While In is sufficiently abundant in every bin, the Mg concentration is much lower. In order to better interpret the Mg-concentration in the composition profile graphs, the Mg concentration profile is smoothed using Gaussian weights (with σ =5 nm):

$$c_{\mathrm{smooth}}(\mathrm{Mg})(d) = \frac{\sum_{i=0}^{i_{\max}} c(\mathrm{Mg})(d_i) \cdot \exp\left(-\frac{1}{2}\left(\frac{d-d_i}{\sigma}\right)^2\right)}{\sum_{i=0}^{i_{\max}} \exp\left(-\frac{1}{2}\left(\frac{d-d_i}{\sigma}\right)^2\right)} \tag{4.2}$$

This assignment of every evaporated atom to a PL spectrum allows for a straightforward comparison between the composition profiles and the specimen's PL response. Fig. 4.5d) shows the PL spectra recorded during the specimen's field evaporation as heat maps. The red zones of this graph show a high detected PL intensity and the blue regions show a low intensity of PL.

Finally two more parameters which contain crucial information of the APT analysis are shown in Fig. 4.5e) and Fig. 4.5f). The voltage applied to the specimen is a measure of the facility of the specimen's field evaporation. The voltage is chosen so that the desired detection rate of atoms is maintained as constant throughout the entire measurement. For a constant radius of curvature a high applied voltage corresponds to a surface of the specimen which is resistant to field evaporation, while a low applied voltage indicates that the section of the tip evaporates easily. Similarly the ratio of the charge states of a select

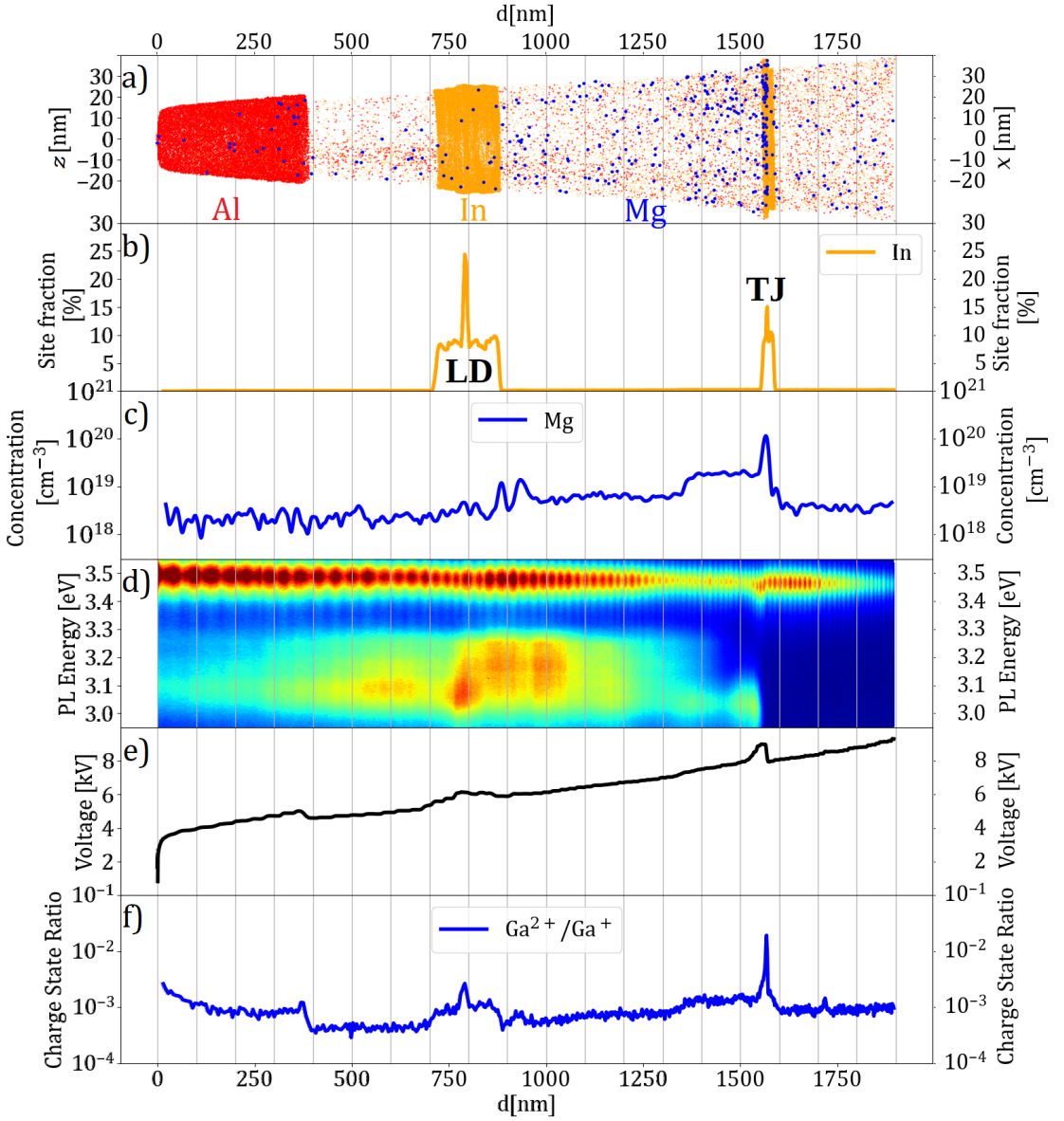

Figure 4.5: The experimental results of the correlated PAP analysis of the (In,Ga)N specimen. a) The APT reconstruction of the sample. b) The In concentration profile. c) The Mg concentration profile. d) Color coded heatmap of the PL spectra recorded during the specimen's field evaporation. e) The development of the voltage during the PAP experiment. f) Ga-charge state ratio.

species category (e.g. Ga^{2+}/Ga^{+} as shown in our analysis) allows for the estimation of the electric field present at the tip apex. Since the theory of thermal field evaporation (Section 1.2.1.1) suggests that only single charge atoms are emitted from the specimen, an ion's transition into a higher charge state takes place by electrons tunneling from emitted ions into the positively charge specimen. Since a higher electric field facilitates this tunneling process (Kingham (1982)), the charge-state ratio can be used as a measure of the electric field.

4.2 Compositional Analysis

4.2.1 Mg-doping

Magnesium is a major dopant of the (In,Ga)N LD heterostructure (Fig. 4.1). Between the LD and the TJ a region with relatively low Mg doping content ($3.5 \cdot 10^{18}$ cm^{-3}) and a highly Mg doped (10^{19} cm^{-3}) region were grown (Fig. 2.11). This difference of the Mg doping levels can be seen in Fig. 4.5c), where the low Mg content zone can be found in the region 1000 nm $< d <$ 1300 nm and the high Mg content zone in 1400 nm $< d <$ 1500 nm. The Mg content in the concentration profile is smoothed with $\sigma = 5$ nm according to Eq. (4.2).

In order to quantify the dopant concentration present in these two regions their local mass spectra are investigated. By generating the mass spectra of selected regions (Fig. 4.6) in the centers of these two differently doped parts of the specimen the calculated

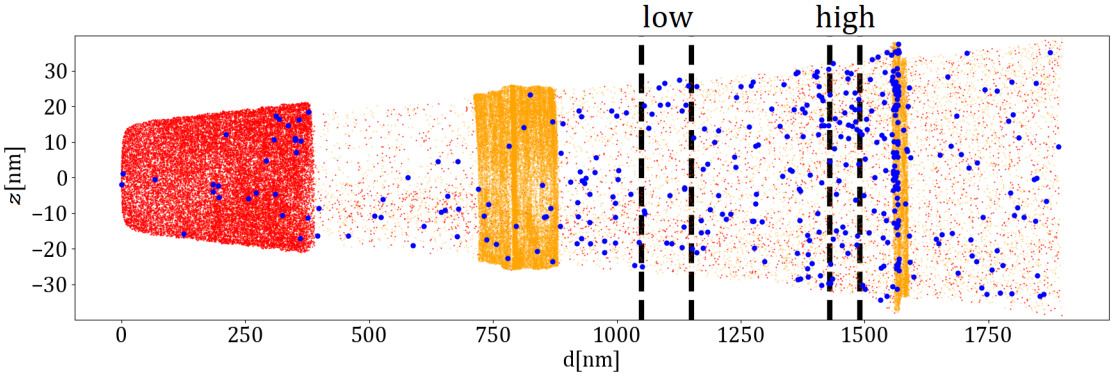

Figure 4.6: The selected regions within the low and high Mg concentration zones between the LD and the TJ. With the atoms present in these regions the local mass spectra are calculated. The atoms shown in this figure lie within a slice of 2 nm thickness around the specimen center. The local mass spectra (Fig. 4.7) are generated from the entire thickness of the reconstruction.

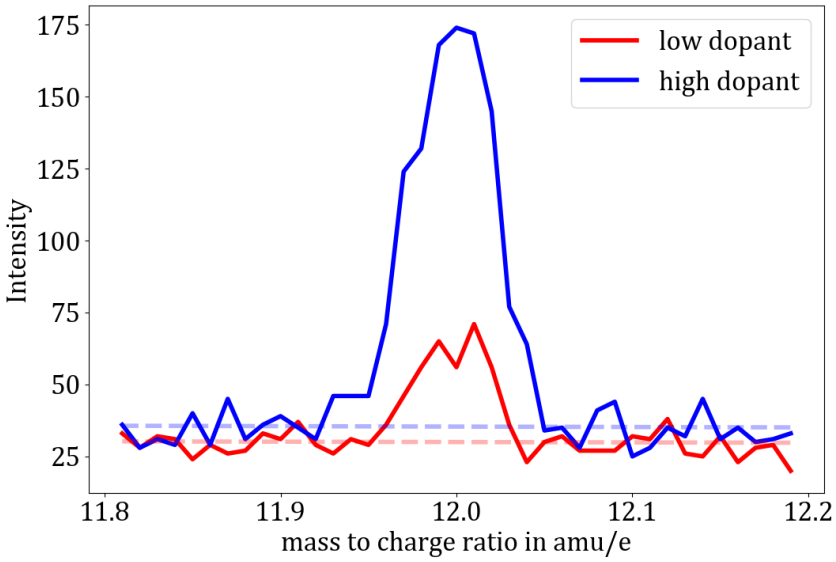

Figure 4.7: The local mass spectra of the regions shown in Fig. 4.6.

concentrations can be background corrected. The total number of detection events are 5.6 million for the low dopant concentration region and 5.1 million for the high dopant concentration region.

Fig. 4.7 shows the mass spectra of these regions. Since the calculation of the Mg-dopant concentration is the focus of the selection of the local mass spectra only the signal of the most abundant Mg isotope ($^{24}Mg^{2+}$) is shown. While the other isotopes are also present, their signals only barely exceed the noise level and thus are not useful for the calculation of the dopant concentration. The experimental background, which corresponds to evaporation events that are uncorrelated with the mass of the Mg^{2+}-peak, is fitted and shown as dashed lines. By summing up the difference between the measured intensity and the fitted background for every mass to charge ratio of the histogram the background number of detected Mg atoms is calculated.

Since the background is estimated by performing a fit for a variety of different mass to charge ratio ranges, the fits represent the main source of error when calculating the background corrected intensity of the $^{24}Mg^{2+}$ signal. The background correction has been shown to give a good description of the experimental noise if it is shifted by ± 2 on the intensity scale. With a total number of 40 mass to charge ratio bins (with a spacing of 0.01 amu) a total error of ± 80 detected Mg atoms is estimated for both regions.

The total number of Mg^{2+} ions is calculated by dividing the number of detected $^{24}Mg^{2+}$ ions by it isotopic abundance (79.0 %). Since the Ga^{+} peak is the by far most

Table 4.3: The APT parameters utilized for the reconstruction of the InGaN-TJ specimen.

	low Mg	high Mg
$N(Ga^+)$	5.21 million	4.56 million
$N(^{24}Mg^{2+})$	148	803
c(Mg)	$3.6 \cdot 10^{-5}$	$22.3 \cdot 10^{-5}$
Δc(Mg)	$1.6 \cdot 10^{-5}$	$1.8 \cdot 10^{-5}$
p(Mg) [cm^{-3}]	$1.6 \cdot 10^{18}$	$9.8 \cdot 10^{18}$
Δp(Mg) [cm^{-3}]	$0.8 \cdot 10^{18}$	$0.7 \cdot 10^{18}$

significant peak of any Gallium containing species dividing the number of the Mg^{2+} ions by the number of detected Ga^{2+} ions gives the site fraction of the Mg atoms (c(Mg)). By dividing the Mg site fraction by the volume of the GaN unit cell (22.8 Å^3) the Mg doping concentration p(Mg) is calculated.

Table 4.3 shows the values of these quantities. As seen in this table, the compositional analysis of the APT data gives a good reproduction of the expected dopant concentration (10^{19} cm^{-3}) within the highly Mg doped region. In the low Mg dopant region however the compositional analysis deviates from the dopant concentration expected from the growth conditions ($3.5 \cdot 10^{18}$ cm^{-3}).

4.2.2 In-content

Since the indium content of the specimen is well above the mass spectrum's noise level, the analysis of the In content does not require a detailed background subtraction as performed in Section 4.2.1. Instead every detection event with a mass-to-charge ratio that falls into the In^+ mass window (Fig. 4.2a) is considered to be an indium atom. Since both nanostructures (LD and TJ) which are interesting for the functionallity of the specimen contain a significant amount of In, the In site fraction at the proximity of both these structures is shown in (Fig. 4.5a). By visualizing the In-site fraction (Fig. 4.5b) we are able to have a good orientation when navigating through the PAP data (Fig. 4.5).

The In concentration profiles of both the LD and TJ are shown in Fig. 4.8. By fitting the In site fraction in the plateau region of both these zones the In-content of the cladding layers is calculated. The maximum value of the In content gives the measured In site fraction in the center of both nanostructures (Table 4.4).

The composition dependence of the InGaN band gap can be expressed as a function

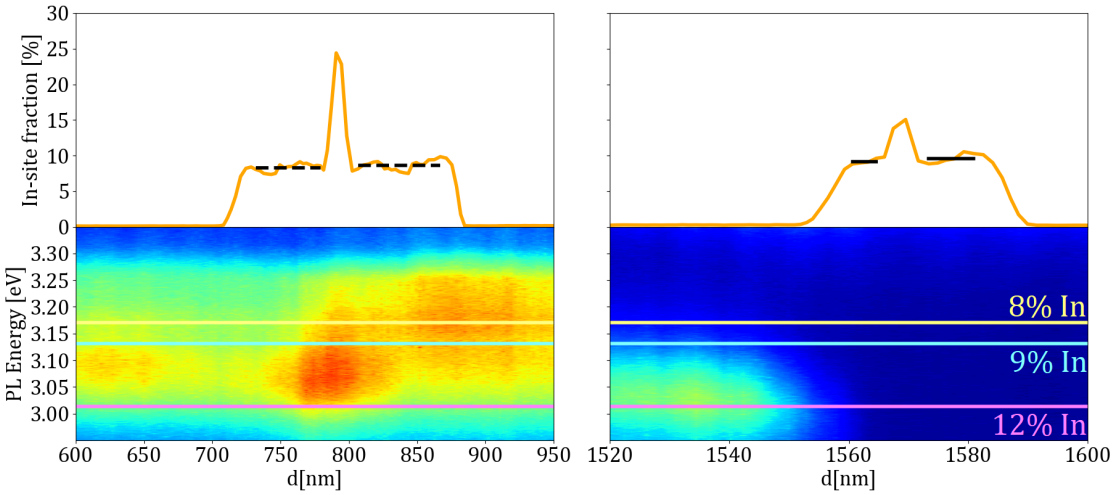

Figure 4.8: The LD's (left) and TJ's (right) In composition profile as a function of the depth-of-analysis d. Different evaporation states (characterized by d) of the specimen show a varying level of distinguishable PL signals. The expected NBE emission energies of (In,Ga)N with different In-site fractions serve as an orientation for the estimation of the In-content which is required to generate the observed PL response.

of the III-site fraction of In (x):

$$E_g(\mathrm{In}_x\mathrm{Ga}_{1-x}\mathrm{N}) = x \cdot E_g(\mathrm{InN}) + (1-x) \cdot E_g(\mathrm{GaN}) + x \cdot (1-x) \cdot \kappa \tag{4.3}$$

where E_g(InN) is the band gap energy of InN, E_g(GaN) is the band gap energy of GaN and κ is the InGaN system's bowing parameter. While E_g(GaN) can be easily estimated (E_g(GaN) $\approx$ 3.5 eV) from the Near Band Edge (NBE) signal, the other parameters E_g(InN) = 0.70 eV and κ = 1.43 eV have to be obtained from literature (Wang and Yoshikawa (2004)). The PL signal of the specimen when both nanostructures in the process of field evaporating is also shown in Fig. 4.8. In this figure the PL energy of bulk

Table 4.4: The In site fraction (x) inside the different specimen regions as estimated from their growth conditions and as measured using the PAP. The expected band gap energy of such a compound is calculated via Eq. (4.3).

	Expected		Measured	
Layer	x [%]	E_g [eV]	x [%]	E_g [eV]
LD Cladding	6-7	3.25-3.21	8	3.2
LD Center	22	2.64	22	2.6
TJ Cladding	1-1.5	3.46-3.44	9	3.1
TJ Center	21	2.67	15	2.9

(In,Ga)N with different In site fractions (8 % In, 9 % In and 12 %) is shown as horizontal lines as an overlay of the PL spectrum.

4.2.3 Ge-doping

Germanium is used as the n-type dopant within the TJ (Fig. 2.11). This thin layer is surrounded by Mg-doped (In,Ga)N on the p-type side and by Si-doped (In,Ga)N as a cladding layer on the n-type side. This configuration allows for the quantification of the Ge doping level within the extremely thin (In,Ga)N:Ge layer. An issue with the quantification of the Ge doping within the specimen is its overlap with Ga in the mass spectrum. This is caused by the similar masses of the abundant isotopes of both elements. No naturally abundant isotopes of Ga and Ge share the same exact mass (Table 4.2) and the most abundant Ge isotope ^{74}Ge can be clearly distinguished from the thermal tail (Vurpillot et al. (2006)) of the Ga-peaks both for the Ge^{+} and the Ge^{2+} evaporation events in the selective mass spectrum of the Ge-doped region of the specimen (Fig. 4.9).

By investigating the mass spectrum of the atoms which constitute the center of the TJ (red zone Fig. 4.9) the total number of Ge atoms in the n-type doped part of the TJ can be calculated. While the whole specimen's mass spectrum Fig. 4.2 does not allow the identification of any Ge-peak, the reduced background noise of local spectra allow for the atomic identification of locally present elements. Fig. 4.10a shows local mass spectra of the atoms which are in the proximity of the TJ (red zone). By subtracting the background

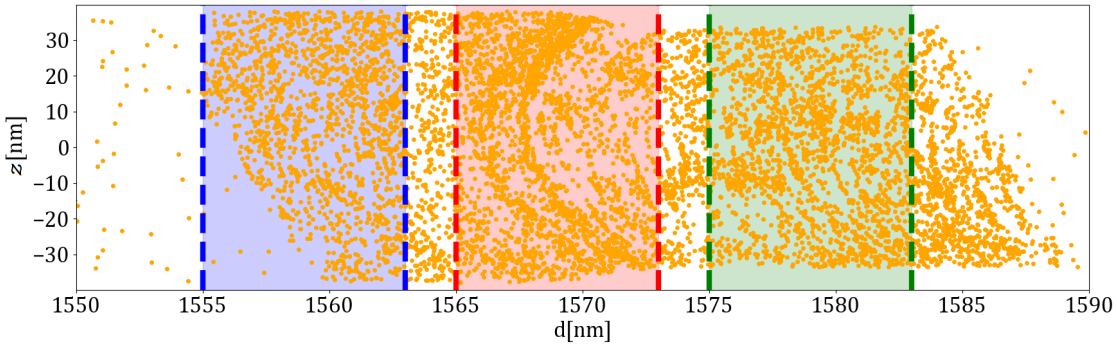

Figure 4.9: Close-up of the specimen reconstruction in the proximity of the TJ. Only the In atoms are shown here. The TJ is the region of high In-atom density within the red zone. The TJ appears to be curved in the reconstruction because the electric field experiences a sudden drop during the TJ's field evaporation (Fig. 4.5e,f). The blue and green zones are used to chemically analyse the upper and lower cladding layer. The curvature of the TJ is an artifact of the APT reconstruction and only amounts to roughly 5 nm over a span of 74 nm.

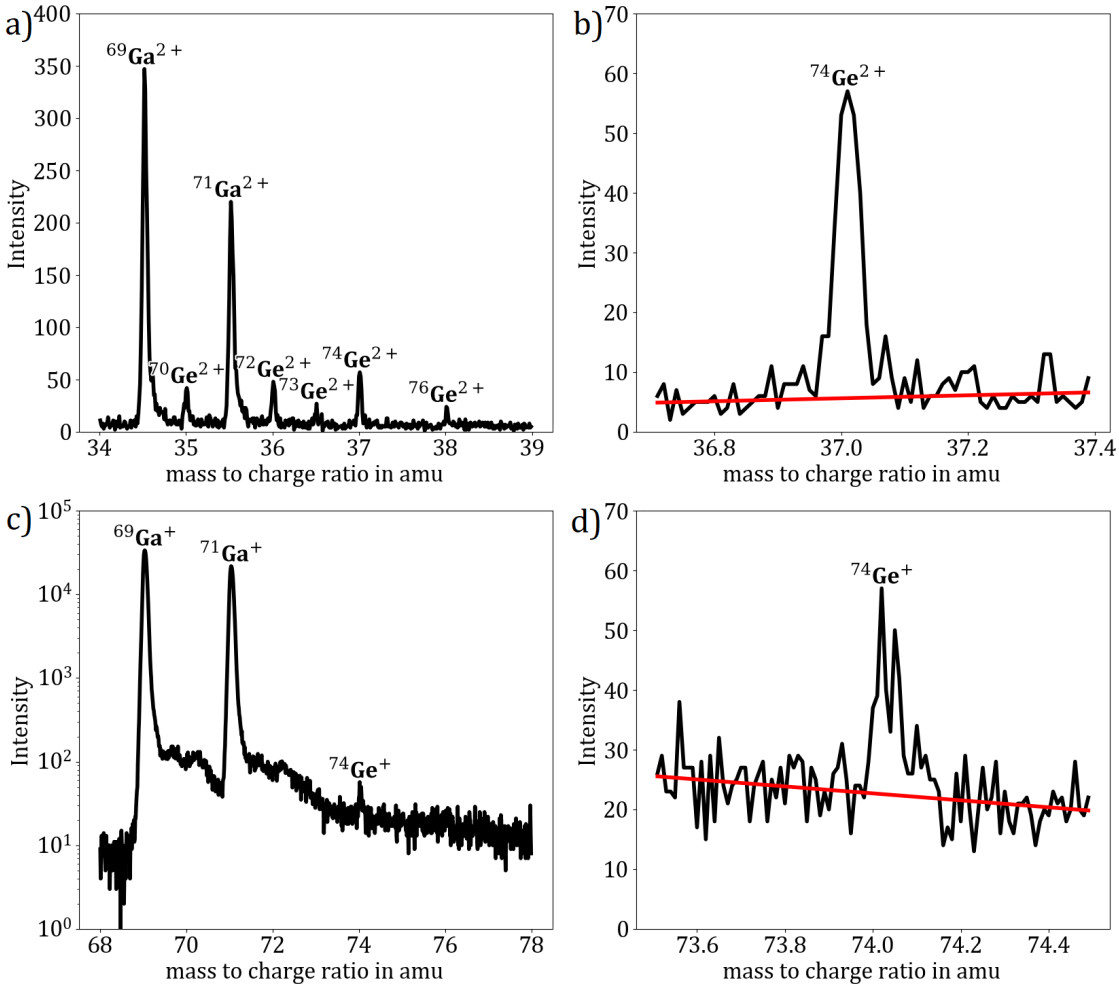

Figure 4.10: The mass spectra of the Ga/Ge^{2+} (a,b) and Ga/Ge^{+} (c,d) signals. The minor peaks in the tails of the $^{69}Ga^{+}$ and $^{71}Ga^{+}$ at 69.7, 70.2, 71.2 and 72.2 amu do not correspond to the isotopic mass of any of the abundant isotopes of either Ga or Ge (Table 4.2).

from the mass spectrum Fig. 4.10b of the $^{74}Ge^{+}$ and $^{74}Ge^{2+}$-peaks and considering the isotopic abundances of the different Ge-isotopes (Table 4.2) the total number of detected Ge-atoms (N_{Ge}) is calculated. While the Ge^{+}-peaks are mostly covered by the tails of the two Ga^{+} isotope signals (Fig. 4.10c), the $^{74}Ge^{+}$ peak can be still discerned in the mass spectrum (Fig. 4.10d).

However the APT reconstruction shows an artifact close to the center of the TJ. Due to a sudden drop in the applied voltage shortly before the evaporation of the TJ (Fig. 4.5) the reconstruction algorithm misinterprets the local radius of curvature leading

to the curved appearance of the TJ (Section 1.2.1). The curved appearance of the already thin TJ and thus the flawed reconstruction in the TJ's proximity, makes it difficult to calculate its Ge-doping concentration in the same way as already presented for Mg in Section 4.2.1.

Instead the Ge atoms are considered to be present in a section of the specimen which has the thickness ($t = 5$ nm) which is expected for the Ge-rich section of the TJ (Fig. 2.11). The radius of the reconstruction in the region of the TJ is $r = 37 \pm 2$ nm. Thus the volume of the TJ in the reconstruction is estimated as $V_{\mathrm{TJ}} = \pi \cdot t \cdot r^2$. The Ge doping concentration can be calculated as:

$$n(\mathrm{Ge}) = \frac{N_{\mathrm{Ge}}}{V_{\mathrm{TJ}} \cdot \nu} \tag{4.4}$$

where $\nu = 50\%$ is the system's detection efficiency. The error of the Ge dopant concentration is calculated as:

$$\Delta n(\mathrm{Ge}) = \left|\Delta r \frac{\mathrm{d}n}{\mathrm{d}r}\right| + \left|\Delta N \frac{\mathrm{d}n}{\mathrm{d}N}\right| = n_{\mathrm{Ge}} \cdot \left(2\frac{\Delta r}{r} + \frac{\Delta N_{\mathrm{Ge}}}{N_{\mathrm{Ge}}}\right) \tag{4.5}$$

The error in the number of detected Ge atoms is estimated by considering an error of ± 2 atoms for every bin of both mass spectra (Fig. 4.10b,d) resulting in a total error of $\Delta N_{\mathrm{Ge}} = \frac{260}{36.5\%} = 712$ atoms when taking the isotopic abundance of the other Ge isotopes into consideration. The Ge dopant concentration estimated here ($1.2 \pm 0.8 \cdot 10^{20}$ cm^{-3}, see Table 4.5) is lower than the expected concentration of $5 \cdot 10^{20}$ cm^{-3} (Fig. 2.11).

In order to verify if some Ge might have left the center of the TJ (red zone in Fig. 4.9), the local mass spectra of both cladding layers surrounding (blue zone and green zone in Fig. 4.9) are investigated. Neither in the top cladding layer (blue), nor in the bottom cladding layer (green) a $^{74}Ge^{+}$ or a $^{74}Ge^{2+}$ peak are observed. Thus we conclude that the Ge atoms, whose doping levels are undestimated in this section, in the TJ did not

Table 4.5: The number of the Ge-detection events measured in the red zone of Fig. 4.9. By estimating the volume of the Ge-doped region the doping concentration is calculated (Eq. (4.4)).

$N(^{74}Ge^{2+})$	295
$N(^{74}Ge^{+})$	191
$N(\mathrm{Ge})$	1332
$n(\mathrm{Ge})$ [cm^{-3}]	$1.2 \cdot 10^{20}$
$\Delta n(\mathrm{Ge})$ [cm^{-3}]	$0.8 \cdot 10^{20}$

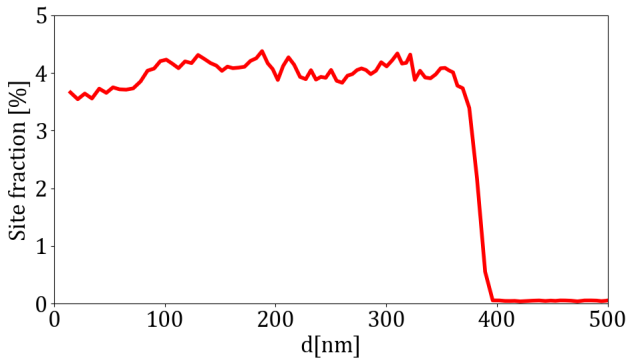

Figure 4.11: Al-fraction of the III-sites of the specimen.

migrate into either cladding layer.

4.2.4 Al and Si content

In order to confine the system's optical modes of LD-heterostructure within the optically active region it contains an (Al,Ga)N top layer (Fig. 4.5). From its growth conditions this layer is expected to have an Al content of 3 %. From the APT data an Al site-fraction of 4 % is obtained within the Al-rich layer (Fig. 4.11). The Al-composition profile is calculated from the sum of the atoms which fall into the Al mass windows (Al^{3+}, Al^{2+}, Al^{+}). Since the calculated Al-site fraction is marginal for $d > 400$ nm, no subtraction of the experimental background was performed.

The (Al,Ga)N layer is, as well as the layers below the TJ, Si doped. Quantifying the Si-content however poses a problem for the APT technique. Since the isotopic mass of the most abundant Si isotope ^{28}Si is twice the mass of the most abundant N isotope ^{14}N there are overlaps of these species in the mass spectrum. Since nitrogen evaporates as N_2^+, N_2H^+, $N_2H_2^+$ and as N^{2+}, NH^{2+}, NH_2^{2+} the quantification of the Si signal coming both from the Si^+ and the Si^{2+} detection events is obstructed for all isotopes by the thermal tails of these APT signals.

4.3 Heterostructure Investigation

4.3.1 Layer Arrangement

While the previous sections have dealt with the compositional properties of different regions of the heterostructure, their arrangement and their thicknesses are important for

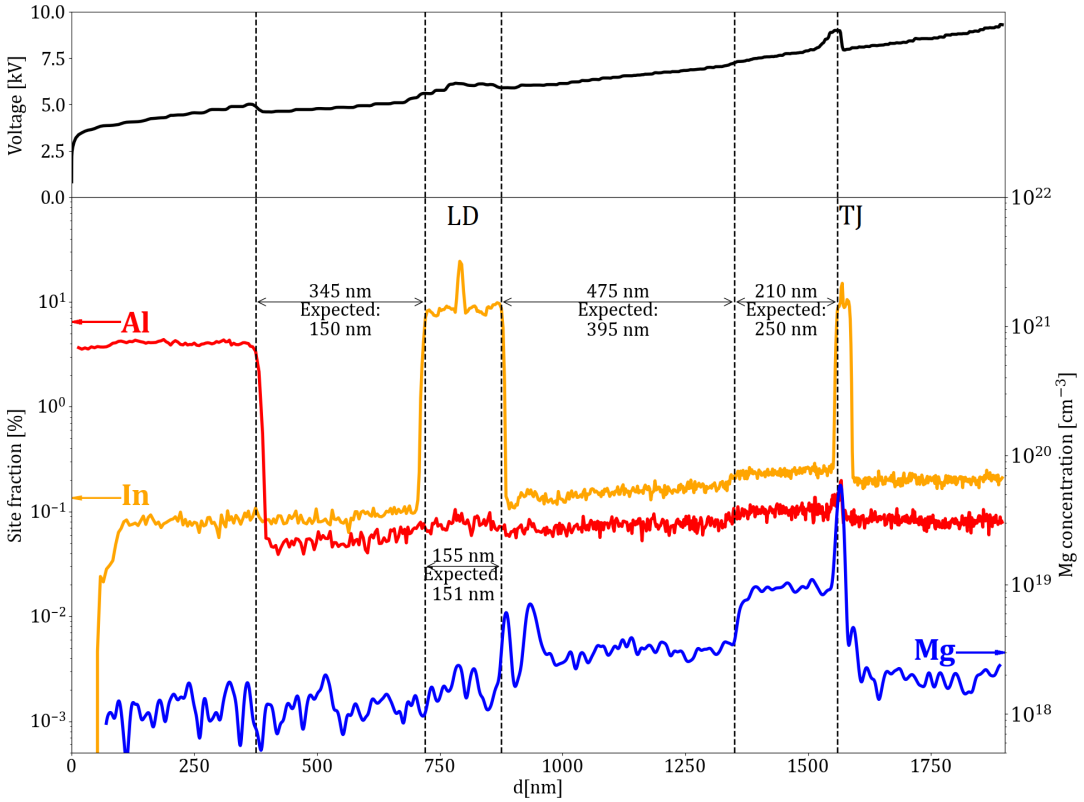

Figure 4.12: The concentration profiles of the reconstructed specimen and the development of the applied voltage. The reconstruction parameters (Table 4.1) are chosen so that the LD (including its cladding layers) is of roughly the expected thickness. The (In,Ga)N QW is located at the center of the LD region and can be identified by its elevated In III-site fraction.

the application of the LED. This section presents the thicknesses of the different layers as obtained from the APT reconstruction and compares these thicknesses with the values expected from the growing conditions (Fig. 2.11).

Fig. 4.12 shows the concentration profiles of the main species as obtained from the APT reconstruction. The APT reconstruction algorithm (Section 1.2.1.3) is used to perform this reconstruction (standard $E\beta$). The reconstruction parameters are shown in Table 4.1. While standard values which describe a usual APT specimen are chosen for the projection point, the curvature-factor and the detection efficiency, the $E\beta$-factor is chosen to be a value which gives a good reconstruction for the thickness of the LD structure and its cladding layers.

The reconstruction algorithm considers the $E\beta$-factor to be proportional to the elec-

tric field of evaporation of the specimen and to be constant throughout the entire experiment. The applied voltage is automatically controlled so that the evaporation rate is held constant. Any modification of the applied voltage is thus considered to be caused by a change in the radius of curvature by the algorithm (Eq. (1.10)). However since the studied system is a heterostructure, this assumption cannot be considered to be entirely true. Since layers with differing chemical constitution within the specimen have different heats of sublimation and work functions, they also have different values of the field evaporation activation energy (Eq. (1.11)). This results in different electric fields being necessary to evaporate these differently composed layers at the desired detection rate (Eq. (1.12)). Thus once the evaporation field reaches a region where the electric field of under which the specimen evaporates no longer corresponds to the $E\beta$-factor of the reconstruction algorithm, the radius of curvature is not properly calculated leading to artifacts in the reconstructed data.

A homogeneous specimen undergoing controlled field evaporation is expected to undergo a monotonous rise in the applied voltage in time, which corresponds to a continuous increase in the radius of curvature. Since the depth of analysis also rises with experiment time, the applied voltage also rises with depth of analysis. If the evaporation front starts entering a section of the specimen which is harder to evaporate than the previous one, the voltage experiences a more sudden rise. If the evaporating section of the specimen becomes easier to evaporate on the other hand the voltage drops. The voltage development when transitioning into In-rich portions of the specimen shown in Fig. 4.12 shows this behavior. There is no steady rise in the applied voltage found, but instead there are drops (once a layer containing Al and In has been fully evaporated) and rises (once an In-containg layer starts evaporating) which disagree with the continuous rise in voltage, which is assumed for the reconstruction algorithm. Thus it can be concluded that phases containing In and Al are harder to evaporate than pure GaN.

While the interfaces between GaN layers and layers which are alloyed with Al and In clearly show a modification of the applied voltage, the interface between the lowly Mg-doped and the highly Mg-doped GaN at $d = 1350$ nm show modulation of the voltage which is much more subtle. Fig. 4.13 shows the voltage behavior within the Mg-doped region of the specimen. A minor increase of the applied voltage on the interface between both different doping levels can be better visualized by the derivative of the voltage $\frac{\mathrm{d}V}{\mathrm{d}d}$. The voltage curve from which $\frac{\mathrm{d}V}{\mathrm{d}d}$ is calculated is smoothed according to Eq. (4.2) with $\sigma = 20$ nm.

The voltage rise during the field evaporation of a specimen with a constant activation energy of the field evaporation should be locally constant (in d). However shortly before

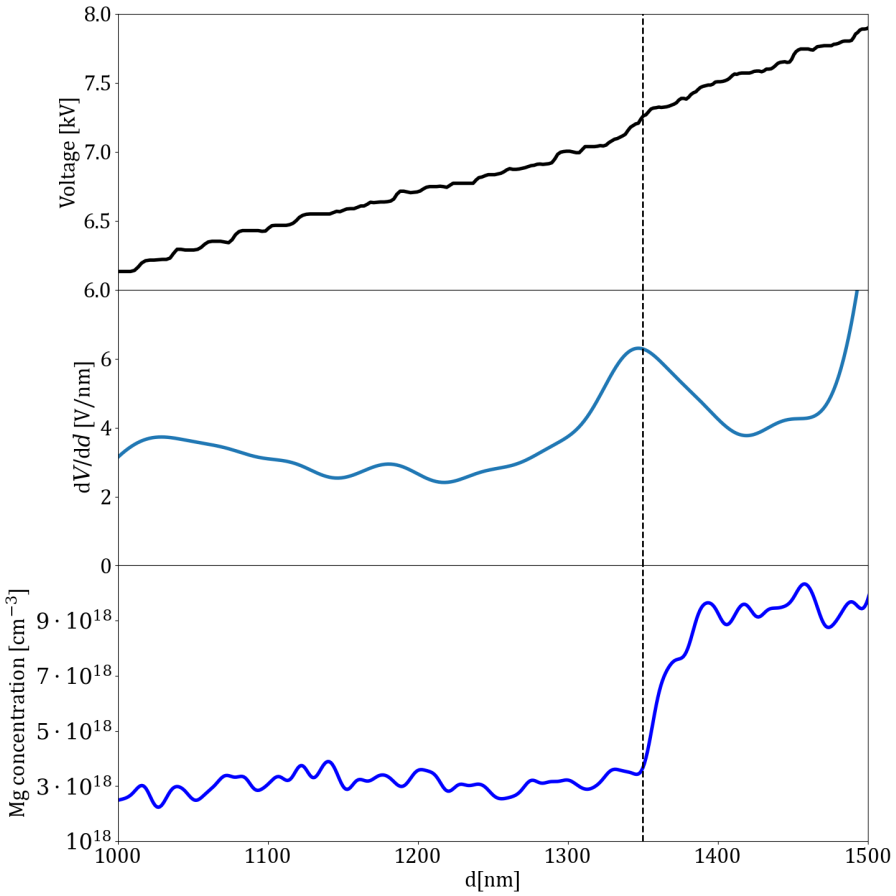

Figure 4.13: The voltage development in the region where the evaporation front transitions from the low-Mg doping region and the high-Mg doping region does not show the difference in the voltage behavior between these regions. The derivative of the applied voltage on the other hand clearly shows that an increase of the Mg-content leads to a more difficult evaporation of the material.

the Mg-rich section starts evaporating $\frac{\mathrm{d}V}{\mathrm{d}d}$ begins increasing. This is equivalent to an increase of the activation energy of field evaporation shortly before Mg atoms are starting to evaporate. At a given electric field strength the activation energy of the field evaporation process increases with a rising heat of sublimation and ionization energy of the evaporating species and decreases with a rise in the surface's electron affinity (Eq. (1.11)). Since Mg atoms in the doped regions only constitute a very minor fraction of the total composition ($< 0.1\%$), the evaporation of Mg atoms is not expected to provide a major contribution to the evaporation rate. Since the ionization energy is independent of the surface's chemical nature, only the heat of sublimation of the evaporating species and

the electron affinity of the surface have to be taken into consideration when discussing the difference in the evaporation behavior of the lowly and highly Mg-doped sections of the specimen. The effect of the increased doping level on the GaN:Mg's heat of sublimation has not been investigated in detail here, but the generally low relative Mg content within both differently doped layers suggests that the Mg incorporation only influences the binding energy of a small fraction of the specimen's Ga and N atoms. The electron affinity of GaN however has been shown to depend on the presence of Mg-dopants on the tip surface. By first principle density functional theory calculations the introduction of Mg-dopants into a GaN surface has been shown to reduce its electron affinity in Ji et al. (2016). This increase of the Mg content of a GaN layer can be expected to reduce the surface's electron affinity as well leading to an increase in the activation energy of the field evaporation (Eq. (1.11)). Due to the PAP experiment being performed under constant detection rate conditions, this increase of the activation energy results in an increase of the applied voltage. This statement is in qualitative agreement with the faster rise of the applied voltage once the Mg-rich region starts evaporating (Fig. 4.13), implying that the electron affinity might play a major role in the specimen's field evaporation behavior.

4.3.2 Behavior of surface electric field in the TJ region

The most drastic increase in the applied DC voltage takes place shortly before the TJ evaporates. This increase in voltage amounts to 1 kV. In Silaeva et al. (2014) the penetration of the electric field into an APT specimen is studied. In this study the screening of the electric field inside of the specimen is calculated. The screening of the electric field is caused by the accumulation of holes at the tip surface, which also cause the electric field that leads to the field evaporation of the surface atoms. In order for this screening to take place at the tip apex a sufficient amount of holes has to be present at the apex.

The surface field $\left(E_{\mathrm{surf}} = \frac{E_{\mathrm{ext}}}{\epsilon}\right)$ which penetrates into the specimen has to be screened by the accumulation of positive charges within a few nm distance from the tip apex. This means that holes are accumulating close to the tip apex. These *excess* holes have to be provided from the backbone of the specimen and cannot come from regions close to the tip apex due to its charge neutrality at zero voltage. Since the electric field which is present at the TJ during the APT experiment is directed towards the tip apex and the p-type doped faces it, the TJ experiences a reverse voltage bias during the performance of the PAP experiment.

Fig. 4.14 shows the behavior of the applied voltage and the Ga^{2+}/Ga^{+}- charge state ratio in the proximity of the TJ. While the applied voltage represents a requirement to

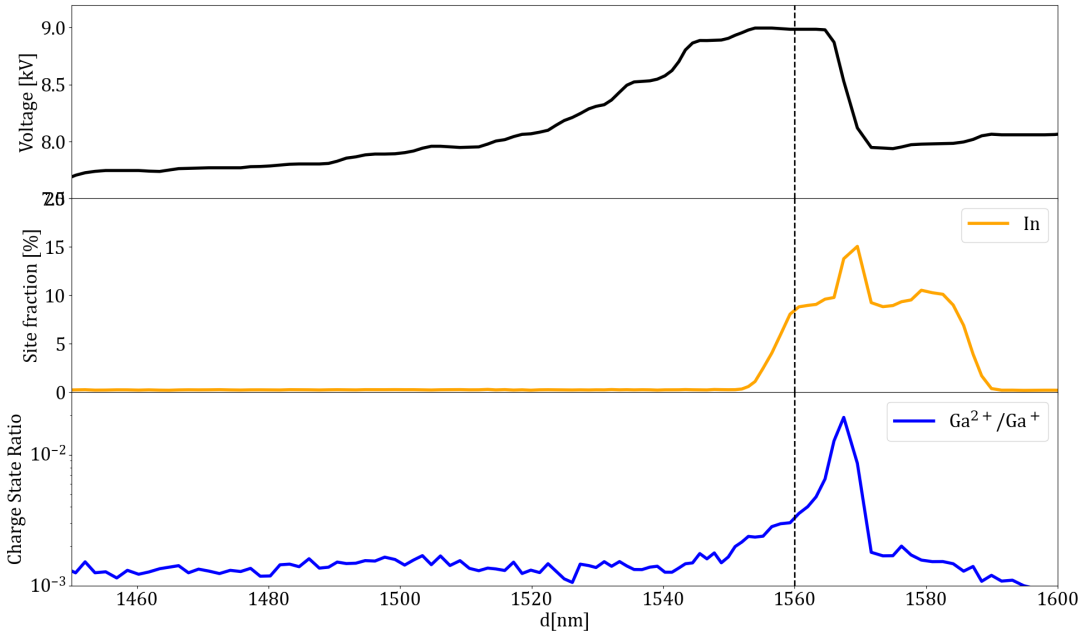

Figure 4.14: The voltage, the In-site fraction and the charge state ratio in the proximity of the TJ.

ensure a steady evaporation rate, the charge state ratio gives an estimate of the electric field which is present at the specimen apex. In Fig. 4.14 it can be seen that the initial increase of the applied voltage around $d = 1500$ nm does not directly cause an increase of the charge state ratio. This means that the increase of the voltage does not result in an increased electric field for 1500 nm $< d <$ 1540nm. The fact that the increase of the applied voltage shortly before TJ's cladding layers start evaporating does not contribute to the electric field on the specimen surface begs the question about the origin of this increase of roughly $\Delta V \approx 1$ kV.

4.4 Correlative Results of PL and APT

With the chemical and structural reconstruction data presented in Section 4.2 and Section 4.3 the specimen's PL response can be interpreted much more easily. Any contribution to a specific PL spectrum (Fig. 4.5d) at a fixed depth of analysis (d) can only originate from regions which are constituted by atoms which have a higher d-value than PL spectrum. Thus only those atoms which lie to the right of a specific color-coded spectrum are able to contribute to it. In order to separate the different components of

the measured PL signal a multi-Gaussian fit was applied to every PL spectrum:

$$\mathrm{Fit}(E) = k + \sum_{i=1}^{i_{\max}} A_i \cdot \exp\left(\frac{(E - E_i)^2}{2\sigma_i^2}\right) \tag{4.6}$$

This function is fitted onto every PL spectrum. Since the parameter $i_{\max}$ gives the number of the Gaussian utilized to fit the experimental data for a specific spectrum, its choice is not trivial. If $i_{\max}$ is chosen too low, it does not satisfy the complexity of the PL signal and if its value is overestimated, spectral deviations of the recorded spectra from the supposed Gaussian shape are falsely interpreted as a distinct signal. Due to the appearance and disappearance of PL signals during the specimen's field evaporation it is necessary to define different values of $i_{\max}$ for different regions of the specimen.

Fig. 4.15 shows the development of the characteristic PL energies of the identified components (E_i) as a function of d. For early ($d < 250$ nm) evaporation states, a description using two Gaussians ($i_{\max} = 2$) suffices in order to obtain a good fit of the measurement data. The two components present here are the GaN NBE signal (E_1 ≈3.5 eV) and the far below band gap PL emission, which is refered to as PL 2 in the following (E_2 ≈3.1 eV).

In the following region ((250 nm $< d <$ 710 nm) another spectral contribution with

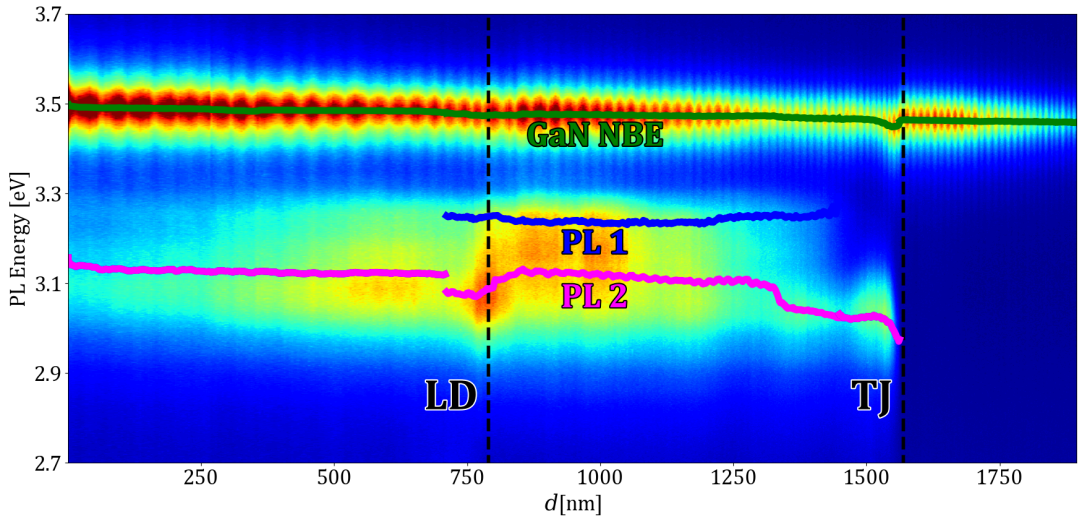

Figure 4.15: The specimen's PL response as a function of the depth-of-analysis d. The set of spectra is fitted utilizing Eq. (4.6). Different evaporation states (characterized by d) of the specimen show a varying level of distinguishable PL signals.

a slightly higher energy (E_3 ≈3.3 eV) starts becoming pronounced (refered to as the emission PL 1 in the following). This spectral component clearly appears after the upper cladding layer of the LD structure starts to evaporate. This clear feature continues to contribute to the PL signal until it continuously disappears in the Mg-doped region between LD and TJ. To describe this additional feature a third Gaussian ($i_{\max} = 3$) is introduced into the fitting procedure in this region (710 nm $< d <$ 1450 nm). Since this higher energy contribution is not well pronounced in the region where this new feature start appearing 250 nm $< d <$ 710 nm), the fitting routine does not converge well when fitting it with three Gaussians, the region $d <$ 710 nm is only fitted with $i_{\max} = 2$.

After the disappearance of the PL 1 signal a two Gaussian fit ($i_{\max} = 2$) is used until the PL 2 signal vanishes abruptly (1450 nm $< d <$ 1560 nm)). The remainder of the experimental PL spectra ($d >$ 1560 nm)) is fitted using only a single Gaussian ($i_{\max} = 1$).

Performing the fit described in Eq. (4.6) delivers the parameters describing the physical properties of the different spectral components of the total PL signal. These are the component i's characteristic energy (E_i), its spectral width (σ_i) and its peak intensity (A_i). In Fig. 4.15 the different spectral components' characteristic energy is laid over the specimen's d-resolved PL response. It should be kept in mind that the fit of the PL signals shown in Eq. (4.6) does not completely describe the experimentally observed PL spectrum. Especially the PL 1 signal appears before there region where it is fitted. However its low intensity at $d <$ 710 nm does not allow it to be properly distinguished from the PL 2 signal by the fitting procedure.

Utilizing the parameters, which are obtained from the previously discussed fitting procedure, the total intensity of a spectral component i is can be calculated as:

$$I_i = 2\pi\sigma_i \cdot A_i \tag{4.7}$$

4.4.1 Near Band Edge signal oscillation

The NBE-signal shows an oscillation of its total signal. The below band gap signal on the other hand only show a much lower intensity oscillation at the same frequency. Since the distance between the intensity maxima is not constant in d, it does not have a constant spatial frequency. The collection time of each recorded PL spectrum is 1 minute.

To further analyse this behavior, the PL intensity of the recorded PL spectrum is integrated in order to obtain a measure of the emission strength around the band gap and below the band gap. In order to do this, the detected PL intensity with a photon energy below 3.35 eV is assigned to the below band gap emission, while the intensity coming from photons with an energy higher than 3.35 eV is assigned to the NBE-signal.

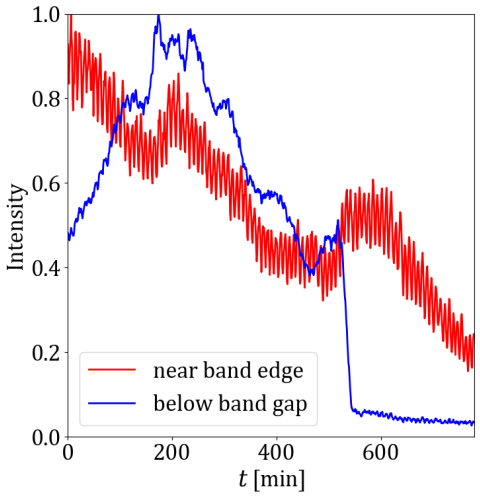

Figure 4.16: The PL intensity originating from near the GaN band gap ($E > 3.35$ eV) and coming from below the GaN band gap ($E < 3.35$ eV) as a function of the measurement time.

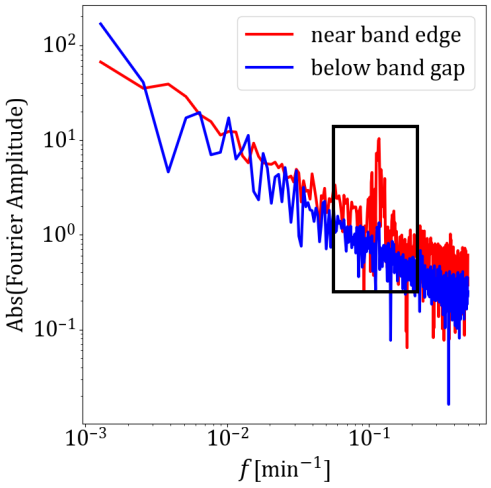

Figure 4.17: The Fourier transform of the curves described in Fig. 4.16. At the frequency f which corresponds to a period of roughly 8.5 minutes, the near gap signal's Fourier spectrum shows a maximum.

By integrating the intensity over the respective energy ranges, the PL signal's strength is calculated and shown as a function of the time of the atom's field evaporation with reference to the start of the PAP experiment in Fig. 4.16. In this graph we can see that the NBE signal shows a strong oscillating component, while the below GaN band gap signal doesn't show such a feature. The Fourier transform of the time-dependent PL intensity signals (Fig. 4.17) shows that there is a dominant frequency of the oscillation of the NBE signal. The period corresponding to this oscillation amounts to roughly 8.5 minutes. The signal below the GaN band gap is also influenced by this oscillation of the system. While having a much lower amplitude, it still shows a minor component in the Fourier spectrum, which corresponds to the period of 8.5 minutes (Fig. 4.17). In both spectral regions this oscillation might be either caused by periodic motions of the sample stage or by a periodic fluctuation of the laser power.

4.4.2 PL 1 Emission

While the concentrations of the alloying elements have to be relatively high in order to cause photoemission at a large energetic distance from the band-gap transition, doping can already influence the specimen's response at much lower concentrations. The

dominant dopant in the investigated system is Mg.

Since PAMBE allows for the deposition of high quality p-type doped GaN:Mg layers without the need for any annealing of the deposited specimen, the PL signals emitted from the investigated specimen are expected to show the same PL emission energy as observed for other PAMBE produced specimen. In Yan-Ping and Guang-Hui (2011) the PL response of PAMBE grown Mg-doped GaN is investigated. This work shows that the energy of the Mg donor-acceptor pair (DAP) PL emission occurs at about 200 meV below the NBE PL emission. Fig. 4.18a) shows that the difference between NBE the PL 1 energies takes values, which are similar to the expected binding energy of the DAPs.

Since the PL 1 emission slowly vanishes once the Mg-rich region between the LD and TJ is underway being evaporated (Fig. 4.5), this signal is identified to originate from the recombination of DAP photocarriers.

4.4.3 PL 2 Emission

Fig. 4.18b) shows the difference between the fitted energy of the PL emission 1 and the NBE energy. In the early phase of the specimen's field evaporation the PL energy of the PL 2 signal remains mostly constant. A major discontinuity of the energy difference is observed with the introduction of the third Gaussian used for the fit at $d = 710$ nm. While at this depth of analysis the peak intensity of the below band gap PL signal has a local minimum (Fig. 4.19), shortly after ($d = 780$ nm) there is a very clear peak in the detected intensity at an energy of 3.08 eV, which represents a red shift of the PL energy

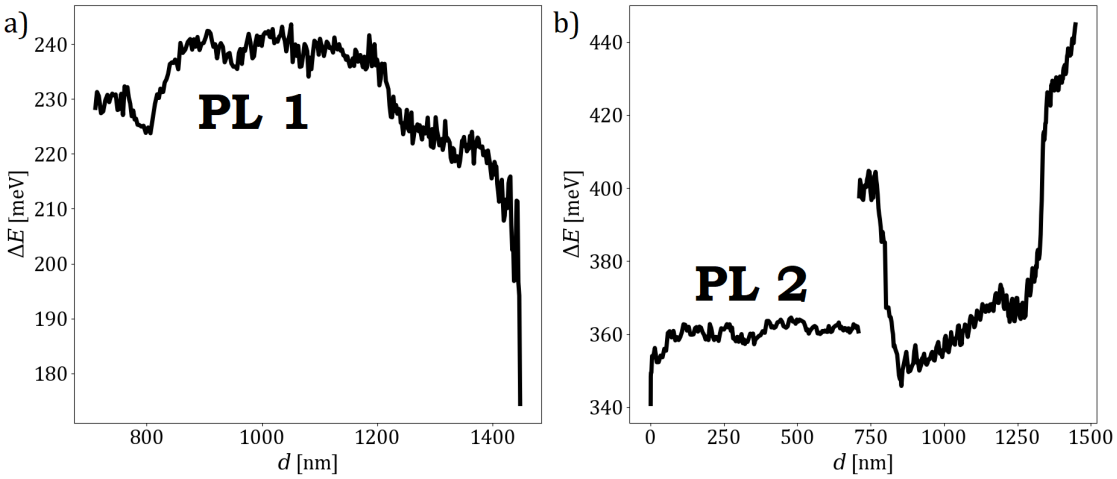

Figure 4.18: PL-energy difference between the NBE emission and a) the PL 1 emission, b) the PL 2 emission.

detected at $d < 710$ nm. Since this signal reaches its maximum peak intensity during the field evaporation of the laser diode QW, it is shown that it does not originate from the QW.

Fig. 4.19 shows the electric field present at the specimen apex as calculated from the charge state ratio (Gault et al. (2016)). The detection events of the entire detector's area are used for the calculation of both the charge state ratio and the electric field. Since the activation energy of field evaporation rises drastically with an increasing charge state of the evaporated ion (Eq. (1.11)) detected species with a charge higher than $+e$ are expected to be generated by electron tunneling from an emitted cation into the specimen at close proximity of the apex after the field evaporation has occured. This makes the charge-state ratio a material independent measure of the electric field at the atomic sites from where field evaporation takes place. It should be remarked that field evaporation only takes place at those exposed atomic sites which experience an especially high electric

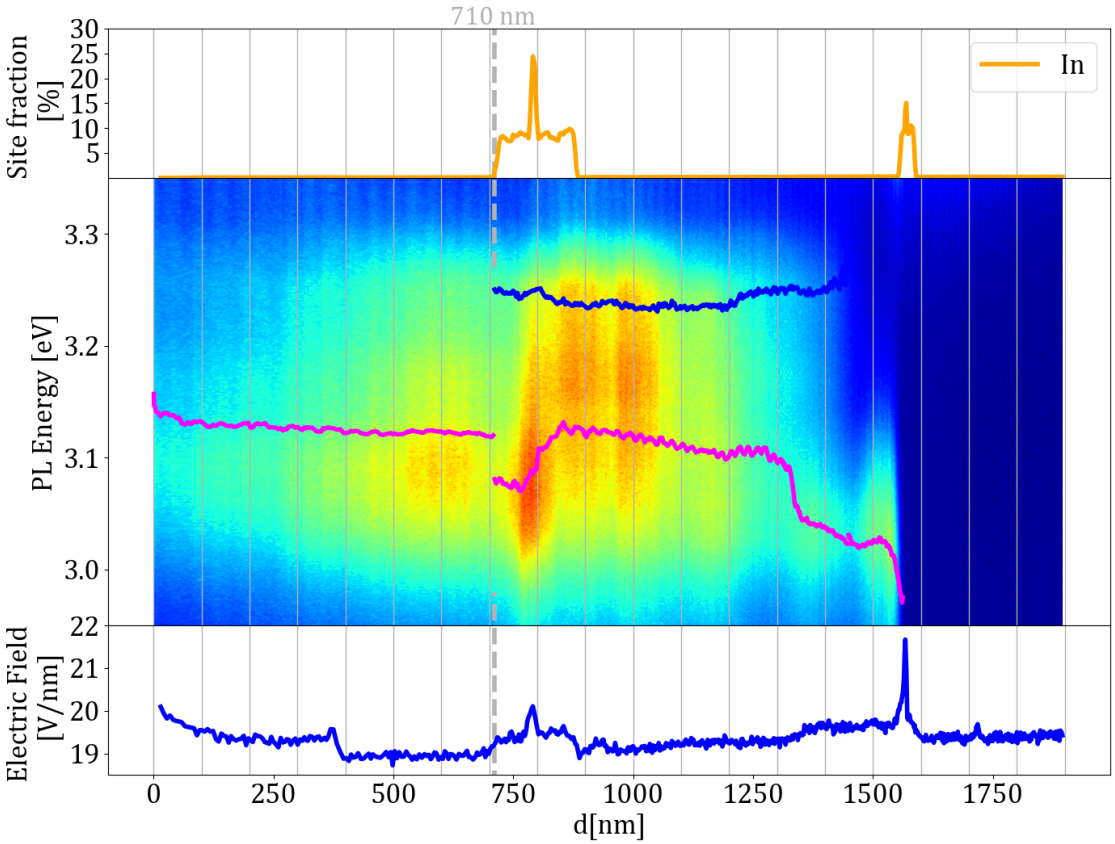

Figure 4.19: The below band-gap PL spectrum with the fits (Eq. (4.6)) of the PL 1 and PL 2 signals.

field, making the electric field calculated from the Kingham (1982)-theory an upper bound for the average electric field at the apex. Despite these limitations it can be deducted from the charge state ratio that the red-shift at $d = 780$ nm is accompanied by an increase of the electric field at the tip apex.

After the field evaporation of the QW and its cladding layers, the electric field and the energy of the PL 2 emission return to values which are similar to those with $d < 710$ nm ($F = 18.9$ V/nm). The increased electric field during the field evaporation of the In-rich layers of the (In,Ga)N QW ($F = 20.1$ V/nm) and its cladding layers ($F = 19.4$ V/nm) shows that this section is tougher to field evaporate.

During the field evaporation of the Mg-doped regions of the specimen which lie between the LD QW and the TJ both fitted PL signals develop mostly parallel to each other. Once the PL 1 emission starts vanishing ($d = 1330$ nm) the fit of the PL 2 emission also experiences a red-shift of the fitted energy. This suggests that the PL 2 emission fit in this section is connected to the emission of PL 1. The PL-spectroscopy data presented in Kaufmann et al. (1999) shows that the Mg-doping induced blue band PL emission of GaN can be expected in a wide energy range from 3.0 eV to 3.3 eV. Since it experiences a very sudden energy shift as soon as the PL 1 starts drastically decreasing in peak intensity the main contribution to the PL 2 emission in 840 nm $< d <$ 1330 nm also originates from Mg-doping.

The origin of the remaining below band gap signal of the later evaporation stages ($d > 1360$ nm) can be established by considering the depth of analyis where it vanishes. Fig. 4.20 shows a close-up of the correlative PAP data around the depth of analysis where the PL 2 signal vanishes. From the development of the fitted PL-intensity shown in this figure, it can be seen that it decreases over a distance of roughly 30 nm before fully vanishing. Over this distance the fitted PL energy is red shifted from 3.02 eV to 2.97 eV. The PL signal of the ZnO QW embedded in (Mg,Zn)O barrier material presented in Section 3.2 also starts vanishes at a similar distance from the evaporation front. This indicates that the PL 2 signal also contains a contribution from the either the TJ or from the TJ-cladding layers.

In Table 4.4 the transition energy of the different In-doped regions of the specimen is estimated from the PAP measured In-site fraction. The TJ cladding layer's band gap is estimated to be 3.1 eV and the TJ's band gap from the In-alloying is calculated to be 2.9 eV. Before the sudden drop of the below band gap PL emission ($d = 1545$ nm), the emission takes values between 3.02 eV and 3.05 eV. These observed PL emission energies are closer to the estimated PL energy of the cladding layers. Also a TJ has a strong internal electric field. This means that any free electrons and holes present within

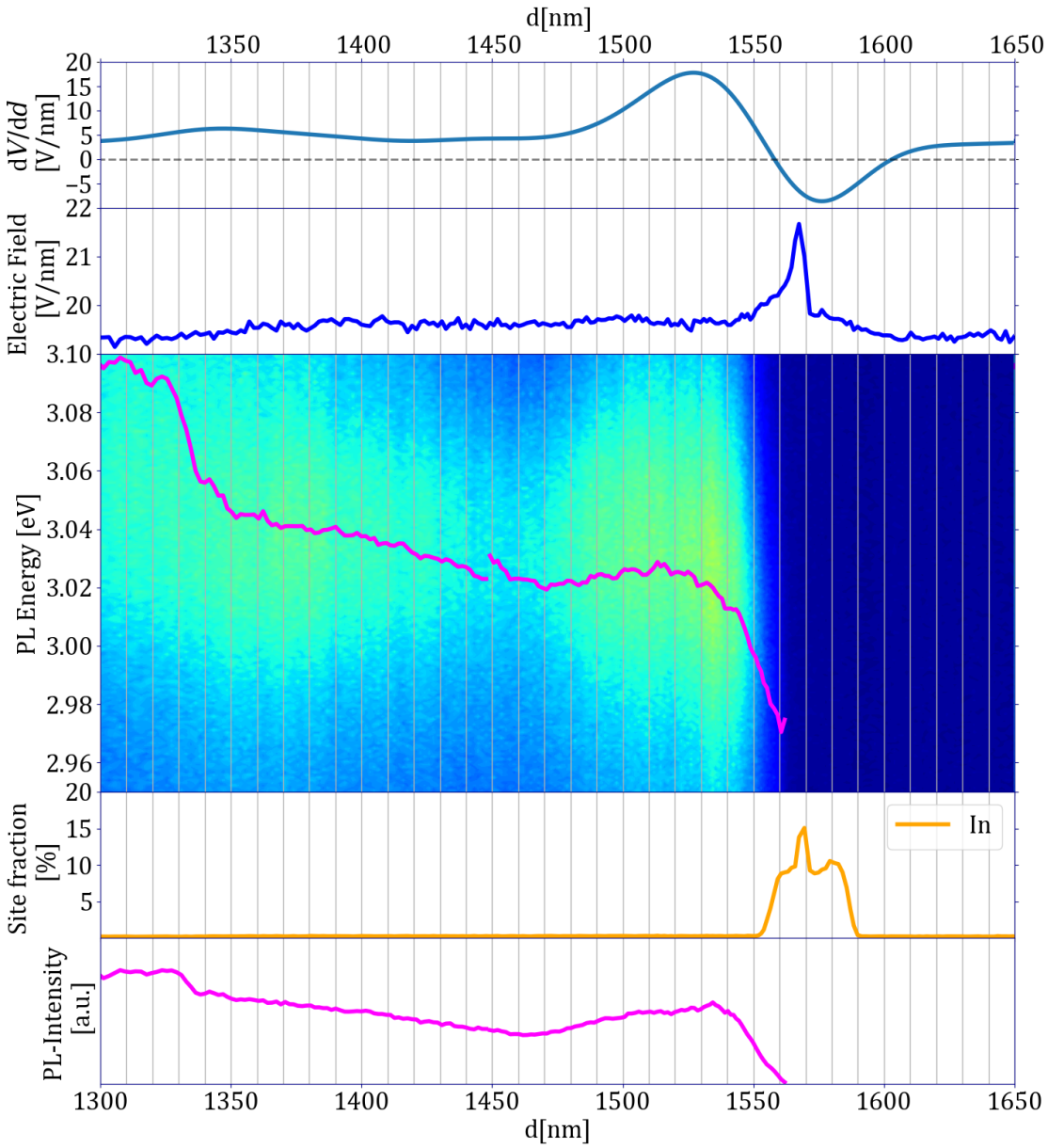

Figure 4.20: The correlated PAP data in the proximity of the TJ. The PL-intensity of PL 2 signal is calculated from the fits of the PL spectra using Eq. (4.7).

it experience an acceleration in opposing directions, leading to their spatial separation. This leads to a smaller overlap of their wave function, resulting in a suppressed PL emission. Thus we conclude that the PL 2 signal in 1350 nm $< d <$ 1530 nm stems from the (In,Ga)N cladding layer of the TJ.

Before the below band gap signal finally vanishes around $d = 1560$ nm it experiences a redshift. Only the final part of this redshift ($d > 1540$ nm) is accompanied by an increase of the electric field at the specimen apex. This implies that the redshift is not primarily induced by an increased electric field strength or by an increase of the mechanical stress close to the apex induced by it. After the vanishing of the PL signal the electric field reaches its maximum around $d = 1570$ nm. At this maximum electric field strength, the applied voltage is already decreasing.

4.5 Summary of the Correlated Results

With the identification of the different contributions to the specimen's PL response in the previous sections the physical origin of the dominant contribution to the detected PL spectrum are determined (Fig. 4.21). The high energy contribution is determined to originate from the NBE interband transition of the GaN phase. Since GaN is present at every evaporation state of the specimen, this response can be observed for the entire experiment.

The lower emitted energies are dominated by the DAP emission coming from the Mg-doped sections of the specimen. This contribution fades out over a relatively large range depth of analysis range. Once a large part of the Mg-doped portion of the specimen has been fully field evaporated the PL response of the bottom cladding layer of the TJ becomes pronounced. While it can be identified at an energy which is distinct from the DAP emission, the exact depth of analysis of its onset can not be clearly identified due to its overlap with the broad DAP signal. This signal can thus only be identified once the DAP signal has experienced a significant decline in intensity and shows a relatively low intensity. Since the cladding layer of the TJ is much thinner than the Mg-doped region, its PL response shows a very swift decline once the evaporation front has approached it. The QW which represents the optically active zone located at the LD's center does not show any PL emission at the energy estimated from the measured In-content (2.6 eV Table 4.4).

The pulsed laser which is used to trigger the field evaporation and to excite the specimen's PL response is focussed on the original apex of the specimen ($d = 0$ nm). The laser spot size is roughly 2 μm and comparable to the entire depth of the analysis. This means that the sections of the specimen which have a low d-value experience a higher excitation from the laser than those with a high d-value. For the interpretation of the comparably low intensity of the TJ's cladding layer's optical response it has to be taken into account that this section does not experience the same laser excitation as

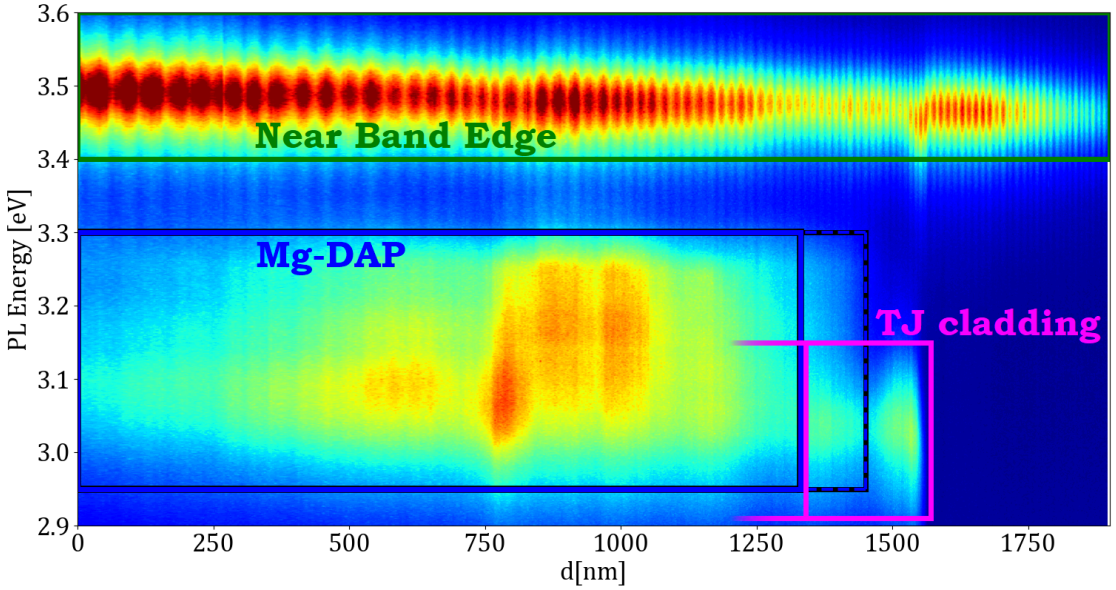

Figure 4.21: Total overview of the specimen's PL response as it was assigned in this chapter. The dominant source of the below band edge PL emission is found to be the Mg donor acceptor pairs for most the experiment. After most of the Mg-rich region of the specimen has been field evaporated, the PL response of the TJ cladding layers becomes pronounced.

section of the specimen with a lower *d*-value.

A question which still remains open is the unusual behavior of the applied voltage and the electric field in the proximity of the TJ (Fig. 4.20). The observation that a decrease of the applied voltage would lead an increase of the electric field present at the tip apex is counter-intuitive. Since no comprehensive explanation of this observation of this unusual behavior has been found yet, it still requires further investigation.

Overall the correlative PAP analysis of the (In,Ga)N laser diode presented in this section has shown interesting results on both the PAP technique and the investigated heterostructure. It has been shown that a high depth of analysis is possible to be measured via PAP. This also allows to study entire heterostructured semiconductor devices using this instrument. The evaluation of the APT data which is presented here allows for an estimation of the doping levels of different layers within the system. The In-site fraction within the different layers has also been measured. A comparison of the chemical modulations with the PL response allows to locate the original region of the different spectral contributions.

Conclusion

This thesis presents an investigation of semiconductor heterostructures using the Photonic Atom Probe. Such heterostructures consisting of the (Mg,Zn)O and (Al,Ga,In)N material systems are presented here in order to investigate different aspects of both the instrumental behavior of the PAP and the material system.

The ZnO Quantum Wells embedded within (Mg,Zn)O-barrier material are presented as a model system for a general study of the behavior of the detected PL intensity emitted from localized PL emitters embedded within an Atom Probe Tomography specimen. The conclusions obtained from the investigations of the ZnO QW's PL emission treat the interaction between the specimen, the light and the PAP set-up which is used to detect the specimen's optical response. The FDTD calculations and their evaluation presented in this thesis take into consideration these three aspects of the PAP experiment and investigate their interdependencies.

In the polarization resolved PAP study of a QW's PL emission it is shown that a QW embedded within an APT specimen shows a PL emission polarized perpendicular to the tip main axis (σ) while the emission of its barrier material is polarized along the tip axis (π). This result is obtained for both the polar c-axis and the non-polar a-axis oriented along the PAP set-up's optical axis. The experimental studies are supplemented by a series of FDTD simulations that serve to simulate the propagation of both the PAP's exciting laser pulse and the QW's PL response inside of the specimen. By the simulation of the polarization resolved PL signal which arrives at the PAP's PL detector insights about the dipole orientation of the PL emission within the specimen are gained. Comparing the experimental and the simulation results shows that the PL emission of the localized QW is mostly polarized within the m-plane. This result is in conflict with the previously reported behavior of planar samples that show a strong polarization in the c-plane. While the reason for this disagreement is still unclear the specific morphology of the QW is suggested as a mechanism for the modulation of the optical response. A possible expansion of the polarization resolved PAP technique presented here is to study

the behavior of a field evaporating PAP specimen (in-operando). The main issue when considering such an experiment is that the non-polarization filtered PL emission has to be intensive enough so that it still gives a sufficient signal after polarization filtering.

Additionally to the polarization resolved study of the ZnO QW, which was performed without any applied voltage, another PAP study of a ZnO QW specimen, which is under field evaporation conditions, is performed. The focus of this study is the explanation of the mechanisms behind the development of the detected PL intensity as a function of the developing tip geometry. For this purpose a set of tip geometries which mimics its geometric evolution is defined and FDTD simulations are performed on this set of geometries. The goal of these simulations is to simulate the PAP's PL generation and PL detection capabilities as a function of the specimen evaporation progress. The simulation of the PL emission of the PAP specimen assuming bulk material properties gives a qualitative description of the experimental PL development, when taking into account the dominant orientation of the emitting dipoles as obtained from the polarization resolved analysis. However taking into consideration the modulation of the specimen's optical properties due to the high surface field during the performance of an APT experiment allows for a quantitative description of the measured PL by FDTD calculation. This agreement between calculation and experiment further fortifies the notion that the uniquely high electric field which is present during any APT experiment also modulates the specimen's optical properties.

The investigation of a (In,Ga)N Laser Diode with a burried (In,Ga)N Tunnel Junction embedded within a wurzite (Al,In,Ga)N heterostructure specimen presents a correlated study of the APT and PL properties of the specimen as performed within the PAP. Both the Ga-site fraction of the elements which are used to locally modify the band gap of the GaN base material (Al,In) and the concentration of doping elements (Ge and Mg) are investigated. The overlap of the Si mass-peaks with the N-signals has hindered the dopant quantification of the Si doped sections of the specimen. By comparing the compositional information obtained from the APT part of the PAP experiment to the PL information obtained by the instrument the original region and mechanism of the PL generation is obtained. It is shown that the specimen's PL emission at energies below the band gap is dominated by the radiation generated by the GaN-Mg donor acceptor pairs from below the LD. Only once the Mg-doped section of the specimen has been fully field evaporated, a PL signal coming from the TJ's cladding layers becomes pronounced. A special focus is set on investigation of the electric field behavior during the field evaporation of this specimen. It is shown that the DC voltage applied to the specimen rises without causing an increase in the surface field shortly before the TJ start undergoing field evaporation.

Overall the study of the laser diode has shown that the PAP technique is applicable for the correlative study of semiconductor device heterostructures, which of course should be expanded in the future.

One material system of particular interest for future investigations are biological samples. The molecular species generated from the field evaporation of biological specimens often poses a challenge for the chemical identification of the mass peaks. Introducing optically active markers into such systems (fluorescent proteins or quantum dots) allows for an additional opportunity to localize the position of a protein embedded in a frozen solution or in a matrix material. From the vanishing of the marker's optical response in the PL spectrum the marked molecule can be localized within the APT reconstruction data. By comparing the mass spectrum of the section of the reconstruction where the protein is present with the mass spectrum, where it is absent the detection events characteristic to the protein can be identified in the mass spectrum. An analysis of the distribution of these species then would allow localizing the protein throughout the specimen.

Ajay, A., Schörmann, J., Jiménez-Rodriguez, M., Lim, C. B., Walther, F., Rohnke, M., Mouton, I., Amichi, L., Bougerol, C., Hertog, M. I. D., Eickhoff, M., and Monroy, E. (2016). Ge doping of GaN beyond the Mott transition. *Journal of Physics D: Applied Physics*, 49(44):445301.

Akasaki, I. (2007). Key inventions in the history of nitride-based blue LED and LD. *Journal of Crystal Growth*, 300(1):2–10. First International Symposium on Growth of Nitrides.

Amano, H., Kito, M., Hiramatsu, K., and Akasaki, I. (1989). P-Type Conduction in Mg-Doped GaN Treated with Low-Energy Electron Beam Irradiation (LEEBI). *Japanese Journal of Applied Physics*, 28(12A):L2112.

Amano, H., Kitoh, M., Hiramatsu, K., and Akasaki, I. (1990). Growth and Luminescence Properties of Mg-Doped GaN Prepared by MOVPE. *Journal of The Electrochemical Society*, 137(5):1639.

Ambacher, O. (1998). Growth and applications of Group III-nitrides. *Journal of Physics D: Applied Physics*, 31(20):2653.

Amichi, L., Mouton, I., Di Russo, E., Boureau, V., Barbier, F., Dussaigne, A., Grenier, A., Jouneau, P.-H., Bougerol, C., and Cooper, D. (2020). Three-dimensional measurement of Mg dopant distribution and electrical activity in GaN by correlative atom probe tomography and off-axis electron holography. *Journal of Applied Physics*, 127(6):065702.

Anikeeva, P. O., Halpert, J. E., Bawendi, M. G., and Bulović, V. (2007). Electroluminescence from a Mixed Red-Green-Blue Colloidal Quantum Dot Monolayer. *Nano Lett.*, 7(8):2196–2200.

Blavette, D., Bostel, A., Sarrau, J. M., Deconihout, B., and Menand, A. (1993). An atom probe for three-dimensional tomography. *Nature*, 363(6428):432–435.

Blum, I., Cuvilly, F., and Lefebvre-Ulrikson, W. (2016). Chapter Four - Atom Probe Sample Preparation. In Lefebvre-Ulrikson, W., Vurpillot, F., and Sauvage, X., editors, *Atom Probe Tomography*, pages 97–121. Academic Press.

Bogdanowicz, J., Kumar, A., Fleischmann, C., Gilbert, M., Houard, J., Vella, A., and Vandervorst, W. (2018). Laser-assisted atom probe tomography of semiconductors: The impact of the focused-ion beam specimen preparation. *Ultramicroscopy*, 188:19–23.

Bogusławski, P. and Bernholc, J. (1997). Doping properties of C, Si, and Ge impurities in GaN and AlN. *Phys. Rev. B*, 56:9496–9505.

Bostel, A., Blavette, D., Menand, A., and Sarrau, J. M. (1989). Toward a Tomographic Atom-Probe. *J. Phys. Colloques*, 50:C8–501–C8–506.

Bouhelier, A., Beversluis, M., Hartschuh, A., and Novotny, L. (2003). Near-Field Second-Harmonic Generation Induced by Local Field Enhancement. *Phys. Rev. Lett.*, 90:013903.

Burstein, E. (1954). Anomalous Optical Absorption Limit in InSb. *Phys. Rev.*, 93:632–633.

Cadeddu, D., Munsch, M., Rossi, N., Gérard, J.-M., Claudon, J., Warburton, R. J., and Poggio, M. (2017). Electric-field sensing with a scanning fiber-coupled quantum dot. *Physical Review Applied*, 8(3):031002.

Cerezo, A., Godfrey, T. J., and Smith, G. D. W. (1988). Application of a position-sensitive detector to atom probe microanalysis. *Review of Scientific Instruments*, 59(6):862–866.

Cerezo, A., Grovenor, C. R. M., and Smith, G. D. W. (1986). Pulsed laser atom probe analysis of semiconductor materials. *Journal of Microscopy*, 141(2):155–170.

Chaisakul, P., Vakarin, V., Frigerio, J., Chrastina, D., Isella, G., Vivien, L., and Marris-Morini, D. (2019). Recent Progress on Ge/SiGe Quantum Well Optical Modulators, Detectors, and Emitters for Optical Interconnects. *Photonics for Solar Energy Systems IX*, 6(1):24.

Chauveau, J.-M., Laügt, M., Venneguès, P., Teisseire, M., Lo, B., Deparis, C., Morhain, C., and Vinter, B. (2008). Non-polar a-plane ZnMgO/ZnO quantum wells grown by molecular beam epitaxy. *Semicond. Sci. Technol.*, 23(3):035005.

Chen, Y., Ben, J., Xu, F., Li, J., Chen, Y., Sun, X., and Li, D. (2021). Review on the Progress of AlGaN-based Ultraviolet Light-Emitting Diodes. *Fundamental Research*, 1(6):717–734.

Crewe, A. V., Eggenberger, D. N., Wall, J., and Welter, L. M. (1968). Electron Gun Using a Field Emission Source. *Review of Scientific Instruments*, 39(4):576–583.

Da Costa, G., Vurpillot, F., Bostel, A., Bouet, M., and Deconihout, B. (2004). Design of a delay-line position-sensitive detector with improved performance. *Review of Scientific Instruments*, 76(1):013304.

Dalapati, P., Beainy, G., Di Russo, E., Blum, I., Houard, J., Moldovan, S., Vella, A., Vurpillot, F., Le Biavan, N., Hugues, M., Chauveau, J., and Rigutti, L. (2021). In Situ Spectroscopic Study of the Optomechanical Properties of Evaporating Field Ion Emitters . *Phys. Rev. Applied*, 15:024014.

Dalapati, P., Weikum, E. M., Beainy, G., Russo, E. D., Houard, J., Moldovan, S., Vella, A., Chauveau, J. M., Hugues, M., Biavan, N. L., Tchernycheva, M., Julien, F. H., Saghi, Z., and Rigutti, L. (2022). Polarization-resolved photoluminescence study of an atom probe tip containing a ZnO-(Mg,Zn)O heterostructure . *SPIE Proceedings*, 12002:l–1.

Davey, J. E. and Pankey, T. (1968). Epitaxial GaAs Films Deposited by Vacuum Evaporation. *Journal of Applied Physics*, 39(4):1941–1948.

Davydov, V., Klochikhin, A., Emtsev, V., Kurdyukov, D., Ivanov, S., Vekshin, V., Bechstedt, F., Furthmüller, J., Aderhold, J., Graul, J., Mudryi, A., Harima, H., Hashimoto, A., Yamamoto, A., and Haller, E. (2002). Band Gap of Hexagonal InN and InGaN Alloys. *physica status solidi (b)*, 234(3):787–795.

Deconihout, B., Bostel, A., Bas, P., Chambreland, S., Letellier, L., Danoix, F., and Blavette, D. (1994). Investigation of some selected metallurgical problems with the tomographic atom probe. *Applied Surface Science*, 76-77:145–154.

Deconihout, B., Bostel, A., Menand, A., Sarrau, J., Bouet, M., Chambreland, S., and Blavette, D. (1993). "On the development of a 3D tomographic atom-probe. *Applied Surface Science*, 67(1):444–450.

Di Russo, E., Dalapati, P., Houard, J., Venturi, L., Blum, I., Moldovan, S., Le Biavan, N., Lefebvre, D., Hugues, M., Chauveau, J. M., Blavette, D. C., Deconihout, B., Vella, A., Vurpillot, F., and Rigutti, L. (2020). Super-resolution Optical Spectroscopy of Nanoscale Emitters within a Photonic Atom Probe. *Nano Letters*, 20(12):8733–8738. PMID: 33236638.

Di Russo, E., Mancini, L., Moyon, F., Moldovan, S., Houard, J., Julien, F. H., Tchernycheva, M., Chauveau, J. M., Hugues, M., Da Costa, G., Blum, I., Lefebvre, W.,

Blavette, D., and Rigutti, L. (2017). Three-dimensional atomic-scale investigation of ZnO-MgxZn1-xO m-plane heterostructures. *Appl. Phys. Lett.*, 111(3):032108.

Dimkou, I., Di Russo, E., Dalapati, P., Houard, J., Rochat, N., Cooper, D., Bellet-Amarlic, E., Grenier, A., Monroy, E., and Rigutti, L. (2020). InGaN Quantum Dots Studied by Correlative Microscopy Techniques for Enhanced Light-Emitting Diodes. *ACS Applied Nano Materials*, 3(10):10133–10143.

Dingle, R., Wiegmann, W., and Henry, C. H. (1974). Quantum States of Confined Carriers in Very Thin $Al_xGa_{1-x}As$-GaAs-$Al_xGa_{1-x}As$ Heterostructures. *Phys. Rev. Lett.*, 33:827–830.

Drachsel, W., Nishigaki, S., and Block, J. (1980). Photon-induced field ionization mass spectroscopy. *International Journal of Mass Spectrometry and Ion Physics*, 32(4):333–343.

Edwards, P. and Martin, R. (2011). Cathodoluminescence nano-characterization of semiconductors. *Semiconductor Science and Technology*, 26.

Esaki, L. (1958). New Phenomenon in Narrow Germanium $p-n$ Junctions. *Phys. Rev.*, 109:603–604.

Fichtenbaum, N. A., Schaake, C., Mates, T. E., Cobb, C., Keller, S., DenBaars, S. P., and Mishra, U. K. (2007). Electrical characterization of p-type N-polar and Ga-polar GaN grown by metalorganic chemical vapor deposition. *Applied Physics Letters*, 91(17):172105.

Fowler, R. H. and Nordheim, L. (1928). Electron emission in intense electric fields. *Proceedings of the Royal Society of London. Series A, Containing Papers of a Mathematical and Physical Character*, 119(781):173–181.

Frith, J. and Rodgers, C. (1896). XLI. On the resistance of the electric arc. *The London, Edinburgh, and Dublin Philosophical Magazine and Journal of Science*, 42(258):407–423.

Gault, B., Moody, M. P., Cairney, J. M., and Ringer, S. P. (2012). *Specimen Preparation*. Springer New York Heidelberg Dordrecht London.

Gault, B., Saxey, D. W., Ashton, M. W., Sinnott, S. B., Chiaramonti, A. N., Moody, M. P., and Schreiber, D. K. (2016). Behavior of molecules and molecular ions near a field emitter. *New Journal of Physics*, 18(3):033031.

Gault, B., Vurpillot, F., Vella, A., Gilbert, M., Menand, A., Blavette, D., and Deconihout, B. (2006). Design of a femtosecond laser assisted tomographic atom probe. *Review of Scientific Instruments*, 77(4):043705.

Grandjean, N., Damilano, B., and Massies, J. (2001). Group-III nitride quantum heterostructures grown by molecular beam epitaxy. *Journal of Physics: Condensed Matter*, 13(32):6945.

Hangleiter, A., Hitzel, F., Netzel, C., Fuhrmann, D., Rossow, U., Ade, G., and Hinze, P. (2005). Suppression of Nonradiative Recombination by V-Shaped Pits in GaInN/GaN Quantum Wells Produces a Large Increase in the Light Emission Efficiency. *Phys. Rev. Lett.*, 95:127402.

Haro-González, P., Martínez-Maestro, L., Martín, I., García-Solé, J., and Jaque, D. (2012). High-sensitivity fluorescence lifetime thermal sensing based on CdTe quantum dots. *small*, 8(17):2652–2658.

Hierro, A., Montes Bajo, M., Tamayo-Arriola, J., Ulloa, J., Le Biavan, N., Lefebvre, D., Hugues, M., Chauveau, J.-M., and Vennéguès, P. (2019). Intersubband absorption at normal incidence by m-plane ZnO/MgZnO quantum wells. page 80.

Hitzel, F., Klewer, G., Lahmann, S., Rossow, U., and Hangleiter, A. (2004). Narrow high-energy emission lines in high-resolution near-field spectroscopy on GaInN/GaN quantum wells. *physica status solidi (c)*, 1(10):2520–2523.

Houard, J., Normand, A., Russo, E. D., Bacchi, C., Dalapati, P., Beainy, G., Moldovan, S., Costa, G. D., Delaroche, F., Vaudolon, C., Chauveau, J. M., Hugues, M., Blavette, D., Deconihout, B., Vella, A., Vurpillot, F., and Rigutti, L. (2020). A photonic atom probe coupling 3D atomic scale analysis with in situ photoluminescence spectroscopy . *Rev. Sci. Instrum.*, 91:083704.

Jacopin, G., Rigutti, L., Bugallo, A. D. L., Julien, F. H., Baratto, C., Comini, E., Ferroni, M., and Tchernycheva, M. (2011). High degree of polarization of the near-band-edge photoluminescence in ZnO nanowires. *Nanoscale Research Letters*, 6(1):501.

Jeannin, M., Artioli, A., Rueda-Fonseca, P., Bellet-Amalric, E., Kheng, K., André, R., Tatarenko, S., Cibert, J., Ferrand, D., and Nogues, G. (2017). Light-hole exciton in a nanowire quantum dot. *Phys. Rev. B*, 95:035305.

Ji, Y.-J., Du, Y.-J., and Wang, M.-S. (2016). Electron affinity of GaN(0001) surface doped with Al, Mg. *Optik*, 127(7):3624–3628.

Kaufmann, U., Kunzer, M., Obloh, H., Maier, M., Manz, C., Ramakrishnan, A., and Santic, B. (1999). Origin of defect-related photoluminescence bands in doped and nominally undoped GaN. *Phys. Rev. B*, 59:5561–5567.

Kellogg, G. L. and Tsong, T. T. (1980). Pulsed-laser atom-probe field-ion microscopy. *J. Appl. Phys.*, 51(2):1184–1193.

Kelly, T. F., Vella, A., Bunton, J. H., Houard, J., Silaeva, E. P., Bogdanowicz, J., and Vandervorst, W. (2014a). Laser pulsing of field evaporation in atom probe tomography. *Current Opinion in Solid State and Materials Science*, 18(2):81–89.

Kelly, T. F., Vella, A., Bunton, J. H., Houard, J., Silaeva, E. P., Bogdanowicz, J., and Vandervorst, W. (2014b). Laser pulsing of field evaporation in atom probe tomography. *Current Opinion in Solid State and Materials Science*, 18(2):81–89.

Kemper, R., Veit, P., Mietze, C., Dempewolf, A., Wecker, T., Bertram, F., Christen, J., Lindner, J., and As, D. (2015). STEM-CL investigations on the influence of stacking faults on the optical emission of cubic GaN epilayers and cubic GaN/AlN multiquantum wells. *physica status solidi (c)*, 12.

Kettler, J., Vaish, N., de Lépinay, L. M., Besga, B., de Assis, P.-L., Bourgeois, O., Auffèves, A., Richard, M., Claudon, J., Gérard, J.-M., Pigeau, B., Arcizet, O., Verlot, P., and Poizat, J.-P. (2021). Inducing micromechanical motion by optical excitation of a single quantum dot. *Nat. Nanotechnol.*, 16(3):283–287.

Kingham, D. R. (1982). The post-ionization of field evaporated ions: A theoretical explanation of multiple charge states. *Surface Science*, 116(2):273–301.

Kirste, R., Hoffmann, M. P., Sachet, E., Bobea, M., Bryan, Z., Bryan, I., Nenstiel, C., Hoffmann, A., Maria, J.-P., Collazo, R., and Sitar, Z. (2013). Ge doped GaN with controllable high carrier concentration for plasmonic applications. *Applied Physics Letters*, 103(24):242107.

Konczewicz, L., Litwin-Staszewska, E., Zajac, M., Turski, H., Bockowski, M., Schiavon, D., Chlipała, M., Iwinska, M., Nita, P., Juillaguet, S., and Contreras, S. (2022). Electrical transport properties of highly doped N-type GaN materials. *Semiconductor Science and Technology*, 37(5):055012.

Krishnamoorthy, S., Akyol, F., and Rajan, S. (2014). InGaN/GaN tunnel junctions for hole injection in GaN light emitting diodes. *Applied Physics Letters*, 105(14):141104.

Langer, D. W., Euwema, R. N., Era, K., and Koda, T. (1970). Spin Exchange in Excitons, the Quasicubic Model and Deformation Potentials in II-VI Compounds. *Phys. Rev. B*, 2:4005–4022.

Lee, J., Sundar, V. C., Heine, J. R., Bawendi, M. G., and Jensen, K. F. (2000). Full Color Emission from II–VI Semiconductor Quantum Dot–Polymer Composites. *Adv. Mater.*, 12(15):1102–1105.

Li, Z., Tang, P., Zhang, Z., Guo, B., Su, Y.-Y., and Yun (2019). Nanoscale Characterization of V-defect in InGaN/GaN QWs LEDs using Near-Field Scanning Optical Microscopy. *Nanomaterials*, 9:633.

Li, Z., Wang, M., Fang, X., Li, Y., Zhou, X., Yu, H., Wang, P., Wang, W., and Pan, J. (2018). Monolithic integration of InGaAs/InP multiple quantum wells on SOI substrates for photonic devices. *Journal of Applied Physics*, 123(5):053102.

Lu, Y., Emanetoglu, N. W., and Chen, Y. (2006). Chapter 13 - ZnO Piezoelectric Devices. In Jagadish, C. and Pearton, S., editors, *Zinc Oxide Bulk, Thin Films and Nanostructures*, pages 443–489. Elsevier Science Ltd, Oxford.

Manasevit, H. M. (1968). Single Crystal Gallium Arsenide on Insulating Substrates. *Applied Physics Letters*, 12(4):156–159.

Mancini, L., Hernández-Maldonado, D., Lefebvre, W., Houard, J., Blum, I., Vurpillot, F., Eymery, J., Durand, C., Tchernycheva, M., and Rigutti, L. (2016). Multi-microscopy study of the influence of stacking faults and three-dimensional In distribution on the optical properties of m-plane InGaN quantum wells grown on microwire sidewalls. *Applied Physics Letters*, 108(4):042102.

Mancini, L., Moyon, F., Hernàndez-Maldonado, D., Blum, I., Houard, J., Lefebvre, W., Vurpillot, F., Das, A., Monroy, E., and Rigutti, L. (2017). Carrier Localization in GaN/AlN Quantum Dots As Revealed by Three-Dimensional Multimicroscopy. *Nano Letters*, 17(7):4261–4269. PMID: 28654283.

Matsui, H. and Tabata, H. (2009). In-plane anisotropy of polarized photoluminescence in M-plane (101^{-}) ZnO and MgZnO/ZnO multiple quantum wells. *Applied Physics Letters*, 94(16):161907.

Müller, E. W. (1937). Elektronenmikroskopische Beobachtungen von Feldkathoden. *Zeitschrift für Physik*, 106(9):541–550.

Müller, E. W. (1943). Das Auflösungsvermögen des Feldelektronenmikroskops. *Zeitschrift für Physik*, 120(5):270–282.

Müller, E. W. (1951). Das Feldionenmikroskop. *Zeitschrift für Physik*, 131(1):136–142.

Müller, E. W., Panitz, J. A., and McLane, S. B. (1968). The Atom-Probe Field Ion Microscope. *Review of Scientific Instruments*, 39(1):83–86.

Morhain, C., Bretagnon, T., Lefebvre, P., Tang, X., Valvin, P., Guillet, T., Gil, B., Taliercio, T., Teisseire-Doninelli, M., Vinter, B., and Deparis, C. (2005). Internal electric field in wurtzite ZnO/$Zn_{0.78}Mg_{0.22}O$ quantum wells. *Phys. Rev. B*, 72:241305.

Moss, T. S. (1954). The Interpretation of the Properties of Indium Antimonide. *Proceedings of the Physical Society. Section B*, 67(10):775.

Müller, E. W. (1956). Field Desorption. *Phys. Rev.*, 102:618–624.

Munsch, M., Kuhlmann, A. V., Cadeddu, D., Gérard, J.-M., Claudon, J., Poggio, M., and Warburton, R. J. (2017). Resonant driving of a single photon emitter embedded in a mechanical oscillator. *Nature communications*, 8(1):1–7.

Nakamura, S., Senoh, M. S. M., and Mukai, T. M. T. (1993). P-GaN/N-InGaN/N-GaN Double-Heterostructure Blue-Light-Emitting Diodes. *Japanese Journal of Applied Physics*, 32(1A):L8.

Neumann, M. D., Esser, N., Chauveau, J.-M., Goldhahn, R., and Feneberg, M. (2016). Inversion of absorption anisotropy and bowing of crystal field splitting in wurtzite MgZnO. *Applied Physics Letters*, 108(22):221105.

Nishigaki, S., Drachsel, W., and Block, J. (1979). Photon-induced field ionization mass spectrometry of ethylene on silver. *Surface Science*, 87(2):389–409.

NIST (2023). Atomic Weights and Isotopic Compositions for All Elements. `https://physics.nist.gov/cgi-bin/Compositions/stand_alone.pl`. [Online; accessed 10-Sept-2023].

Niu, B. H. C., Beacham, J. R., and Bryant, P. J. (1977). Photon assisted field ionization. *The Journal of Chemical Physics*, 67(5):2039–2042.

Nozik, A. (2002). Quantum dot solar cells. *Physica E*, 14(1):115–120.

Ohm, G. S. (1828). Die galvanische Kette, mathematisch bearbeitet. *Allgemeine Literatur-Zeitung*, 14:105.

Ozden, I., Makarona, E., Nurmikko, A. V., Takeuchi, T., and Krames, M. (2001). A dual-wavelength indium gallium nitride quantum well light emitting diode. *Applied Physics Letters*, 79(16):2532–2534.

Ozgur, U., Alivov, Y. I., Liu, C., Teke, A., Reshchikov, M. A., Dogan, S., Avrutin, V., Cho, S.-J., and Morkoc, H. (2005). A comprehensive review of ZnO materials and devices. *Journal of Applied Physics*, 98(4):041301.

Panitz, J. A. (1973). The 10 cm Atom Probe. *Review of Scientific Instruments*, 44(8):1034–1038.

Park, Y. S. and Schneider, J. R. (1968). Index of Refraction of ZnO. *Journal of Applied Physics*, 39(7):3049–3052.

Qiao, Y., Zhao, Y., Zhang, Z., Liu, B., Li, F., Tong, H., Wu, J., Zhou, Z., Xu, Z., and Zhang, Y. (2022). Single-Wedge Lift-Out for Atom Probe Tomography Al/Ni Multilayers Specimen Preparation Based on Dual-Beam-FIB. *Micromachines*, 13(1).

Reynolds, D., Look, D., and Jogai, B. (1996). Optically pumped ultraviolet lasing from ZnO. *Solid State Communications*, 99(12):873–875.

Rigutti, L. (2020). Chapter Two - Laser-assisted atom probe tomography. In Hÿtch, M. and Hawkes, P. W., editors, *Advances in Imaging and Electron Physics*, volume 213 of *Advances in Imaging and Electron Physics*, pages 29–53. Elsevier.

Rigutti, L., Blum, I., Shinde, D., Hernandez-Maldonado, D., Lefebvre, W., Houard, J., Vurpillot, F., Vella, A., Tchernycheva, M., Durand, C., et al. (2014). Correlation of microphotoluminescence spectroscopy, scanning transmission electron microscopy, and atom probe tomography on a single nano-object containing an InGaN/GaN multiquantum well system. *Nano letters*, 14(1):107–114.

Rigutti, L., Enrico, D. R., Chabanais, F., Blum, I., Houard, J., Gogneau, N., Largeau, L., Karg, A., Eickhoff, M., Lefebvre, W., and Vurpillot, F. (2021). Surface Microscopy of Atomic and Molecular Hydrogen from Field-Evaporating Semiconductors. *The Journal of Physical Chemistry C*, 125.

Rigutti, L., Tchernycheva, M., De Luna Bugallo, A., Jacopin, G., Julien, F. H., Furtmayr, F., Stutzmann, M., Eickhoff, M., Songmuang, R., and Fortuna, F. (2010). Photoluminescence polarization properties of single GaN nanowires containing $Al_xGa_{1-x}N$/GaN quantum discs. *Phys. Rev. B*, 81:045411.

Rigutti, L., Vella, A., Vurpillot, F., Gaillard, A., Sevelin-Radiguet, N., Houard, J., Hideur, A., Martel, G., Jacopin, G., Luna Bugallo, A. D., and Deconihout, B. (2013). Coupling atom probe tomography and photoluminescence spectroscopy: Exploratory results and perspectives. *Ultramicroscopy*, 132:75–80. IFES 2012.

Rigutti, L., Venturi, L., Houard, J., Normand, A., Silaeva, E. P., Borz, M., Malykhin, S. A., Obraztsov, A. N., and Vella, A. (2017). Optical Contactless Measurement of Electric Field-Induced Tensile Stress in Diamond Nanoscale Needles. *Nano Letters*, 17(12):7401–7409. PMID: 29095635.

Roessler, D. M. and Walker, W. C. (1967). Electronic Spectrum and Ultraviolet Optical Properties of Crystalline MgO. *Phys. Rev.*, 159:733–738.

Ruda, H. E. and Shik, A. (2005). Polarization-sensitive optical phenomena in semiconducting and metallic nanowires. *Phys. Rev. B*, 72:115308.

Russo, E. D., Blum, I., Houard, J., Gilbert, M., Da Costa, G., Blavette, D., and Rigutti, L. (2018). Compositional accuracy of atom probe tomography measurements in GaN: Impact of experimental parameters and multiple evaporation events. *Ultramicroscopy*, 187:126–134.

Russo, E. D., Mavel, A., Arcara, V. F., Damilano, B., Dimkou, I., Vézian, S., Grenier, A., Veillerot, M., Rochat, N., Feuillet, G., Bonef, B., Rigutti, L., Duboz, J.-Y., Monroy, E., and Cooper, D. (2020). Multi-microscopy nanoscale characterization of the doping profile in a hybrid Mg/Ge-doped tunnel junction. *Nanotechnology*, 31(46):465706.

Sakurai, T. and Müller, E. W. (1973). Field calibration using the energy distribution of a free-space field ionization. *Journal of Applied Physics*, 48(6):2618–2625.

Schmidt, G., Berger, C., Veit, P., Metzner, S., Bertram, F., Bläsing, J., Dadgar, A., Strittmatter, A., Christen, J., Callsen, G., Kalinowski, S., and Hoffmann, A. (2015). Direct evidence of single quantum dot emission from GaN islands formed at threading dislocations using nanoscale cathodoluminescence: A source of single photons in the ultraviolet. *Applied Physics Letters*, 106(25):252101.

Schmitt, S. W., Sarau, G., and Christiansen, S. (2015). Observation of strongly enhanced photoluminescence from inverted cone-shaped silicon nanostructures. *Sci. Rep.*, 5(1):17089.

Silaeva, E. P., Arnoldi, L., Karahka, M. L., Deconihout, B., Menand, A., Kreuzer, H. J., and Vella, A. (2014). Do dielectric nanostructures turn metallic in high-electric dc fields? . *Nano Lett.*, 14(11):6066–6072.

Skierbiszewski, C., Turski, H., Muziol, G., Siekacz, M., Sawicka, M., Cywiński, G., Wasilewski, Z. R., and Porowski, S. (2014). Nitride-based laser diodes grown by plasma-assisted molecular beam epitaxy. *Journal of Physics D: Applied Physics*, 47(7):073001.

Smeeton, T. M., Kappers, M. J., Barnard, J. S., Vickers, M. E., and Humphreys, C. J. (2003). Electron-beam-induced strain within InGaN quantum wells: False indium "cluster" detection in the transmission electron microscope. *Applied Physics Letters*, 83(26):5419–5421.

Sullivan, D. (2000). *One-Dimensional Simulation with the FDTD Method*. John Wiley & Sons, Ltd.

Sun, C. J., Kung, P., Saxler, A., Ohsato, H., Haritos, K., and Razeghi, M. (1994). A crystallographic model of (00·1) aluminum nitride epitaxial thin film growth on (00·1) sapphire substrate. *Journal of Applied Physics*, 75(8):3964–3967.

Sundaram, K. and Khan, A. (1997). Characterization and optimization of zinc oxide films by r.f. magnetron sputtering. *Thin Solid Films*, 295(1):87–91.

Takeuchi, T., Hasnain, G., Corzine, S., Hueschen, M., Richard P. Schneider, J., Kocot, C., Blomqvist, M., lan Chang, Y., Lefforge, D., Krames, M. R., Cook, L. W., and Stockman, S. A. (2001). GaN-Based Light Emitting Diodes with Tunnel Junctions. *Japanese Journal of Applied Physics*, 40(8B):L861.

Thomson, J. J. (1897). Cathode Rays. *The London, Edinburgh, and Dublin Philosophical Magazine and Journal of Science*, 44(269):293–316.

Tizei, L. H. G. and Kociak, M. (2012). Spectrally and spatially resolved cathodoluminescence of nanodiamonds: local variations of the NV0 emission properties. *Nanotechnology*, 23(17):175702.

Trampert, A., Brandt, O., and Ploog, K. (1997). Chapter 7 Crystal Structure of Group III Nitrides. In Pankove, J. I. and Moustakas, T. D., editors, *Gallium Nitride (GaN) I*, volume 50 of *Semiconductors and Semimetals*, pages 167–192. Elsevier.

Tsong, T. T. (1978). Measurement of the field evaporation rate of several transition metals. *Journal of Physics F: Metal Physics*, 8(7):1349.

Tsong, T. T., Block, J. H., Nagasaka, M., and Viswanathan, B. (1976). Photon stimulated field ionization. *The Journal of Chemical Physics*, 65(6):2469–2470.

Tumanov, D., Vaish, N., Nguyen, H. A., Curé, Y., Gérard, J.-M., Claudon, J., Donatini, F., and Poizat, J.-P. (2018). Static strain tuning of quantum dots embedded in a photonic wire. *Appl. Phys. Lett.*, 112(12):123102.

Turski, H., Siekacz, M., Muzioł, G., Hajdel, M., Stańczyk, S., Żak, M., Chlipała, M., Skierbiszewski, C., Bharadwaj, S., Xing, H. G., and Jena, D. (2019). Nitride LEDs and Lasers with Buried Tunnel Junctions. *ECS Journal of Solid State Science and Technology*, 9(1):015018.

Vella, A. (2013). On the interaction of an ultra-fast laser with a nanometric tip by laser assisted atom probe tomography: A review. *Ultramicroscopy*, 132:5–18. IFES 2012.

Vella, A., Shinde, D., Houard, J., Silaeva, E., Arnoldi, L., Blum, I., Rigutti, L., Pertreux, E., Maioli, P., Crut, A., and Del Fatti, N. (2018). Optothermal response of a single silicon nanotip. *Phys. Rev. B*, 97:075409.

Vella, A., Vurpillot, F., Gault, B., Menand, A., and Deconihout, B. (2006). Evidence of field evaporation assisted by nonlinear optical rectification induced by ultrafast laser. *Phys. Rev. B*, 73:165416.

Vurpillot, F. (2016). Chapter Seven - Three-Dimensional Reconstruction in Atom Probe Tomography: Basics and Advanced Approaches. In Lefebvre-Ulrikson, W., Vurpillot, F., and Sauvage, X., editors, *Atom Probe Tomography*, pages 183–249. Academic Press.

Vurpillot, F., Gault, B., Vella, A., Bouet, M., and Deconihout, B. (2006). Estimation of the cooling times for a metallic tip under laser illumination. *Applied Physics Letters*, 88(9). 094105.

Wang, X., Saito, K., Tanaka, T., Nishio, M., Nagaoka, T., Arita, M., and Guo, Q. (2015). Energy band bowing parameter in MgZnO alloys. *Applied Physics Letters*, 107(2):022111.

Wang, X. and Yoshikawa, A. (2004). Molecular beam epitaxy growth of GaN, AlN and InN. *Progress in Crystal Growth and Characterization of Materials*, 48-49:42–103. Vapour Growth of Bulk Crystals and Epitaxy: Part II.

Watson, I. M. (2013). Metal organic vapour phase epitaxy of AlN, GaN, InN and their alloys: A key chemical technology for advanced device applications. *Coordination Chemistry Reviews*, 257(13):2120–2141. Chemistry and Applications of Metal Nitrides.

Weikum, E. M., Dalapati, P., Beainy, G., Chauveau, J. M., Hugues, M., Lefebvre, D., Houard, J., Vella, A., and Rigutti, L. (2023). Influence of dynamic morphological modifications of atom probe specimens on the intensity of their photoluminescence spectra. *J. Opt. Soc. Am. B*, 40(6):1633–1643.

Wiechert, E. (1897). Ueber das Wesen der Elektricität. *Naturwissenschaftliche Rundschau*, 12:9496–9505.

Wikimedia (2008). Commons. `https://commons.wikimedia.org/wiki/File:Wurtzite_polyhedra.png`. [Online; accessed 12-July-2023].

Wu, J. and Walukiewicz, W. (2003). Band gaps of InN and group III nitride alloys. *Superlattices and Microstructures*, 34(1):63–75.

Wu, J., Walukiewicz, W., Yu, K. M., Ager, J. W., I., Haller, E. E., Lu, H., Schaff, W. J., Saito, Y., and Nanishi, Y. (2002). Unusual properties of the fundamental band gap of InN. *Applied Physics Letters*, 80(21):3967–3969.

Yan-Ping, S. and Guang-Hui, Y. (2011). Effect of Mg Doping on the Photoluminescence of GaN:Mg Films by Radio-Frequency Plasma-Assisted Molecular Beam Epitaxy. *Chinese Physics Letters*, 28(6):067807.

Yee, K. (1966). Numerical solution of initial boundary value problems involving maxwell's equations in isotropic media. *IEEE Transactions on Antennas and Propagation*, 14(3):302–307.

Yeo, I., de Assis, P.-L., Gloppe, A., Dupont-Ferrier, E., Verlot, P., Malik, N. S., Dupuy, E., Claudon, J., Gérard, J.-M., Auffèves, A., Nogues, G., Seidelin, S., Poizat, J.-P., Arcizet, O., and Richard, M. (2014). Strain-mediated coupling in a quantum dot–mechanical oscillator hybrid system. *Nat. Nanotechnol.*, 9(2):106–110.

Yoo, S.-H., Kim, S.-H., Woods, E., Gault, B., Todorova, M., and Neugebauer, J. (2022). Origins of the hydrogen signal in atom probe tomography: case studies of alkali and noble metals. *New Journal of Physics*, 24(1):013008.

Yoshida, S., Misawa, S., and Gonda, S. (1983). Improvements on the electrical and luminescent properties of reactive molecular beam epitaxially grown GaN films by using AlN-coated sapphire substrates. *Applied Physics Letters*, 42(5):427–429.

Yoshikawa, H. Y. H. and Adachi, S. A. S. (1997). Optical Constants of ZnO. *Japanese Journal of Applied Physics*, 36(10R):6237.

Zagonel, L. F., Mazzucco, S., Tencé, M., March, K., Bernard, R., Laslier, B., Jacopin, G., Tchernycheva, M., Rigutti, L., Julien, F. H., Songmuang, R., and Kociak, M. (2011). Nanometer Scale Spectral Imaging of Quantum Emitters in Nanowires and Its Correlation to Their Atomically Resolved Structure. *Nano Letters*, 11(2):568–573.

Zawadzka, A., Płóciennik, P., Strzelecki, J., and Sahraoui, B. (2014). Transparent amorphous zinc oxide thin films for NLO applications. *Optical Materials*, 37:327–337.